SCIENCE CHINA
Physics, Mechanics & Astronomy

• Invited Review •

May 2016 Vol. 59 No. 5: 650501
doi: 10.1007/s11433-016-5801-0

Complex fields in heterogeneous materials under shock: modeling, simulation and analysis

AiGuo Xu[1,2,3*], GuangCai Zhang[1,3,4], YangJun Ying[1], and Cheng Wang[4]

[1]*Laboratory of Computational Physics, Institute of Applied Physics and Computational Mathematics, P. O. Box 8009-26, Beijing 100088, China;*
[2]*Center for Applied Physics and Technology, MOE Key Center for High Energy Density Physics Simulations, College of Engineering, Peking University, Beijing 100871, China;*
[3]*State Key Laboratory of Theoretical Physics, Institute of Theoretical Physics, Chinese Academy of Sciences, Beijing 100190, China;*
[4]*State Key Laboratory of Explosion Science and Technology, Beijing Institute of Technology, Beijing 100081, China*

Received November 2, 2015; accepted December 21, 2015; published online March 24, 2016

In this mini-review we summarize the progress of modeling, simulation and analysis of shock responses of heterogeneous materials in our group in recent years. The basic methodology is as below. We first decompose the problem into different scales. Construct/Choose a model according to the scale and main mechanisms working at that scale. Perform numerical simulations using the relatively mature schemes. The physical information is transferred between neighboring scales in such a way: The statistical information of results in smaller scale contributes to establishing the constitutive equation in larger one. Except for the microscopic Molecular Dynamics (MD) model, both the mesoscopic and macroscopic models can be further classified into two categories, solidic and fluidic models, respectively. The basic ideas and key techniques of the MD, material point method and discrete Boltzmann method are briefly reviewed. Among various schemes used in analyzing the complex fields and structures, the morphological analysis and the home-built software, GISO, are briefly introduced. New observations are summarized for scales from the larger to the smaller.

complex fields, heterogeneous material, molecular dynamics, material point method, discrete Boltzmann model

PACS number(s): 05.40.-a, 62.50.Ef, 81.05.Rm, 81.05.Zx, 62.20.mm

Citation: A. G. Xu, G. C. Zhang, Y. J. Ying, and C. Wang, Complex fields in heterogeneous materials under shock: modeling, simulation and analysis, Sci. China-Phys. Mech. Astron. **59**, 650501 (2016), doi: 10.1007/s11433-016-5801-0

Contents

*Corresponding author (email: Xu_Aiguo@iapcm.ac.cn)

1 Introduction

It has long been recognized that the properties of materials are not uniquely determined by their average chemical composition but also, to a large extent, influenced by their structures. A heterogeneous material is a substance which is non-uniform in composition or character. The heterogeneous materials are ubiquitous in natural and industrial fields. In fact, nearly all the materials in macroscopic scales used in our daily life are heterogeneous. When a heterogeneous material is shocked, the morphology and distribution of the mesoscopic structures will largely influence the fields of stress and temperature inside the material, and consequently influence the mechanical properties of the material, influence the processes of failure nucleation and phase transition, etc. The behaviors of mesoscopic structures and the resulted non-equilibrium effects have been attracting more attention with time [1, 2]. Such problems have been becoming an essential inter-discipline subject in the fields of modern mechanics, physics and material science, etc. [3].

From the experimental side, since the shocking process is very quick, it is generally difficult to measure the details of the series actions occurred in the materials. From the theoretical side, since related to strong nonlinearity and complex fields, a pure theoretical investigation on such a system is nearly impossible. Therefore, numerical simulation plays a non-sustitutable role in better understanding shocked heterogeneous materials.

Such problems generally show effects or influence on our life in macroscopic scale, but are originated from the microscopic scale. The scale for the series of actions spans from 10^{-10} m to 1 m, i.e., about 10 orders in magnitude. How to model and simulate behaviors in such a wide scale has plagued the scientific community for a long time. Currently, the studies under the terminology, multi-scale modeling and simulation, can be roughly classified into two categories. In the first category, the complex problem is decomposed into various scales. One chooses the theory and method according to the specific scale and the dominant mechanism working in that scale. The statistical results of simulations in the smaller scale contribute to formulate the constitutive equation used in the larger scale. In the second category, the mainly concerned problems are around how to bridge the neighboring scales in simulations. In this mini-review we focus mainly on studies in the first category. Even in the first category there are too many problems to be studied in one decade. Therefore, under the topic of multi-scale modeling and simulations of heterogeneous materials, what we did in the past years are scattered and can only show a few aspects of the field.

According to the shear behavior heterogeneous materials can be classified into two kinds. The first kind is referred to as solid, and the second is referred to as fluid. A typical differences between solid and fluid is that the solid show anisotropic behaviors in both the microscopic and

macroscopic scales, while the fluid shows isotropic behavior in microscopic scale but anisotropic behavior in macroscopic scale. For solid heterogenous materials, what we concerned in the past years are mainly focused on the shocking responses of porous materials and microscopic mechanical behaviors of metal under various loadings. These studies present preliminary and fundamental references for modeling the elasto-plasticity, damage and fracture of solid materials under shock loading and unloading conditions. For fluid heterogeneous materials, we mainly studied the mechanical behavior and non-equilibrium phenomena in the kinetic transportation, phase transition, chemical coupling, etc. These observations present fundamental insights for modeling and simulation of complex fluids.

A porous material is a material containing voids or tunnels of different shapes and sizes. Such materials are commonly found in natural and industrial materials. Examples are referred to brick, wood, carbon, ceramic, foam, explosive and metal, etc. To have an effective application, their mechanical and thermodynamical behaviors must be understood in relating to their mesoscopic structures.

There contain a large quantity of micro-structures like dislocations, grain boundaries, voids, cavities, second phase grains in macroscopic metal materials. These structures influence the strength of the materials. When model these materials, the morphology and evolution process of these microstructures should be taken into account. In the past years, we investigated such systems via the MD simulation.

In fluid heterogeneous materials, around the shock-induced structures, material interfaces and structures induced by their stabilities, the thermodynamic non-equilibrium effects are pronounced. The traditional models based on Navier-Stokes equations are critical in treating with such problems. Under such cases, a kinetic model based on the Boltzmann equation, the Discrete Boltzmann Model (DBM) [4-8], can be used to adaptively capture the various non-equilibrium behaviors.

When phase transition and/or chemical reaction exist, the creation of new phase or matter and their evolution result in heat creation/absorption and more complicated kinetic transportation processes. The DBM is an effective mesoscopic approach to access such a system.

The rest of the paper is organized as below. In sect. 2 various models and simulation tools are introduced. Sect. 3 is for the analysis schemes for the complex fields and structures. The numerical experiments and observations are presented in sect. 4. Sect. 5 summarizes the paper and gives perspectives.

2 Models and simulation tools

Generally speaking, we can model the system in microscopic, mesoscopic and macroscopic scales. Since the matter can be divided infinitely, the delimitation of the scales is relative. In this review, the microscopic description is referred to as that based on Molecular Dynamics (MD). The macroscopic scale is referred to the scale of the whole system or a scale which is comparable with the system dimension. Thus, the wide range of scales in between the microscopic and macroscopic are referred to as mesoscopic. It is clear that the so-called mesoscopic scale is generally not referred to a specific scale, but a scale series.

The macroscopic model is generally described by a set of partial differential equations corresponding to the fundamental conservation laws. Because it uses the smallest number of the mechanical quantities, the macroscopic model is the simplest and frequently used in many engineering applications. It has been well-known that the macroscopic model is not sufficient to describe the complex behaviors occurring in heterogeneous materials under shock. Such behaviors are generally originated from the molecular scale and make effects in macroscopic via a series of complex interactions between various structures. Intuitively, the complete understanding of the whole story resorts to the MD simulation. But, practically, it is far from possible to use MD to simulate behaviors in macroscopic scale. Under such cases, the mesoscopic modeling technology which connecting the macroscopic and the most necessary microscopic behaviors is needed. Compared with the MD results, the mesoscopic modeling is some kind of coarse-grained description of the microscopic details via some slow or conservative variables.

2.1 Microscopic MD model

Molecular dynamics model describes physical movements of particles (molecules or atoms) in the context of N-body interaction, where N is the particle number in the system. In the most common MD simulations, the trajectories of particles are tracked via numerically solving the Newton's equations of motion for a system of interacting particles, where forces between the particles are determined from the molecular mechanics force fields (or interatomic potentials). The MD method was originally proposed by theoretical physicists in the late 1950s [9, 10], but now is extensively used in chemical physics, materials science and the modeling of bio-molecules, etc. Due to the vast number of particles in the systems, the MD method resorts to numerical simulations.

The first important step in the MD simulation is to establish the inter-particle potential. In principle, a molecule is influenced by all other surrounding molecules. Fortunately, the strength of the interaction decreases quickly with the distance. Therefore, the second important step in the MD simulation is to truncate the inter-particle potential. The smaller the truncation radius, the less the computational cost. The validity of truncation position is determined by that the simulation results of known material parameters are correct. To compute the force acting on a molecule, one has to search all the surrounding molecules located within the truncation radius. Because the one-by-one searching is not affordable for a system with more than 1 million atoms, the third important step is to index the molecules in terms of a link-list

corresponding to background grid mesh.

Based on the inter-particle potential we can obtain the summation of the external forces acting on any molecule and consequently the acceleration of it. Thus, from the current position and velocity, we can obtain its position and velocity at the next time step. The positions and velocities of all the molecules can be updated in the same way. Then the summation of external forces acting on any molecule is updated. via such iteration steps, we can track all the molecules in the system. The physical variables like the energy, temperature, pressure, density, flow velocity, etc, can be obtained from the MD data via appropriate statistical calculations. The micro-structures can be identified, described and tracked via some data post-treatment algorithms. In our studies, the numerical MD simulations are performed using the well-known LAMMPS software package. The interatomic interaction in each material is described by an embedded atom method (EAM) potential [11, 12]. The dilative strain is applied uniformly through re-scaling the coordinates as in the Parrinello-Rahman approach. The data are analyzed by using our home-built softwares.

Now, we can obtain a preliminary estimation on the scale of the material that the MD can be used to simulate. The molecule numbers used in current MD simulations are generally less than 10^7. That is to say, molecule number in one dimension is only in the order 10^2. For a general solid material, the distance in between two neighboring particles is about 10^{-10} m. It is clear that, for a practical MD simulation in nowadays, the largest scale in one dimensional is smaller that 0.1 μm. Since the time step is generally in the order of femto-second, i.e. 10^{-15} s, the whole duration being simulated is generally in the order of pico-second, i.e., 10^{-12} s. At the same time, from the theoretical point of view, a long MD simulation is mathematically ill-conditioned. It generates cumulative errors in numerical integration which can be minimized via selecting proper algorithms and parameters, but can not be eliminated entirely.

There are many phenomenological physical models for a heterogeneous solid materials. In this review the material is assumed to follow an associative von Mises plasticity model with linear kinematic and isotropic hardening [13]. The Material Point Method (MPM) [14-26] is used to simulate the mesocopic and macroscopic behaviors in the shocked porous materials.

2.2 Solid model and MPM

2.2.1 Physical model

If we introduce a linear isotropic elastic relation and assume that the volumetric plastic strain is zero, the deviatoric stress $\boldsymbol{s}$ or strain $\boldsymbol{e}$ can be decoupled from volumetric one, $-P\boldsymbol{I}$ or $\theta\boldsymbol{I}/3$, where P and θ are scalars, $\boldsymbol{s}$ and $\boldsymbol{e}$ are tensors. The stress and strain tensors, $\boldsymbol{\sigma}$ and $\boldsymbol{\varepsilon}$, can be written as:

$$\boldsymbol{\sigma} = \boldsymbol{s} - P\boldsymbol{I}, \quad P = -\frac{1}{3}\mathrm{Tr}(\boldsymbol{\sigma}), \tag{1}$$

$$\boldsymbol{\varepsilon} = \boldsymbol{e} + \frac{1}{3}\theta\boldsymbol{I}, \quad \theta = \frac{1}{3}\mathrm{Tr}(\boldsymbol{\varepsilon}). \tag{2}$$

Generally, the strain $\boldsymbol{e}$ can be decomposed as $\boldsymbol{e} = \boldsymbol{e}^e + \boldsymbol{e}^p$, where $\boldsymbol{e}^e$ and $\boldsymbol{e}^p$ are the traceless elastic and plastic components, respectively. Until the von Mises yield criterion,

$$\sqrt{\frac{3}{2}}\,\|\boldsymbol{s}\| = \sigma_Y, \tag{3}$$

is reached, the material shows a linear elastic response, where σ_Y is the plastic yield stress increasing linearly with the second invariant of the plastic strain tensor $\boldsymbol{e}^p$, i.e.,

$$\sigma_Y = \sigma_{Y0} + E_{\tan}\,\|\boldsymbol{e}^p\|\,, \tag{4}$$

where σ_{Y0} is the initial yield stress and $E_{\tan}$ is the tangential module. The deviatoric stress $\boldsymbol{s}$ is calculated by $\boldsymbol{s} = [E/(1+\nu)]\boldsymbol{e}^e$, where E is the Yang's module and ν the Poisson's ratio. The pressure P is calculated by using the following Mie-Grüneissen state of equation:

$$P - P_{\mathrm{H}} = \frac{\gamma(V)}{V}[E - E_{\mathrm{H}}(V_{\mathrm{H}})], \tag{5}$$

where P_{H}, V_{H} and E_{H} are pressure, specific volume and energy on the Rankine-Hugoniot curve, respectively. The relation between P_{H} and V_{H} can be estimated by experiment. It can be written as:

$$P_{\mathrm{H}} = \begin{cases} \dfrac{\rho_0 c_0^2\left(1-\frac{V_{\mathrm{H}}}{V_0}\right)}{(\lambda-1)^2\left(\frac{\lambda}{\lambda-1}\times\frac{V_{\mathrm{H}}}{V_0}-1\right)^2}, & V_{\mathrm{H}} \leqslant V_0, \\ \rho_0 c_0^2\left(\dfrac{V_{\mathrm{H}}}{V_0}-1\right), & V_{\mathrm{H}} > V_0. \end{cases} \tag{6}$$

We assume that the initial material density and sound speed are ρ_0 and c_0, respectively. The shock speed U_{s} and the particle speed U_{p} after the shock front follows a linear relation,

$$U_{\mathrm{s}} = c_0 + \lambda U_{\mathrm{p}},$$

where λ is a characteristic coefficient of material. Both the shock compression and the plastic work W_{p} result in increasing of temperature. The temperature increase from shock compression is calculated by

$$\frac{\mathrm{d}T_{\mathrm{H}}}{\mathrm{d}V_{\mathrm{H}}} = \frac{c_0^2\cdot\lambda(V_0-V_{\mathrm{H}})^2}{c_v[(\lambda-1)V_0-\lambda V_{\mathrm{H}}]^3} - \frac{\gamma(V)}{V_H}T_{\mathrm{H}}, \tag{7}$$

where c_v is the specific heat. Eq. (7) can be obtained from the thermal equation and the Mie-Grüneissen equation of state [27]. The temperature increase due to plastic work is calculated by

$$\mathrm{d}T_{\mathrm{p}} = \frac{\mathrm{d}W_{\mathrm{p}}}{c_v}. \tag{8}$$

Eqs. (7) and (8) can be written in the form of increment.

2.2.2 *Material-Point Method*

The MPM is a particle method. It was originally introduced in fluid dynamics by Harlow et al. [18] and extended to solid mechanics by Burgess et al. [19], then developed by various groups, including ours [20-26].

The MPM discretizes the continuum bodies with N_p material particles, where p is the index of particle. Each material particle carries the information of mass m_p, density ρ_p, position $\boldsymbol{x}_p$, velocity $\boldsymbol{v}_p$, strain tensor $\boldsymbol{\varepsilon}_p$, stress tensor $\boldsymbol{\sigma}_p$ and all other internal state variables necessary for the constitutive model. At each time step, the calculations can be classified into two parts: a Lagrangian part and a convective one. At first, the computational mesh deforms with the body. It is used to determine the strain increment, and the stresses in the sequel. Then, a new position of the computational mesh is chosen. Particularly, it may be the previous one. The velocity field is mapped from the particles to the mesh nodes. Nodal velocities are determined by using the equivalence of momentum calculated for the particles and for the computational grid. The MPM not only takes advantages of both the Lagrangian and Eulerian algorithms but also avoid their drawbacks as well.

At each time step, the mass and velocities of the material particles are mapped onto the background computational mesh. The mapped momentum at node i is obtained by

$$m_i\boldsymbol{v}_i = \sum_p m_p\boldsymbol{v}_p N_i(\boldsymbol{x}_p),$$

where N_i is the element shape function and the nodal mass m_i reads

$$m_i = \sum_p m_p N_i(\boldsymbol{x}_p).$$

Suppose that a computational mesh is constructed of eight-node cells for three-dimensional problems, then the shape function reads

$$N_i = \frac{1}{8}(1+\xi\xi_i)(1+\eta\eta_i)(1+\varsigma\varsigma_i), \tag{9}$$

where ξ, η, ς are the natural coordinates of the material particle in the cell along the x-, y-, and z-directions, respectively, ξ_i, η_i, ς_i take corresponding nodal values ±1. The mass of each particle is equal and fixed, so the mass conservation equation,

$$\mathrm{d}\rho/\mathrm{d}t + \rho\nabla\cdot\boldsymbol{v} = 0,$$

is automatically satisfied. The momentum equation reads,

$$\rho\mathrm{d}\boldsymbol{v}/\mathrm{d}t = \nabla\cdot\boldsymbol{\sigma} + \rho\boldsymbol{b}, \tag{10}$$

where ρ is the mass density, $\boldsymbol{v}$ the velocity, $\boldsymbol{\sigma}$ the stress tensor and $\boldsymbol{b}$ the body force. Eq. (10) is solved on a finite element mesh in a lagrangian frame. Its weak form reads

$$\int_\Omega \rho\delta\boldsymbol{v}\cdot\mathrm{d}\boldsymbol{v}/\mathrm{d}t\mathrm{d}\Omega + \int_\Omega \delta(\boldsymbol{v}\nabla)\cdot\boldsymbol{\sigma}\mathrm{d}\Omega - \int_{\Gamma_t}\delta\boldsymbol{v}\cdot\boldsymbol{t}\mathrm{d}\Gamma - \int_\Omega \rho\delta\boldsymbol{v}\cdot\boldsymbol{b}\mathrm{d}\Omega = 0. \tag{11}$$

Since the continuum bodies is described by a finite set of material particles, the mass density can be written as:

$$\rho(\boldsymbol{x}) = \sum_{p=1}^{N_p} m_p\delta(\boldsymbol{x}-\boldsymbol{x}_p),$$

where δ is the Dirac delta function with dimension of the inverse of volume. Substituting $\rho(\boldsymbol{x})$ into the weak form of the momentum equation converts the integral to the sums of quantities evaluated at the material particles. So,

$$m_i\mathrm{d}\boldsymbol{v}_i/\mathrm{d}t = (\boldsymbol{f}_i)^{\mathrm{int}} + (\boldsymbol{f}_i)^{\mathrm{ext}}, \tag{12}$$

where the internal force vector is given by

$$\boldsymbol{f}_i^{\mathrm{int}} = -\sum_p^{N_p} m_p\boldsymbol{\sigma}_p\cdot(\nabla N_i)/\rho_p,$$

and the external force vector is given by

$$\boldsymbol{f}_i^{\mathrm{ext}} = \sum_{p=1}^{N_p} N_i\boldsymbol{b}_p + \boldsymbol{f}_i^c,$$

where the vector $\boldsymbol{f}_i^c$ is the contacting force between two bodies. In the case where all colliding bodies are composed of the same material, $\boldsymbol{f}_i^c$ is treated in the same way as the internal force.

The nodal accelerations can be calculated by using eq. (12) with an explicit time integrator. To have a stable simulation, the time step Δt should be less than the critical value,

$$\Delta t_C = \frac{\Delta x_{\min}}{\max(c_p + |\boldsymbol{v}_p|)},$$

where $\Delta x_{\min}$ is the smallest cell size, c_p the sound speed at particle p. Once the motion equations have been solved on the cell nodes, the new nodal values of acceleration can be used to update the velocity of the material particles. The strain increment for each material particle is determined by using the gradient of nodal basis function evaluated at the position of the material particle. The corresponding stress increment can be obtained from the constitutive model. The internal state variables can also be completely updated. The computational mesh may be the original one or a newly defined one, choose for convenience, for the next time step. More details of the algorithm can be referred to refs. [25, 26].

In our studies the possible phase transitions are studied via MD and DBM, instead of MPM simulations.

2.3 Fluid model and DBM

Shock waves may occur in many different kinds of materials. However, in parts of this review the discussion is restricted to situations where the material may be described, to a good approximation, by the model of a compressible, heat-conducting fluid. The most frequently used hydrodynamic

models in engineering applications are the Euler and Navier-Stokes equations. The model described by Euler equations assumes that (i) the fluid is always at its local thermodynamic equilibrium, and consequently can be completely described by the thermodynamic quantities, (ii) the change or transition between various mechanical states is quasi-static and iso-entropic. According to this model, the shock wave has no thickness. The model by Navier-Stokes equations assumes that all the relevant non-equilibrium behaviors can be described by non-equilibrium linear responses of gradients of physical quantities. The linear response of momentum flux is described by the viscosity tensor which is proportional to the gradient of flow velocity. The linear response of energy flux is described by the heat conduction which is proportional to the gradient of local temperature. According to this model, the width of the shock wave depends on the viscosity and heat conductivity. Around the various interfaces, such as the material interfaces, shock fronts, new phase boundaries, and within the chemical reaction zone, the non-equilibrium effects may be so pronounced that the linear response theory does not work any more. At the same time, some specific non-equilibrium status are invisible in the Navier-Stokes model, although those information is helpful for us to physically understand the flow system. Under such conditions, the models by Euler and Navier-Stokes equations may lead to unreasonable results or missing valuable information. Consequently, the DBM is more preferable.

2.3.1 *Brief review of DBM*

Historically, the DBM was developed from the well-known Lattice Boltzmann Method (LBM) which was developed from the lattice gas cellular automaton model [28]. Mathematically, the DBM can be regarded as a special discretization of the Boltzmann equation.

Roughly speaking, the discrete Boltzmann models can be further classified into two categories. The first category is the one generally referred to as LBM in literature. In the first category the LBM is regarded as a kind of new scheme to numerically solve partial differential equations, such as the Navier-Stokes equaitons, etc. In the second category the DBM works as a kind of novel mesoscopic and coarse-grained kinetic model for complex fluids. The most important difference between the two kinds of DBMs are as below. In the first category the LBM must be faithful to the original physical model, while in the second category, the DBM must possess some points beyond the original physical model. The second kind of DBM aims to probe the trans- and supercritical fluid behaviors [7] or to study simultaneously the hydrodynamic non-equilibrium (HNE) and thermodynamic non-equilibrium (TNE) behaviors [4-6,8]. It has brought significant new physical insights into the systems and promoted the development of new methods in the fields. For example, new observations on fine structures of shock and detonation waves have been obtained [29, 30]; these new observations have been used to discriminate various interfaces [29, 30]; the intensity of TNE has been used as a physical criterion to discriminate the two stages, spinodal decomposition and domain growth, in phase separation [8]; based on the features of TNE, some new front-tracking schemes have been designed [31]. In a recent study, the relation between TNE quantities and entropy production rate has been established [32]. Since the goals are different, the criteria used to formulate the two kinds of models are significantly different, even though there may be considerable overlaps between them.

Physically, the DBM can be regarded as a model being coarser-grained than the Boltzmann equation. It can be obtained via two important steps of coarser-grained modelings. The first step is the linearization of the collision operator in the Boltzmann equation. In this step, we obtain the Boltzmann-BGK-like equations. The second step is the special discretization of the particle velocity space. The DBM obtained in this way is roughly equivalent to a hydrodynamic model supplemented by a coarse-grained model of the TNE behaviours.

From the side of physical modeling, the MD is a microscopic particle model which is independent of the continuum assumption. Consequently, it can be used to study the TNE behaviours, no matter the material is in solid or fluid state. The MPM is based on the solid mechanics which is based on the continuum assumption. The DBM is based on the Boltzmann equation. It includes and is beyond the hydrodynamic model, for example, the Navier-Stokes equations [4-8]. Here we briefly review the recently developed DBMs for multiphase flows and for detonation systems.

2.3.2 *DBM for multiphase flows*

In 2007, Gonnella, Lamura and Sofonea (GLS) [33] proposed a LBM for liquid-vapor two-phase flows, where the effects of interparticle force enter the force term of the lattice Boltzmann equation. In 2011, our group proposed to use the fast Fourier transform and its inverse to calculate the spatial derivatives in the GLS model [34, 35]. In this way, the total energy conservation can be better held and the spurious velocities can be refrained to a negligible scale in real simulations. Recently, our group further improved the model in two sides, inserted a more practical equation of state and supplemented a methodology to investigate the non-equilibrium features in the system [8, 36].

The GLS LBM can be described by the following evolution equation:

$$\frac{\partial f_{ki}}{\partial t} + \boldsymbol{v}_{ki} \cdot \frac{\partial f_{ki}}{\partial \boldsymbol{r}} = -\frac{1}{\tau}[f_{ki} - f_{ki}^{eq}] + I_{ki}, \tag{13}$$

where the subscript ki are the indexes of the discrete velocity and I_{ki} reads

$$I_{ki} = -[A + \boldsymbol{B} \cdot (\boldsymbol{v}_{ki} - \boldsymbol{u}) + (C + C_q)(\boldsymbol{v}_{ki} - \boldsymbol{u})^2] f_{ki}^{eq}, \tag{14}$$

with

$$A = -2(C + C_q)T, \tag{15}$$

$$\boldsymbol{B} = \frac{1}{\rho T}[\nabla(P^{\rm vdw} - \rho T) + \nabla\cdot\boldsymbol{\Lambda} - \nabla(\zeta\nabla\cdot\boldsymbol{u})], \tag{16}$$

$$\begin{aligned} C =& \frac{1}{2\rho T^2}\Big\{(P^{\rm vdw} - \rho T)\nabla\cdot\boldsymbol{u} + \boldsymbol{\Lambda}\colon\nabla\boldsymbol{u} - \zeta(\nabla\cdot\boldsymbol{u})^2 \\ &+ \frac{9}{8}\rho^2\nabla\cdot\boldsymbol{u} + K\Big[-\frac{1}{2}(\nabla\rho\cdot\nabla\rho)\nabla\cdot\boldsymbol{u} \\ &- \rho\nabla\rho\cdot\nabla(\nabla\cdot\boldsymbol{u}) - \nabla\rho\cdot\nabla\boldsymbol{u}\cdot\nabla\rho\Big]\Big\}, \end{aligned} \tag{17}$$

$$C_q = \frac{1}{2\rho T^2}\nabla\cdot[2q\rho T\nabla T]. \tag{18}$$

Here ρ, $\boldsymbol{u}$, T are the local density, velocity, temperature, respectively. The tensor $\boldsymbol{\Lambda}$ is contribution of density gradient to pressure tensor and read

$$\boldsymbol{\Lambda} = K\nabla\rho\nabla\rho - K(\rho\nabla^2\rho + |\nabla\rho|^2/2)\boldsymbol{I} - [\rho T\nabla\rho\cdot\nabla(K/T)]\boldsymbol{I},$$

where $\boldsymbol{I}$ is the unit tensor, K the surface tension coefficient and ζ the bulk viscosity. The model is consistent with the thermodynamic relations proposed by Onuki [37].

The original GLS model utilizes the van der Waals equation of state,

$$P^{\rm vdw} = \frac{3\rho T}{3-\rho} - \frac{9}{8}\rho^2$$

with fixed parameters. The density ratio R between the liquid and vapor phases which can be stably simulated is generally less than 10 due to the numerical instability problem. Since the Carnahan-Starling equation of state [38] modifies the repulsive term of van der Waals equation of state so that it presents a more accurate representation for hard sphere interactions. The Carnahan-Starling equation of state reads

$$p^{\rm cs} = \rho T\frac{1+\eta+\eta^2-\eta^3}{(1-\eta)^3} - a\rho^2, \tag{19}$$

with $\eta = b\rho/4$, where a and b are the attraction and repulsion parameters. Subsequently, the total energy density becomes

$$e_T = \rho T - a\rho^2 + K|\nabla\rho|^2/2 + \rho u^2/2.$$

2.3.3 DBM for system under detonation

As for the discrete Boltzmann modeling and simulation of combustion systems, the current studies can also be classified into two categories. Most of existing studies belong to the first category where the LBM is used as a kind of alternative numerical scheme and are focused on cases with low Mach number where the incompressible models work. The first DBM for detonation system [39] appeared in 2013. It is also the first study aiming to investigate both the HNE and TNE in the combustion system via the discrete kinetic modeling. To model and simulate the non-equilibrium behaviors in axial symmetric implosion and explosion processes, a DBM for detonation system in polar-coordinates [40] was proposed in 2014. A multiple-relaxation-time version of DBM for detonation system was developed and some fundamental issues in formulating discrete kinetic models were reviewed in a recent study [30]. A double-distribution-function DBM for detonation system is referred to ref. [41].

Up to now, from the view of mathematical modeling, the only difference of the DBM from the traditional hydrodynamic model is that the Navier-Stokes or Euler equations for flow are replaced by the discrete Boltzmann equation(s). The phenomenological equation describing the reaction process is the same. But from the view of physical application, the DBM is roughly equivalent to a hydrodynamic model supplemented by a coarse-grained model of the TNE behaviors. Being able to capture various non-equilibrium effects and being easy to parallelize are two features of the second kind of DBM. The two points are also the physical gain and computational gain of DBM replacing the traditional hydrodynamic model. Some more realistic DBMs for detonation systems are in progress.

The hydrodynamic modeling and microscopic molecular dynamics have seen great achievements in detonation simulations. But for problems relevant to the mesoscopic scales, where the hydrodynamic modeling is not enough to capture the non-equilibrium behaviors and the molecular dynamics simulation is not affordable, the modeling and simulation are still open and challenging. Roughly speaking, there are two research directions in accessing the mesoscopic behaviors. One direction is to start from the continuous description at macroscopic scale to kinetic descriptions at smaller scales, the other direction is to start from the particle description at microscopic scale to statistical descriptions at larger scales. The idea of second kind of DBM belongs to that of the first direction. It will contribute more to the studies on the non-equilibrium behaviors in various complex fluids.

2.3.4 Two kinds of non-equilibrium effects

If choose the Navier-Stokes model as the macroscopic counterpart, the DBM must be based on, at least, the following seven kinetic moments:

$$\boldsymbol{M}_0^{\rm eq} = \sum_{ki} f_{ki}^{eq} = \rho, \tag{20}$$

$$\boldsymbol{M}_1^{\rm eq} = \sum_{ki} f_{ki}^{eq}\boldsymbol{v}_{ki} = \rho\boldsymbol{u}, \tag{21}$$

$$\boldsymbol{M}_{2,0}^{\rm eq} = \sum_{ki}\frac{1}{2}f_{ki}^{eq}\boldsymbol{v}_{ki}\cdot\boldsymbol{v}_{ki} = \rho\left(T + \frac{u^2}{2}\right), \tag{22}$$

$$\boldsymbol{M}_2^{\rm eq} = \sum_{ki} f_{ki}^{eq}\boldsymbol{v}_{ki}\boldsymbol{v}_{ki} = \rho(T\boldsymbol{I} + \boldsymbol{uu}), \tag{23}$$

$$\begin{aligned} \boldsymbol{M}_3^{\rm eq} = \sum_{ki} f_{ki}^{eq}\boldsymbol{v}_{ki}\boldsymbol{v}_{ki}\boldsymbol{v}_{ki} = \rho[T(&\boldsymbol{u}_\alpha\boldsymbol{e}_\beta\boldsymbol{e}_\gamma\delta_{\beta\gamma} + \boldsymbol{e}_\alpha\boldsymbol{u}_\beta\boldsymbol{e}_\gamma\delta_{\alpha\gamma} \\ &+ \boldsymbol{e}_\alpha\boldsymbol{e}_\beta\boldsymbol{u}_\gamma\delta_{\alpha\beta}) + \boldsymbol{uuu}], \end{aligned} \tag{24}$$

$$\boldsymbol{M}_{3,1}^{\rm eq} = \sum_{ki}\frac{1}{2}f_{ki}^{eq}\boldsymbol{v}_{ki}\cdot\boldsymbol{v}_{ki}\boldsymbol{v}_{ki} = \rho\boldsymbol{u}\left(2T + \frac{1}{2}\boldsymbol{u}\cdot\boldsymbol{u}\right), \tag{25}$$

$$\boldsymbol{M}_{4,2}^{\mathrm{eq}} = \sum_{ki} \frac{1}{2} f_{ki}^{eq} \boldsymbol{v}_{ki} \cdot \boldsymbol{v}_{ki} \boldsymbol{v}_{ki} \boldsymbol{v}_{ki} = \rho \Big[\Big(2T + \frac{\boldsymbol{u} \cdot \boldsymbol{u}}{2} \Big) T \boldsymbol{I} + \boldsymbol{u}\boldsymbol{u} \Big(3T + \frac{\boldsymbol{u} \cdot \boldsymbol{u}}{2} \Big) \Big], \quad (26)$$

where $\boldsymbol{M}_{m,n}^{\mathrm{eq}}$ stands for that the m-th order tensor is contracted to a n-th order one. Among the seven kinetic moment relations, only for the first three, the local equilibrium distribution function f_{ki}^{eq} can be replaced by f_{ki}, which means that, when the system approaches or deviates from the thermodynamic equilibrium, the mass, momentum and energy are conserved. Replacing f_{ki}^{eq} by f_{ki} in eqs. (23)-(26) results in the imbalance and the deviation described by

$$\boldsymbol{\Delta}_n = \boldsymbol{M}_n(f_{ki}) - \boldsymbol{M}_n^{\mathrm{eq}}(f_{ki}^{eq}). \quad (27)$$

The quantity $\boldsymbol{\Delta}_n$ presents a simple, convenient and effective measure to the departure of the system from the local thermodynamic equilibrium.

If the shocking is so strong that the material can be regarded as ideal gas, we can consider that the HNE and TNE effects are only induced by gradients of macroscopic quantities, also referred to gradient force. When the inter-particle interaction potential can not be completely ignored and the system can be regarded as a multiphase flow system. The force term in the DBM equation works as the second driving force. Especially, the right-hand side of eq. (13) can be rewritten as:

$$\mathrm{RHS} = -\frac{1}{\tau} \left[f_{ki} - (1 + \tau\theta) f_{ki}^{eq} \right] = -\frac{1}{\tau} \left[f_{ki} - f_{ki}^{eq,\mathrm{NEW}} \right], \quad (28)$$

where

$$\theta = -[A + \boldsymbol{B} \cdot (\boldsymbol{v}_{ki} - \boldsymbol{u}) + (C + C_q)(\boldsymbol{v}_{ki} - \boldsymbol{u})^2]$$

and

$$f_{ki}^{eq,\mathrm{NEW}} = (1 + \tau\theta) f_{ki}^{eq}.$$

It can be considered as a new equilibrium state shifted by the interparticle force. Consequently,

$$\boldsymbol{\Delta}_n^F = \boldsymbol{M}_n(\tau\theta f_{ki}^{eq}) = \boldsymbol{M}_n(\tau I_{ki}) \quad (29)$$

describes the non-equilibrium effects induced by the interparticle force. What we measure from f_{ki} and f_{ki}^{eq},

$$\boldsymbol{\Delta}_n = \boldsymbol{M}_n(f_{ki}) - \boldsymbol{M}_n^{\mathrm{eq}}(f_{ki}^{eq}) = \boldsymbol{\Delta}_n^F + \boldsymbol{\Delta}_n^G \quad (30)$$

are the combined or the net non-equilibrium effects, where

$$\boldsymbol{\Delta}_n^G = \boldsymbol{M}_n(f_{ki}) - \boldsymbol{M}_n^{\mathrm{eq}}(f_{ki}^{eq,\mathrm{NEW}}) \quad (31)$$

are the non-equilibrium effects induced by the gradient force. It is clear that, when the interparticle force disappears, the net non-equilibrium effects are only from the gradient force, i.e., $\boldsymbol{\Delta}_n = \boldsymbol{\Delta}_n^G$, corresponding to an ideal gas system. Note that, the kinetic moment $\boldsymbol{M}_n$ contains the information of $\boldsymbol{u}$, so do the non-equilibrium quantity $\boldsymbol{\Delta}_n$. They describe both the HNE and TNE effects. If we use the central kinetic moment $\boldsymbol{M}_n^*(f_{ki}) = \sum f_{ki}(\boldsymbol{v}_{ki} - \boldsymbol{u})^n$, then $\boldsymbol{\Delta}_n^*$ does not contain the effects of $\boldsymbol{u}$, describes only the TNE effects. Because $\boldsymbol{M}_n^*(f_{ki})$ is only the representation of the thermo-fluctuations of molecules relative to $\boldsymbol{u}$.

Compromise The physically concerned hydrodynamic quantities are some kinetic moments of the distribution function, f. According to the Chapman-Enskog analysis, they can finally be roughly calculated from some kinetic moments of the local equilibrium distribution function, f^{eq}. The calculation of any non-conserved quantity triggers the requirement of higher-order kinetic moments of f^{eq}. When construct the discrete Boltzmann model, we must ensure the required kinetic moments of f^{eq}, originally in integral form, can be calculated in discrete summation form.

All descriptions on the TNE based on finite number of kinetic moments are coarse-grained. The more accurate the TNE is to be described, the more kinetic moments are required. The more the required kinetic moments, the higher the computational cost. In practical applications, we have to make compromise between what we want and what we can afford.

3 Analysis schemes for complex fields and structures

No matter which physical model and simulation tool are used, after the simulation, how to analyze the data and pick out reliable information is of key importance. In our MD simulation studies, two methods are used. (i) The atoms are distinguished by the Common Neighbor Analysis (CNA) method [42-44]. In this method the signature of the local crystal structure of an atom is identified by computing three characteristic numbers for each of the n neighbor bonds of the central atom; (ii) the Burgers vectors of the evolved dislocations in the MD simulations are calculated using our home-built code. In this code, dislocation lines and their directions are first identified. Then, surrounding the dislocation lines, appropriate Burgers circuits that cross stacking-fault planes or perfect crystal are selected, and the atom-to-atom sequences corresponding to the circuits are determined. Finally, after a summation over vectors of the Thompson's tetrahedron and its mirrors that are most closest to the atom-to-atom vectors, the Burgers vectors of the dislocations are obtained.

For complex system in the mesoscopic and macroscopic scales, nearly all the analysis methods are some sort of statistics. The most commonly used ones are the mean values of physical variables and their corresponding fluctuations. The rheological description provides helpful measurements like the spatial correlation, temporal correlation, spatial-temporal correlation, structure factor, characteristic length, etc [45-47]. In our studies the morphological description is introduced to describe the complex fields in heterogeneous materials under shock [48, 49]. Several new schemes, including the turbulence mixing, volume dissipation, entropy increment, cluster

identification, tracking of characteristic structures were designed [50-52].

3.1 For fields and structures based on ordered points

To analyze fields and structures based on ordered points, a variety of schemes can be used. For example, (i) common schemes of statistical physics, (ii) rheological descriptions, (iii) morphological characterization, etc. Scheme examples for (i) are referred to the mean value and fluctuations, turbulence dissipation, volume dissipation, entropy production. Scheme examples for (ii) are referred to spatial correlation, temporal correlation and spatial-temporal correlation, structure factor, characteristic length and time scales. Scheme examples for (iii) are referred to the Minkowskii functionals [53]. All of them are some kinds of statistics.

Here we concentrate only on the set of statistics known as Minkowski functionals [53]. A physical field can be described by $\Theta(\boldsymbol{x})$, where $\boldsymbol{x}$ is the position, Θ a physical variable. The physical variable Θ can be a scalar state variable like temperature T, density ρ and pressure P. It can also be the size of velocity $\boldsymbol{v}$, velocity component in one degree of freedom, as well as some specific stress component, etc.

According to a general theorem of integral geometry, all properties of a D-dimensional convex set (or more generally, a finite union of convex sets) satisfying the morphological properties (translational invariance and additivity), are contained in $D+1$ numerical values [48, 54]. The points with $\Theta(\boldsymbol{x}) \geqslant \Theta_{\rm th}$ compose the two- or three-dimensional convex set and its morphological properties can be completely described by three or four functionals, where $\Theta_{\rm th}$ is some threshold value. In the case of two or three dimensions, the Minkowski functionals have intuitive geometric interpretations. For the two-dimensional case, the three Minkowski functionals correspond geometrically to the total fractional area A, the total boundary length L, and the Euler characteristic χ which is equivalent to the topological genus. In practical application, the Minkowski functions can be made dimensionless. Such a morphological description has been successfully applied in describing patterns in reaction-diffusion system [54], phase separation [55-57] and complex fields in porous materials under shock [48], etc.

For the two-dimensional square lattice, a lattice node possesses four vertices. A region with connected lattice nodes with $\Theta(\boldsymbol{x}) \geqslant \Theta_{\rm th}$ or connected lattice nodes with $\Theta(\boldsymbol{x}) < \Theta_{\rm th}$ is defined as a white or black domain, in the language of morphological description. Two neighboring white and black domains present a clear interface or boundary. When the threshold $\Theta_{\rm th}$ is increased from the lowest to the highest values of Θ in the system, the white area A will decrease from 1 to 0; the boundary length L first increases from 0, then arrives at a maximum value, and finally decreases to 0 again. There are several ways to define the Euler characteristic χ. Two simplest ones are as below:

$$\chi = N_{\rm W} - N_{\rm B}, \tag{32}$$

or

$$\chi = \frac{N_{\rm W} - N_{\rm B}}{N}, \tag{33}$$

where $N_{\rm W}$ ($N_{\rm B}$) is the number of connected white (black) domains, N is the total number of lattice nodes with $\Theta(\boldsymbol{x}) < \Theta_{\rm th}$. The only difference of the two definitions is that the first keeps χ an integer. In contrast to the other two Minkowski functionals, white area A and boundary length L, what the Euler characteristic χ describes is the connectivity of the domains in the lattice. It describes the pattern or structure in a purely topological way, i.e., without referring to any kind of metric. It is clear that it is negative (positive) if many disconnected black (white) regions dominate the pattern or structure. The smaller the Euler characteristic χ, the higher the connectivity of the structure with $\Theta(\boldsymbol{x}) \geqslant \Theta_{\rm th}$ or $\Theta(\boldsymbol{x}) < \Theta_{\rm th}$. Specifically, for the first definition, the integer $\chi = -1$ in the case with only black drop in a large white lattice, and $\chi = +1$ vice versa, since the surrounding white (black) region does conventionally not count. In our work, only the second definition is used. What the ratio, $\kappa = (N_{\rm W} - N_{\rm B})/(NL)$, describes is the mean curvature of the boundary line separating black and white domains. Even though the Euler characteristic χ has a global meaning, it can be calculated in a local way via the additivity relation [54]. When the number of white regimes dominates, $\chi > 0$; else, $\chi < 0$. Figure 1 shows an example of two-dimensional patterns, where the z-axis corresponds to a physical quantity Θ under consideration, x- and y-axes show the two-dimensional coordinates. Figure 2 shows the white and back domains and schematic morphological characterizations.

The morphological characterizations of some physical fields, for example, the temperature field and density field, can be used to study the effects of material properties such as the porosity and effects of shocking strengths, etc. They can also be extended to investigate possible correlations and similarities occurred in various shocking processes. Because all the morphological properties of a pattern in D-dimensional space are contained in the $D+1$ morphological quantities, one can consider the morphological properties of the pattern in a $D+1$-dimensional space opened by the $D+1$ morpho-

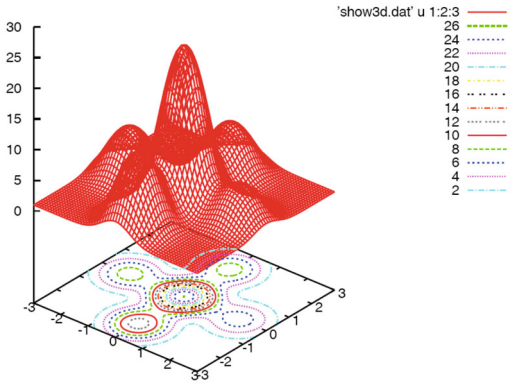

Figure 1 (Color online) An example of two-dimensional patterns, where the z-axis corresponds to a physical quantity under consideration, x- and y-axes show the two-dimensional coordinates.

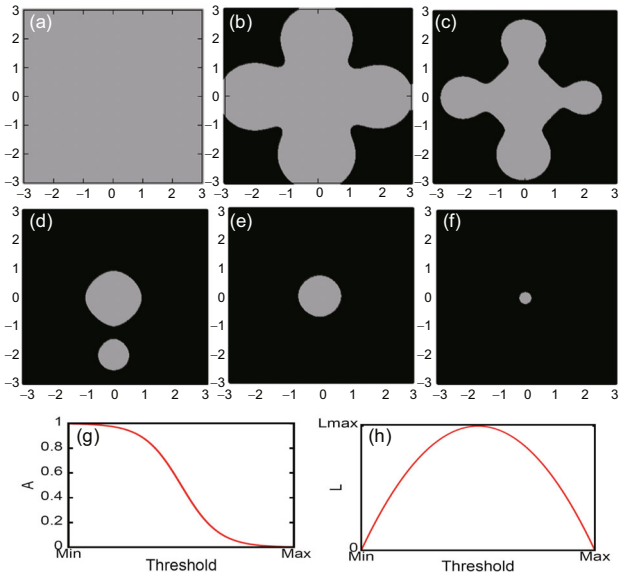

Figure 2 (Color online) Schematics of morphological characterizations. From (a) to (f) one can find that the white area A decreases and the topology of the patten changes with increasing the threshold value $\Theta_{\rm th}$. (g) shows the schematic curve for A versus $\Theta_{\rm th}$. (h) shows schematically the variation of boundary length L with $\Theta_{\rm th}$.

logical quantities. In this $D+1$-dimensional space one point corresponds to all the morphological behaviors of a pattern. The distance d between two points in this space presents a coarse-grained description of the difference of the two patterns. The shorter the distance d, the higher the similarity between the morphological properties of the two corresponding patterns. So, we can define a new quantity named structure similarity as $S = 1/d$. (See Figure 3 for a schematic.) If the two patterns evolve with time, then we can go a further step to define a dynamical similarity for the two pattern evolution processes from time t_1 to t_2,

$$S_D = \int_{t_1}^{t_2} d\,(t)\,{\rm d}t/\,(t_2 - t_1)\,.$$

Specifically, for patterns in the two-dimensional space, the difference of the morphological properties of pattern 1 and pattern 2 can be coarsely described by

$$d = \sqrt{(A_2 - A_1)^2 + (L_2 - L_1)^2 + (\chi_2 - \chi_1)^2},$$

where the subscript is the index of the pattern. (See Figure 4 for a schematic.)

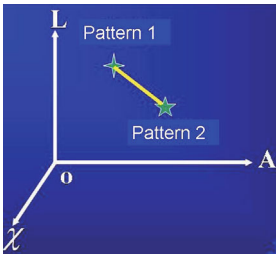

Figure 3 (Color online) Morphological properties of two patterns in the space opened by the morphological quantities.

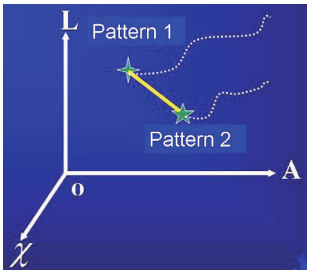

Figure 4 (Color online) Evolution of the morphological properties with time.

3.2 For fields and structures based on disordered points

Structure analysis is the core issue in studies on material simulation and material dynamics. The micro-structures in metal material may be composed of defect atoms deviating from the crystal lattices. In principle, the defect atoms can be identified by analyzing the regularity of their neighboring atoms. The distribution of the defect atoms in space is generally disordered. It is necessary to find an efficient algorithm for identifying and analyzing these structures. These complex algorithms include various searching schemes. In scheme design and in coding, based on the defect atoms, the identification of high dimension structures like dislocations, grain boundaries and voids requires to construct the so-called line, surface and body. A General Index of Spatial Objects (GISO) was designed in our group in the past years. In this section we introduce the GISO software and its applications in structure analysis on various micro-structures [51, 52].

3.2.1 Outline of GISO

Complex computations of relation between particles are inevitable in any elaborate defect identification methods. The computation time will dramatically increase with growing the system size in traditional methods. Without indexing the spatial objects, the computation quantity for searching object is generally very large. If a system contains N objects, the computation complexity related to two objects is N^2 and that related to three bodies is N^3. In the case where the total number of objects is more than 10^4, the computation complexity will not be acceptable. In such a case, schemes for effective storage and fast search of objects are crucial. To obtain such a scheme, it is necessary to design new data structure and indexing algorithm which significantly reduce the computation complexity. The computation complexity in defect identification methods can be greatly reduced by using background grid and linked list. The background grid index, together with the linked list data structure, is suitable for managing uniform distributed points. It has been extensively used in computation and analysis of many simulation results. Complex structure in non-uniform system refers not only to points, but also to lines, surfaces and bodies. Their distributions in space are

usually non-uniform. The background grid index cannot satisfy the needs for managing these objects, but a multi-level division of space is much more effective. The Space Hierarchy Tree (SHT) is a newly proposed data structure. It is a powerful dynamical management framework for any complex objects in any dimensional space. Based on the SHT, index of objects with complex structure can be created. Corresponding fast searching schemes can also be designed to satisfy various searching requirements.

SHT management structure The SHT data structure is similar to octree in the three-dimensional space. Go a further step, for a system in n-dimensional space, an n-dimensional cube is designed to contain the system. It is a line segment in one-dimensional space, a rectangle in two-dimensional space, and a cube in three-dimensional space, and so on. Divide each dimension of this tube into two parts. 2^n sub-cubes are formed, but only retain the cubes with objects inside. Continue to decompose each cube until the required resolution is reached. Put the objects (points, lines, surfaces, bodies) into the appropriate cubes according to their locations and sizes (see Figure 5). Connect the retained cubes together according to their belonging relationships. Thus, a "spatial hierarchy tree" is constructed (see Figure 6).

In practical applications, the SHT is constructed dynamically because the number of objects may be variable. The dynamic management procedure of SHT consists of the following three basic operations: (i) establishment of a tree, (ii) adding a new object to a tree, (iii) removing an object from a tree. The regimes managed by SHT is dynamically altered during these operations. In managing various objects with drastically different sizes and extremely scattered distributions, the SHT shows its effectiveness.

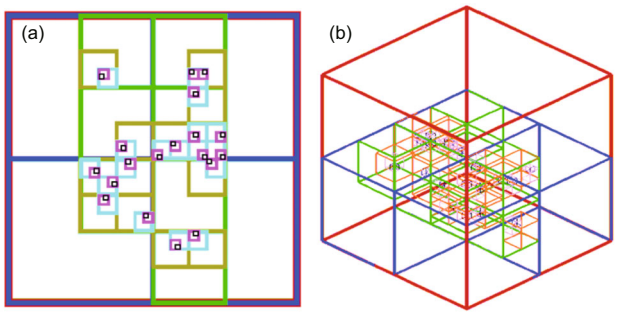

Figure 5 (Color online) Scheme for management region of SHT of discrete points. (a) Two-dimensional points; (b) three-dimensional points. (Adopted with permission from ref. [51]. The grey-level version is published in ref. [52].)

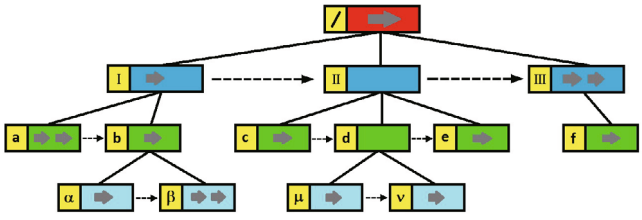

Figure 6 (Color online) Scheme for object management by SHT. The rectangle in each row stands for cube, horizontal grey arrow stands for object, and vertical black arrow stands for the list which connects the sub-cubes belonging to a same cube. (Adopted with permission from ref. [51].)

3.2.2 *Fast searching algorithms based on SHT*

One generally needs a fast search of objects satisfying certain requirements in practical application. For an ergodic search, the computational complexity is N. It is evidently not practical to treat with a huge number of objects. In such cases, one needs to design fast searching algorithms. With the management of SHT, fast searchers with computational complexity $\ln N$ can be easily created. The basic idea is as follows: do not search the objects directly, but rather check cubes and skip those cubes without objects. In this way, the searching is limited to a substantially smaller range. According to the requirements of applications, two fast searching algorithms are proposed. The first is referred to as conditional search, and the second is referred to as minimum search. The conditional search is to search for objects meeting certain conditions. For example, to find objects in a given area. The minimum search is to search for objects whose function values are minimum. For example, to find the nearest object to a fixed point.

Conditional search The basic idea is as follows: From the largest cube to the smallest, hierarchically check whether or not a cube contains objects meeting given conditions. If not, skip the cube (including all sub-cubes of it and corresponding objects).

In the searching process, only two operations are relevant to space dimension and type of object. The two operation are as follows: (i) to check whether or not an object is the needed one, or (ii) to check whether or not an cube is a candidate. Thus, the algorithm can be built in the abstract level. The conditional search is implemented via providing a conditional function and an identification function. The conditional function is used to check whether or not an object is needed. Assuming *condition(o)* is the conditional function, the argument o is object and the function value is a bool number. The identification function is used to assess whether or not a cube is a candidate. Assuming *maycontain(b)* is identification function, the argument b is cube and the function value is also a bool number. After defining the above two functions, conditional searching meeting any given conditions can be easily implemented.

Minimum search One often needs to find objects satisfying some given extreme condition in programming related to spatial objects. For example, to find a point with the largest z component from a set of three-dimensional points, or to search a point with the nearest distance to a given point, or to search a sphere closest to a plane, etc. Such searches can be classified to the minimum searching problem. For spatial objects, each one can be assigned a function value related to its location and size in such a way that the minimum search

becomes to find the object with the minimum function value.

Corresponding fast searching scheme can be designed based on the SHT. The basic idea is as follows: Design a function to assess the range of the function values of all possible objects in a cube which has certain position and size. Via comparing the ranges of the function value of different cubes, some cubes can be excluded. For example, Σ is a set of discrete points in a region, one needs to search the nearest points to a given point, A. The fast searching is not to calculate the distance between each point in Σ and the point A, but assess the range of distance between 'cubes' and point A to exclude unnecessary searching of cubes (including the point in them and their sub-cubes) with longer distance.

In minimum search, except for calculating the function value of an object and the range of a cube, other operations have nothing to do with space dimension and type of object, so that the algorithm can also be built in abstract level. Similar to case of conditional search, the minimum search is implemented via providing a value-finding function and range-evaluation function. The value-finding function is to calculate the function value of an object. Assuming *value(o)* is value-finding function, the argument *o* is an object and the function value is a real number. The range-evaluation function is used to compute the range of a cube. Assuming *M(b)* is the upper limit and *m(b)* is the lower limit of the range, the argument of function is cube *b* and the function value is a real number. After defining the above two functions, various minimum searches can be easily implemented.

3.2.3 Applications of GISO

We first illustrate the algorithm of rolling-ball method to construct spatial surface. For other applications of GISO, only the basic ideas are briefly reviewed.

Rolling-ball method for finding interfaces On a regular grid, the most common method to find interface of physical domain is to use the contour of the corresponding physical field. This method works well for the case where the discrete points closed to interface are uniformly distributed. When the distribution of discrete points is very complex, it is difficult to preserve the smoothness of the constructed interface. Consequently, the calculated interface will be significantly different from the actual one. A better means is to use the rolling-ball method. The basic idea of rolling-ball method is as follows: Roll a ball with fixed size over the discrete points; each rolling goes through three points, and these points constitute a surface element of interface. After the rolling-ball goes through the overall region, the physical interface is constructed.

In the rolling-ball method, the initial localization needs two searching schemes, and the rolling process needs the other two searching schemes. The four searching schemes are as follows.

(I) Minimum searcher MS1: Given a triangle face ABC and one of its edge AB, search in point tree for the first point met by the rolling-ball above triangle ABC, where the radius of rolling-ball is r and the rotation axis is AB. To construct the value-finding function, we first calculate the initial center $\boldsymbol{r}_o$ of the rolling-ball and the directions of local coordinate axes $\hat{\boldsymbol{x}}$, $\hat{\boldsymbol{y}}$, $\hat{\boldsymbol{z}}$ according to the following equations:

$$r^2 = (\boldsymbol{r}_O - \boldsymbol{r}_A)^2\,,$$
$$r^2 = (\boldsymbol{r}_O - \boldsymbol{r}_B)^2\,,$$
$$r^2 = (\boldsymbol{r}_O - \boldsymbol{r}_C)^2\,,$$

and

$$\hat{\boldsymbol{x}} = \frac{\boldsymbol{P}_{xy}\cdot(\boldsymbol{r}_O - \boldsymbol{r}_A)}{\left|\boldsymbol{P}_{xy}\cdot(\boldsymbol{r}_O - \boldsymbol{r}_A)\right|},$$
$$\hat{\boldsymbol{y}} = \hat{\boldsymbol{z}}\times\hat{\boldsymbol{x}},$$
$$\hat{\boldsymbol{z}} = \frac{\boldsymbol{r}_B - \boldsymbol{r}_A}{|\boldsymbol{r}_B - \boldsymbol{r}_A|},$$

where the subscript "o" indicate "old" and

$$\boldsymbol{P}_{xy} = \boldsymbol{I} - \hat{\boldsymbol{z}}\hat{\boldsymbol{z}}.$$

After the rotation, calculate the new center $\boldsymbol{r}_{\rm n}$ of the rolling ball and the corresponding local coordinates, x, y, z, according to the following relations:

$$r^2 = (\boldsymbol{r}_{\rm n} - \boldsymbol{r}_A)^2,$$
$$r^2 = (\boldsymbol{r}_{\rm n} - \boldsymbol{r}_B)^2,$$
$$r^2 = (\boldsymbol{r}_{\rm n} - \boldsymbol{r}_P)^2,$$

and

$$x = \hat{\boldsymbol{x}}\cdot(\boldsymbol{r}_{\rm n} - \boldsymbol{r}_A)\,,$$
$$y = \hat{\boldsymbol{y}}\cdot(\boldsymbol{r}_{\rm n} - \boldsymbol{r}_A)\,,$$
$$z = \hat{\boldsymbol{z}}\cdot(\boldsymbol{r}_{\rm n} - \boldsymbol{r}_A)\,,$$

where the subscript "n" means "new". Calculate the rotation angle, i.e. the value of value-finding function.

$$\text{value}(P) = \arctan 2(y, x).$$

Figure 7 shows the scheme for the rotation of triangle ABC. The procedure for constructing range-evaluation function is as follows: calculate the position $\boldsymbol{r}_T$ of the tangent point T of rolling-ball and the circumsphere of the cube b. The needed relations are as below:

$$r^2 = |\boldsymbol{r}_T - \boldsymbol{r}_A|^2 = |\boldsymbol{r}_T - \boldsymbol{r}_B|^2,$$
$$|\boldsymbol{r}_T - \boldsymbol{c}_b| = r + \sqrt{3}d_b.$$

$\boldsymbol{r}_T$ has two roots, $\boldsymbol{r}_{ML}$ and $\boldsymbol{r}_{mL}$. The corresponding tangent points are ML and mL. The range-evaluation functions are as follows:

$$M(b) = \begin{cases} \text{value(ML)}\,, & \text{if above equations have real solutions} \\ \infty, & \text{else,} \end{cases}$$

$$m(b) = \begin{cases} \text{value(mL)}, & \text{if above equations have real solutions} \\ \infty, & \text{else.} \end{cases}$$

Figure 8 shows the cross section picture for two different cases. In each case, the circumspheres of cube b and the rolling-ball are tangent to each other. Here, the back circle is for the circumsphere of cube b. The blue, green and red circles are for rolling-balls. ML and mL are for corresponding tangent points. The rotation angle of rolling-ball takes its smallest value when the tangent point is ML. It takes its maximum when the tangent point is mL.

(II) Minimum searcher MS2: Given a point $\boldsymbol{r}_0$, search for its nearest point P in point tree. The value-finding function is

$$value(P) = |\boldsymbol{r}_P - \boldsymbol{r}_0|,$$

where $\boldsymbol{r}_P$ is coordinate of point P. The range-evaluation functions are

$$M(b) = |\boldsymbol{c}_b - \boldsymbol{r}_0| + \sqrt{3}d_b,$$
$$m(b) = \max(|\boldsymbol{c}_b - \boldsymbol{r}_0| - \sqrt{3}d_b, 0).$$

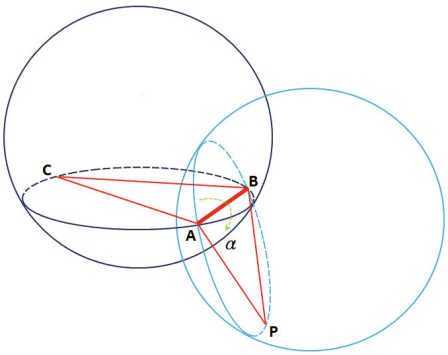

Figure 7 (Color online) Scheme for the rotation of triangle ABC. (Adopted with permission from ref. [51].)

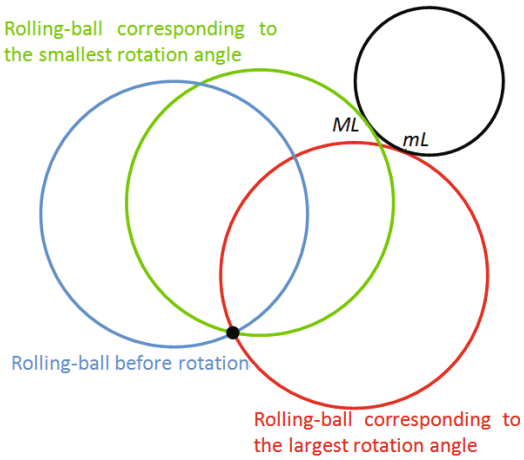

Figure 8 (Color online) Scheme for the two tangent cases between the rolling-ball and the circumsphere of cube b. (Adopted with permission from ref. [51].)

(III) Minimum searcher MS3: Given a point and a rotation axis, search for the first point met by the rolling-ball with fixed size in point tree. The algorithm is nearly the same as for MS1. We do not repeat here.

(IV) Conditional searcher CS1: Given two points, P1 and P2, search for segment BD, whose vertexes are P1 and P2, in segment tree. The conditional function is as follows:

$$maycontain(b) = \begin{cases} \text{true}, & \text{P}_1, \text{P}_2 \in S, \\ \text{false}, & \text{else.} \end{cases}$$

The circumsphere S of cube b is used for identification. The identification function is as follows:

$$s = \left| \sum_{i \in \text{neighbour}} (\boldsymbol{r}_i - \boldsymbol{r}_0) \right|.$$

The rolling-ball algorithm is as follows: (I) Initialization: Generate a point tree, *tp*, from given discrete points. Set the radius of rolling-ball as r and the center as P0. Using the searcher MS2 to search for the nearest point P1 of P0 in tree *tp*. Use searcher MS3 to search for a point P2 which is the first point met by the rolling-ball rotating around $\boldsymbol{x}$ axis in tree *tp*. Use searcher MS3 to search for a point P3 which is the first point met by the rolling-ball rotating around the direction of segment P1P2 in tree *tp*. Generate a triangle from P1, P2 and P3. Construct a triangle tree *tt* and a segment tree *tb*. Put the triangle P1P2P3 into *tp* and put its three edges into *tb*. (II) Interface construction: Check whether or not the tree *tb* is null. If yes, exit. If not, cut down an edge AB of triangle ABC. Use the searcher MS1 to search, in tree *tb*, for a point P to make smallest the rotation angle of circumsphere of triangle ABC. Here, AB is the rotation axis. Construct a triangle BAP, and put it into the triangle tree *tt*. Use CS1 searcher to search, in tree *tb*, for an segment L whose vertexes are point B and P. If L exists, cut it down from *tb*, and then delete it. If not, generate an segment PB and put it into *tb*. Perform the same operations to points P and A. (III) Go back to step (II). The surface composed of triangles contained in the tree *tt* is just the physical interface that we need.

The interface of voids constructed from discrete points is shown in Figure 9. The process of constructing interface of voids from discrete points is shown in Figure 10.

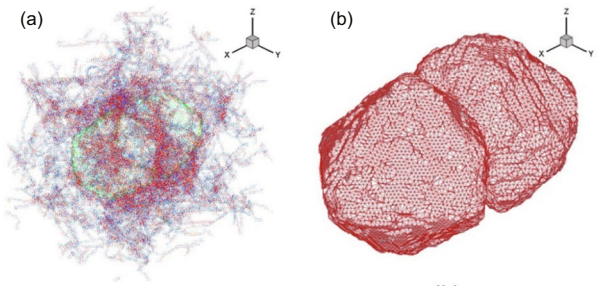

Figure 9 (Color online) Interface of voids constructed from discrete points. (a) Discrete points; (b) constructed interface. (Adopted with permission from ref. [51].)

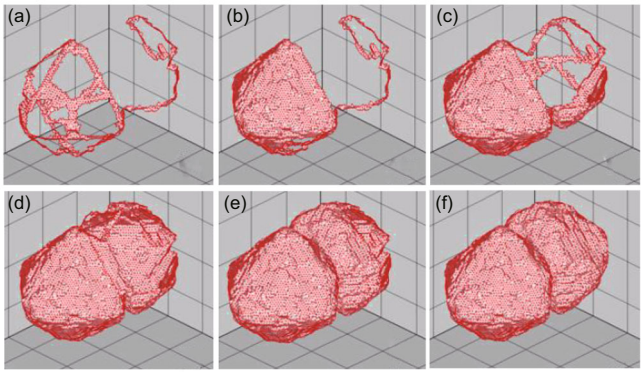

Figure 10 (Color online) Process of constructing interface of voids from discrete points. (Adopted with permission from ref. [51].)

Delaunay division There have been a number of algorithms to construct Delaunay triangles in two-dimensional space and tetrahedrons in three-dimensional space. The complexities of most algorithms come from the searching procedures of disordered data. Here, we introduce an algorithm based on the GISO. The algorithm is simple and intuitive. It is convenient to extend to higher dimensional space. The algorithm for constructing Delaunay division from discrete points is as follows: Firstly, create a point tree *tp*, put all the points into *tp*. The largest cube of the *tp* is centered at r_0 and has the size *a*. Construct a largest tetrahedron *T* which contains all the points in the local region. This tetrahedron is just the most initial Delaunay tetrahedron. This tetrahedron can be chosen as regular tetrahedron centered at r_0 with enough large size, e.g. 20*a*. This ensue that all the points in the tree *tp* are within *T*. Create a tetrahedron tree *tt*, put the first tetrahedron *T* into the tree *tt*. Secondly, add each point to adjust the Delaunay division. Take off a point P from *tp*, search the tetrahedrons in *tt* whose circumsphere contains P. We use a set, Q, to denote all the tetrahedrons checked out in above procedure. The tetrahedrons of Q forms a polyhedron. Remove these tetrahedrons from *tt*. Construct new tetrahedrons by linking each triangle surface of the polyhedron and point P. Put these new tetrahedrons into *tt*. Remove point P from *tp*. Repeat the procedure until *tp* is null. Finally, search for the tetrahedrons which share surface with T, and remove them from *tt*. Then, the all the tetrahedron in the *tt* construct the Delaunay division.

Figure 11 shows the steps for adding a two-dimensional point and re-dividing the space, where the red point stands for the newly added point P, the green triangles in Figure 11(a) are for the to-be-adjusted-triangles, the red segments in Figure 11(b) are retained boundary segments, the blue segments in Figure 11(c) are segments connecting point P and vertexes of boundary. In the three-dimensional case, we need only to replace the triangle with a tetrahedron, replace the line with a triangular face, and replace the triangle with a tetrahedron. Figure 12 shows the Delaunay division constructed from randomly distributed discrete points in a three-dimensional spherical region.

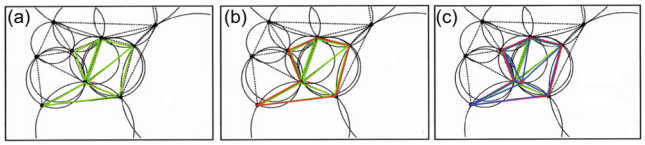

Figure 11 (Color online) Three steps to add a new point to a two-dimensional Delaunay division. (a) Finding the triangles whose circumcircle contains the newly added point P; (b) removing the internal lines of these triangles, retaining the external ones; (c) connecting each left line with point P to form new triangles. (Adopted with permission from ref. [51]. The grey-level version is published in ref. [52].)

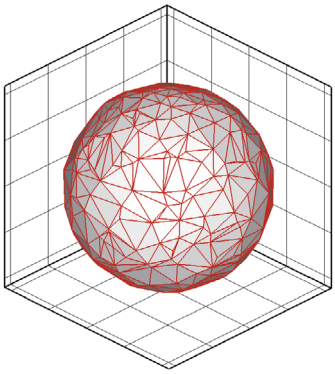

Figure 12 (Color online) Delaunay division constructed from randomly distributed discrete points in a three-dimensional spherical region. (Adopted with permission from ref. [51]. The grey-level version is published in ref. [52].)

Cluster construction and analysis method For discrete points, a cluster are defined as a group of points which have short distance. The critical distance is denoted as *d*, which is also the minimum distance between any two clusters. The algorithm to construct a cluster is as follows: Firstly, construct tetrahedron tree *tt* containing Delaunay tetrahedrons using the Delaunay division algorithm. Search in *tt* for the tetrahedron whose smallest edge is longer than *d*, and remove them from *tt*. Divide the remaining tetrahedrons in *tt* into different sets according to their connectivities. Create a cluster tree *tcl* to contain all the clusters. Secondly, create a tetrahedron tree *tc* to contain all the tetrahedrons in the first cluster. For convenience of description, *tc* is also referred to as a cluster. Create a triangle tree *ttr* to contain the inner surfaces of the clusters. Take off one tetrahedron T off *tt*, put T into *tc*, put each of its four triangle surfaces into *ttr*. Take off triangle *tr* from *ttr*, search in *tt* for the tetrahedron, say T1, whose triangle surface coincides with *tr*. If find T1, remove it from *tt* and put it into cluster *tc*. Put all the surfaces except *tr* into *ttr*. Repeat the procedure until *ttr* is null. Up to this step, the first cluster *tc* is completely constructed. Put the cluster *tc* into cluster tree *tcl*. Then, construct a new cluster and put it into *tcl* until *ttr* is null.

Figure 13 shows the clusters constructed with random points in two-dimensional space.

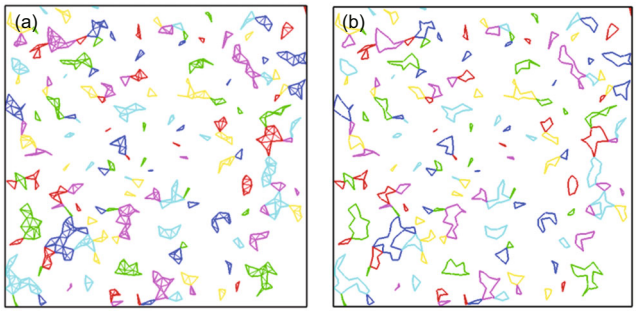

Figure 13 (Color online) Cluster structure formed from 1000 random discrete points in a two-dimensional square area [0,1]×[0,1]. (a) A cluster; (b) the corresponding cluster boundary. (Adopted with permission from ref. [51]. The grey-level version is published in ref. [52].)

Identification methods of defect atoms Here we introduce three methods.

(1) Excess energy method

In this method, the defect atoms are defined as those whose potential energies exceeds a critical value. This method requests that the MD simulation outputs not only atom positions but also the inter-atomic potentials.

(2) Centro-Symmetry Parameter method

In Centro-Symmetry Parameter (CSP) method [58], the geometrical symmetry of the collection of nearest atoms of an atom is used to identify defect atoms. All atoms in the perfect crystal are in the geometrical center of its nearest atoms, but the defect atoms are not. Therefore, an order parameter is defined as follows:

$$s = \left| \sum_{i \in \text{neighbour}} (\boldsymbol{r}_i - \boldsymbol{r}_0) \right|.$$

Atoms whose order parameter s is greater than a critical value s_c are defect atoms.

(3) Bond-pair analysis method

The CSP and excess energy methods can be used to distinguish defect atoms, but can not be easily used to identify types of the defects atoms. The bond-pair analysis (BPA) [59] based on local topological connections can be used to identify more accurately the atom type. The idea of BPA is as follows: The bond type is marked in terms of the connections among all the atoms bonding with the two atoms. An atom type is marked in terms of all the bonds of itself. Figure 14 shows the voids surfaces and dislocations identified by bond-pair analysis.

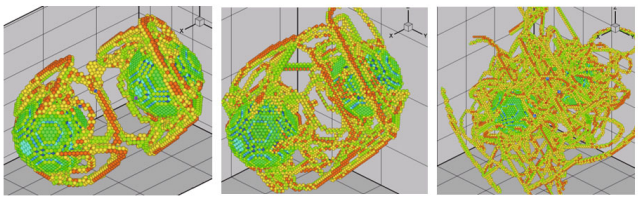

Figure 14 (Color online) Voids surfaces and dislocations identified by bond-pair analysis. (Adopted with permission from ref. [51].)

Packing-sculpting method for constructing object surface In computational geometry, it is an important issue to construct object surface from disorder points. The current algorithms can be categorized into four groups [60]: space partition method [61], distance function method [62], deformation method [63], and growth method [64]. Space partition is generally based on Delaunay division. The outer surface is generated by removing some Delaunay mesh in the sculpting method. The packing-sculpting method presented below is an intuitive method. The out surface is constructed by dynamically sculpting the packing convex hull. As for the packing, the basic idea is as follows: Firstly, create a point tree *tp*, and put all the points into the tree *tp*. Search in *tp* for the point P1 which has largest x-coordinate; remove P1 from *tp*. Define a plane passing P1 perpendicular to x-axis; rotate the plane around the axis which passes P1 and along the y direction; search for the first point P2 it meets; remove it from *tp*. Define a plane passing points P1 and P2; rotate the plane around P1P2; search for the first point P3 it meets. Remove P3 from *tp*. Create triangle P1P2P3 by linking P1, P2, P3. That is the first triangle surface. Create a triangle tree *tt*, and put triangle P1P2P3 into it. Create a boundary tree *tb* and put P1P2, P2P3, P3P1 into it. Secondly, take one boundary edge AB in *tb*, define a half plane which is on the same plane as the triangle surface passing AB. This half plane includes the region opposite to the triangle. Rotate the half plane around AB, search in *tp* for the point P it first meets. Create triangle BAP and put it into *tt*. Find in *tb* for each edge, AB, PA and BP. If find one, remove it from *tb*; if not, put its reverse edge, BA, AP or PB, into *tb*. Repeat the procedure until *tb* is null. In this way, all the packing surfaces are included in *tp*.

As for the sculpting, the basic idea is as follows: Define a size s which represents the sculpting depth. Firstly, create a triangle tree *ts* to contain triangle surface. Take a triangle surface ABC from surface tree *tt*. Define a sphere B which passes vertices A, B, C of triangle ABC and has a large enough radius, e.g., 10^{100}. Keep the sphere B passing the points, A, B and C, decrease the radius of B, search in *tp* for the first point P that sphere B meets. If P can not be found before the radius shrink to be less than s, it means that the sculpting from triangle surface ABC can not be done any more, remove ABC from *tt* and put it into *ts*. If P exists, the sculpting from triangle surface ABC can be done, remove ABC from *tt*. Find in *tt* for each Triangle surface, ABC, CBP, BAP and ACP. If find one, remove it from *tt*; if not, put its reverse triangle, BAC, CBP, ABP or CAP into *tt*. Repeat the procedure until *tt* is null. In this way, all the surfaces are included in *ts*.

The procedure of packing-sculpting algorithm is shown in Figure 15.

Calculation of the Burgers vector of dislocation loop Based on the Thompson's tetrahedron, a Frank scheme is developed to calculate the Burgers vector of dislocations in a fcc crystal during its plastic deformation. A Burgers circuit is located firstly in a deformed crystal with a reference cir-

cle surrounding one or more dislocations. The atom-to-atom sequence, in a dislocation-free crystal, corresponding to the Burgers circuit is determined from the edge vectors of the Thompson's tetrahedron and its mirrors, instead of a local reference lattice. The Burgers vector can be calculated via summing over the vectors connecting neighboring atoms in the Burgers circuit. As long as the same dislocations are surrounded, the final Burgers vector obtained by its Frank definition is accurate. The present method is validated in determining the Burgers vectors for the dissociation of a perfect dislocation and for the complex reactions of the dislocations from a nanovoid in a deformed crystal under a uniaxial tensile loading [65] (see Figures 16 and 17).

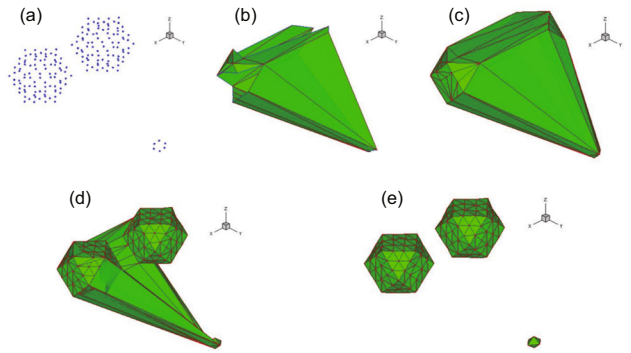

Figure 15 (Color online) The procedure of packing-sculpting algorithm. (a) Discrete points; (b) the mid of packing procedure; (c) packing convex hull; (d) sculpting procedure; (e) object surface. (Adopted with permission from ref. [51].)

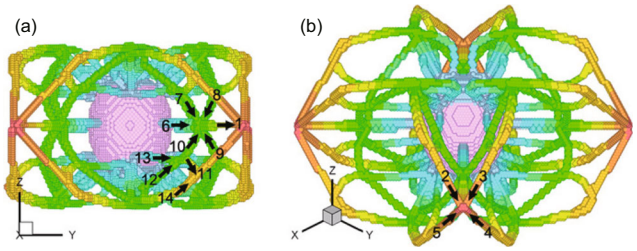

Figure 16 (Color online) Burgers vectors for dislocations from a nanovoid in a deformed crystal under a uniaxial tensile loading. (a) Front view; (b) perspective view. The colors are based on the distance to the void center. Specifically, $\boldsymbol{b}_1 = [0,0,0]$; $\boldsymbol{b}_2 = [1,2,-1]/6$; $\boldsymbol{b}_3 = [-2,-1,1]$; $\boldsymbol{b}_4 = [2,1,1]/6$; $\boldsymbol{b}_5 = [-1,-2,-1]/6$; $\boldsymbol{b}_6 = [0,0,0]$; $\boldsymbol{b}_7 = [-1,1,-2]/6$; $\boldsymbol{b}_8 = [-1,1,2]/6$; $\boldsymbol{b}_9 = [1,-1,2]/6$; $\boldsymbol{b}_{10} = [1,-1,-2]/6$; $\boldsymbol{b}_{11} = [-2,-1,1]/6$; $\boldsymbol{b}_{12} = [1,-1,-2]/6$; $\boldsymbol{b}_{13} = [-2,-1,1]/6$; $\boldsymbol{b}_{14} = [1,-1,-2]/6$. (Adopted with permission from ref. [65].)

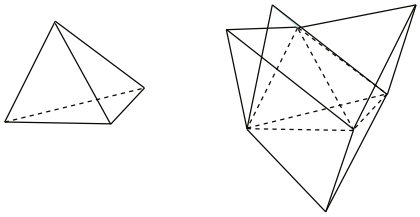

Figure 17 Thompson's tetrahedron and its mirrors. (Adopted with permission from ref. [51].)

4 Numerical experiments and observations

Our investigations can be roughly classified into three groups, microscopic, mesoscopic and macroscopic scales. As for the microscopic scale, what we probed are limited to the cases which can be simulated by the MD simulations. As for the mescoscopic scale, both the solid and fluid models are used. Based on the solid model, what we probed are limited to the cases with only one or a few cavities where the continuum theory works and the MPM can be used. The fluid model here is mainly referred to the DBM. By using the DBM, we can study both the hydrodynamic non-equilibrium and thermodynamic non-equilibrium behaviors, especially around the interfaces. Both the MPM and DBM are also applied to simulate behaviors in the macroscopic scale.

4.1 MPM investigations: Global behaviors

The global behaviors of shocked porous material based on MPM simulations are referred to those averaged or statistical behaviors [48-50, 66-68]. Here "global" is relative to "local". The latter is referred to the case with only a single or a few cavities, while the former is referred to the case with several thousands or more. In our numerical experiments the porous material is fabricated by a solid material body with an amount of cavities randomly embedded. The particle feature of MPM makes easy the flexible setting of the initial configuration. We denote the mean density of the porous body as ρ and the density of the solid portion as ρ_0. The porosity is defined as $\Delta = 1 - \delta$, where $\delta = \rho/\rho_0$. The porosity Δ is controlled by the total number N_{void} and mean size r of voids embedded. In our numerical experiments, there are two kinds of equivalent shock loading schemes, colliding with a body with symmetric configuration or colliding with a rigid wall in the same material. In the studies on global behaviors, the shock is loaded via colliding with the rigid wall. In the studies on local behaviors, the shock is loaded via colliding with a body with symmetric configuration. The gravity effects are neglected. The rigid wall is located horizontally and keeps static at the bottom where $y = 0$, the target porous body is on the upper side of the rigid wall and moves towards the rigid wall at a velocity with the size v_{init}. We start to count the time when the porous body begins to touch the rigid wall. At the left and right boundaries we use periodic boundary conditions. This treatment means that the real system under consideration is composed of many of the simulated ones aligned periodically in the horizontal direction.

The sample material for MPM simulations in this paper is fixed at the metal aluminum. The corresponding parameters are as follows: $E = 69$ MPa, $\nu = 0.33$, $\rho_0 = 2700$ kg/m^3, $\sigma_{Y0} = 120$ MPa, $E_{\tan} = 384$ MPa, $k = 237$ W/(m·K), $c_0 = 5.35$ km/s, $\lambda = 1.34$, $c_v = 880$ J/(kg·K) and $\gamma_0 = 1.96$ when the pressure is below 270 GPa. The initial temperature of the material is fixed at 300 K.

4.1.1 Mean values and their fluctuations

In this part of the studies, the effects of porosity and shock strength are the main concerns. For cases with the same porosity, the effects of mean-cavity-size are further studied. Main observations are as follows: the local volume dissipation and turbulence mixing are two important mechanisms for transformation of kinetic energy to internal energy. In the cases with very small porosities, the shocked portion may arrive at a dynamical steady state; the cavities within the downstream portion reflect back rarefactive waves and make slight oscillations of mean density and pressure; in the cases with the same porosity, a larger mean-cavity-size results in a higher mean temperature. In the cases with high porosities, the hydrodynamic quantities vary with time during the whole shock-loading procedure: after the initial period, the mean density and pressure decrease, but the temperature increases with a higher rate. The distributions of local pressure, temperature, density and particle-velocity are generally non-Gaussian and vary with time. The changing rates are dependent on the shock strength, porosity value as well as the mean-cavity-size. The porosity effects become more pronounced with increasing shocking strength [50]. We show some specific numerical results based on two-dimensional simulations below.

The computational unit here is 2 mm in width, as shown in Figure 18. Since mainly interested in the loading procedure, the height of porous material is set a large enough value so that the rarefactive waves reflected from the upper free surfaces do not significantly influence the physical process within the time scale under investigation.

Two snapshots are shown in Figure 18, where Figure 18(a) shows the contour of pressure and (b) shows the contour of temperature. Different from the cases with perfect solid material, no stable shock wave exists in the porous materials. When the initial shock wave arrives at the first cavity, rarefactive wave is reflected back and propagates within the compressed portion, which destroys the original possible equilibrium state there. The shock waves at the two sides continue to propagate forward and meet again in front of the cavity. The waves begin to become complex. When a compressive wave meets a new cavity, similar behaviors occur. In this way, the waves in the porous material become very complex. For the convenience of description, the concept, shock wave, is still used as a coarse-grained description. Correspondingly, the values of physical quantities, such as the pressure, the particle velocity, temperature, density, etc, are corresponding mean values calculated in a region Ω with $y_1 \leqslant y \leqslant y_2$.

Cases with low porosity Figure 19 shows the mean density, pressure, temperature and particle velocity versus time for a case where $\Delta = 0.029$ ($\delta = 1.03$), $r = 50$ μm, $v_{\text{init}} = 1000$ m/s and the height of the porous material is 5 mm. These values are dynamically measured in a bottom and a top domains, respectively. For the bottom domain, we choose $y_1 = 100$ μm, and for the top domain, y_2 takes the y-coordinate of the highest material-particle. Three sets of measured results are shown. The heights of the measured domain are chosen as $h = 800$, 400 and 100 μm, respectively. The lines with solid symbols are for measured values from the bottom domain, the lines with empty symbols show measured values from the top. Simulation results show that, for the case of $h = 800$ μm, when the shock waves propagate within the bottom domain Ω_b, the measured mean density, pressure and temperature increase nearly linearly with time, up to about $t = 150$ ns. After that the temperature further to increase with a much lower increasing rate. The three quantities arrive at their first maximum values, 3.14 g/cm^3, 16.7 GPa, and 432 K, at about $t = 250$ ns. At this time the shock front has passed the downstream boundary of the measured domain (See Figure 18). The concave regions in the ρ-,P-,T-curves at about $t = 450$ ns shows an unloading phenomenon of the compressive waves, i.e., rarefactive waves reflect back from the cavities downstream neighboring to the measured domain. The values of ρ and P increase and recover to their (nearly) steady values after that, but the temperature further to increase. The secondary loading-phenomenon is due to the collisions of the upstream and downstream walls of cavities. During the following period the density and pressure keep nearly constants, while the temperature still increases very slowly. The weak fluctuations in the density, pressure and temperature curves after $t = 650$ ns result from the inputs of compressive and rarefactive waves from the two boundaries at the opposite sides of the measured domain Ω_b. The visco-plastic work by these wave series makes the temperature increase slowly. From the lines with empty symbols we can find that the shock waves arrive at the top free surface at about $t = 800$ ns. After that, rarefactive waves come back into the shocked material. Within the time interval shown in the figure, for the cases with $h = 800$ and 400 μm, the density (or pressure) recovers to a value slightly larger than its initial one, but the temperature is about 60 K higher than its initial value and still increases; for the case with $h = 100$ μm, evident oscillations are found in the curve of density after $t = 900$ ns. To understand better this phenomena, we show in Figure 20 the top portion of the configuration with temperature contour for the time $t = 1.15$ μs, from which we can find jetting phenomena at the upper free surface. From the same data used in Figure 18, we can obtain the mutual dependences of these hydrodynamical quantities. The initial transient stage and the final oscillatory steady state are clearly observable. Due to existence of the randomly distributed voids, waves with various wave vectors and frequencies propagate within the shocked material. When the measured domain becomes smaller, more detailed wave structures may be found. Figure 19 shows clearly this trend.

Figure 21 shows the standard deviations of the above four quantities measured in the bottom domains versus time. These quantities increase quickly with time at the initial stage, then decrease, nearly exponentially, to their steady values. The standard deviation of u_y is larger than that of u_x,

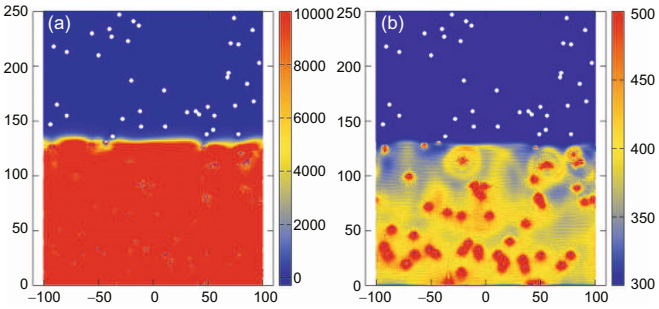

Figure 18 (Color online) Snapshots of the shocked porous metal. δ = 1.03, Δ = 0.029, t=250 ns. (a) Contour of pressure; (b) contour of temperature. The unit of length in this figure is 10 μm. From blue to red, the contour value increases. The unit of contour is MPa in (a) and is K in (b). The initial velocities of the flyer and target are $\pm v_{\text{init}}$ = ±1000 m/s in this case. (The grey-scale version is published in ref. [50].)

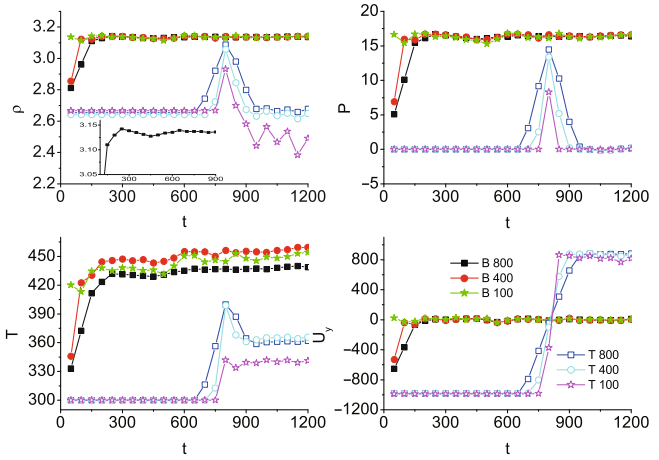

Figure 19 (Color online) Variations of mean density, pressure, temperature and particle velocity with time. The height of the measured domain are h = 800, 400 and 100 μm, respectively, as shown in the legends. "B" and "T" in the legends means the measured domains are at the bottom and top of the target body, respectively. The units of density, pressure, temperature, particle velocity and time are g/cm^3, GPa, K, m/s and ns, respectively. (The grey-scale version is published in ref. [50].)

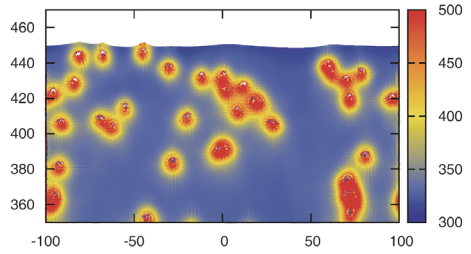

Figure 20 (Color online) Configuration with temperature contour at time t=1.15 μs. Other parameters are referred to Figures 18 and 19. The unit of temperature is K. (The grey-scale version is published in ref. [50].)

which means the system is out of the thermodynamic equilibrium and the internal energy in shocking degree of freedom is larger than in the transverse degrees of freedom. The non-zero values of these fluctuations confirm that the system is in a nearly steady state with local dynamical oscillations.

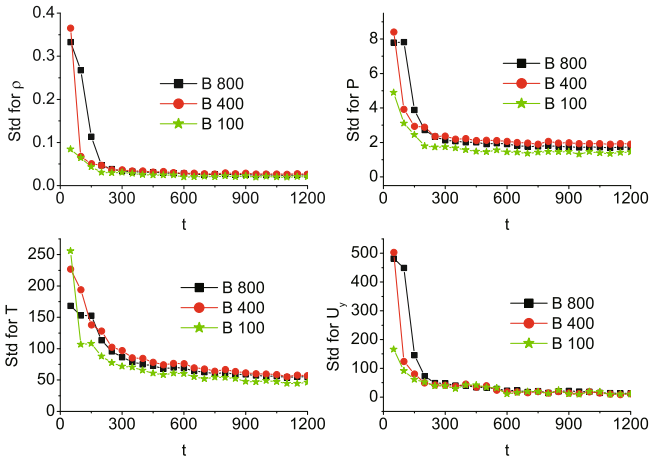

Figure 21 (Color online) Standard deviations (Std) of the local quantities averaged in various spatial scales. The heights of the measured domains are shown in the legends where "B" means the measured domains are at the bottom of the target body. The length and time units are μm and ns, respectively. (The grey-scale version is published in ref. [50].)

For the case where a perfect crystal material is shocked, the entropy production occurs only in the non-equilibrium zone induced by the shock wave. In the case of porous material, the high plastic distortion of the materials surrounding the collapsed cavities contributes extra entropy production. Therefore, we can roughly define a local rotation as:

$$\text{Rot} = |\nabla \times \boldsymbol{u}|,$$

and a local divergence as:

$$\text{Div} = |\nabla \cdot \boldsymbol{u}|.$$

Both the local rotation and divergence make significance sense in describing the dynamic process of porous material under shock. The local rotation, $|\nabla \times \boldsymbol{u}|$, describes the circular flow and/or turbulence. The divergence, $|\nabla \cdot \boldsymbol{u}|$, describes the changing rate of volume. Both of them work as important mechanisms of entropy production and temperature increase in dynamic responses of porous material. The former indicates the turbulence dissipation, and the latter indicates the shock compression. Figure 22 shows their mean values squared versus time. As a comparison, the behavior of strain rate ("StrR" in the figure) $\dot{\boldsymbol{\varepsilon}}$ is also shown. All the three quantities decrease, nearly exponentially, to their steady state values as shock waves pass the measured domain Ω. The amplitude of steady strain rate is very close to that of the rotation. The amplitude of the divergence is a little larger for this case. Cavity collapse and new cavitation by the rarefactive waves are the main contributors to the local divergence. Figure 23 shows a portion of the configuration with density contour, pressure contour, temperature contour and velocity field at time t = 750 ns, from which one can understand better the fluctuations of the local density, pressure, temperature, particle velocity and the finite values of the rotation and divergence.

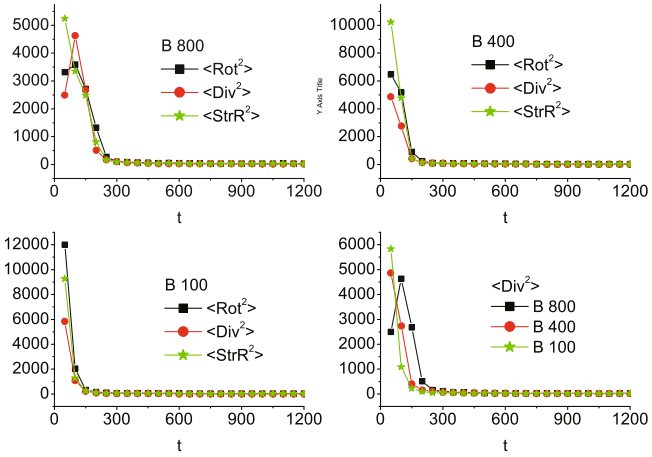

Figure 22 (Color online) Variations of the mean values squared of local rotation, divergence and strain rate with time. ⟨...⟩ in the legends denote the mean value of the corresponding quantity and "B" means the measured domains are at the bottom of the target body. The length and time units are μm and ns, respectively. (The grey-scale version is published in ref. [50].)

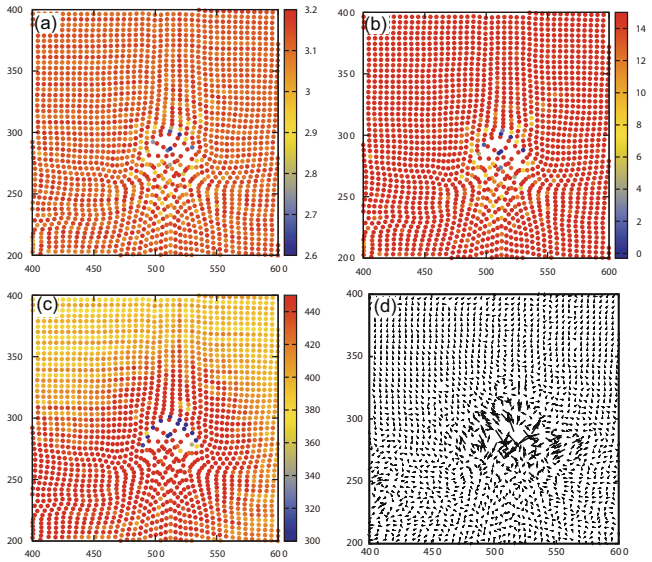

Figure 23 (Color online) Configurations with density contour (a), pressure contour (b), temperature contour (c) and velocity field (d) at time t=750 ns. The size of particle velocity is denoted by the length of arrow timed by 50. The units are the same as in Figure 19. (The grey-scale version is published in ref. [50].)

There is a void around the position (510 μm, 280 μm) in this case. To check the effects of the void size, results for different void sizes are shown and compared. The mean density, pressure and particle velocity in the steady state do not show evident differences. But the temperature shows significant dependence on the void size. Larger voids result in higher mean temperature (See Figure 24). As for influences of void size on the mean value squared of the local rotation and divergence, the void size make effects only in the transient period. See Figure 25, where the two cases correspond to different mean-void-sizes but the same value of porosity, $\Delta = 0.029$, are shown.

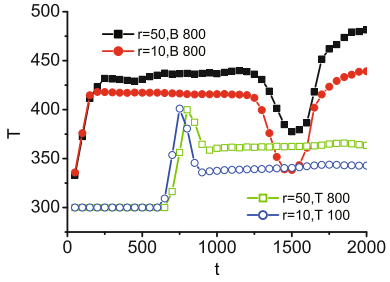

Figure 24 (Color online) Effects of the mean void size on the mean temperature. The mean void size r, position and height of the measured domain are shown in the legend. "B" and "T" means the measured domains are at the bottom and top of the target body, respectively. The length and time units are μm and ns, respectively. (The grey-scale version is published in ref. [50].)

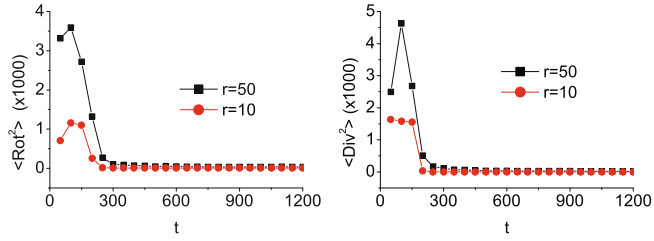

Figure 25 (Color online) Effects of mean void size on the mean values squared of local rotation, divergence. The mean sizes of void are shown in the legends. The length and time units are μm and ns, respectively. (The grey-scale version is published in ref. [50].)

Cases with higher porosity For the cases with higher porosity, we show the variations of mean density, pressure, temperature and particle velocity with time for the case with $\Delta = 0.286$, $\delta = 1.4$, $r = 10$ μm and $v_{\text{init}} = 1000$ m/s in Figure 26. Here only results averaged in the upper and bottom domains with the same hight, $h = 800$ μm, are shown. Different from the low-porosity case with $\delta = 1.03$, the mean density and pressure decrease with time, while the mean temperature increase with a higher rate after the initial stage. This is due to the rarefactive waves reflected back from the cavities in the downstream region. The rarefactive waves make looser the shocked material and result in a relatively higher local divergence. Consequently, more kinetic energy into heat. At the same time, a higher porosity means more cavities embedded in the material, more jetting phenomena may occur under shock. Both the jetting phenomena and the collisions of jetted materials with the downstream walls of cavities result in a significant increase of local temperature, local divergence and local rotation. Figure 27 shows the mean values squared of the local rotation, divergence and strain rate. During the initial transient period, the turbulence dissipation is the main mechanism for the temperature increase in this case. In the later steady state, all the three kinds of dissipations make nearly the same contributions.

To further clarify the inhomogeneity effects in the shocked regime, in Figure 28, we show the distributions of density, pressure, temperature and particle velocity at three times,

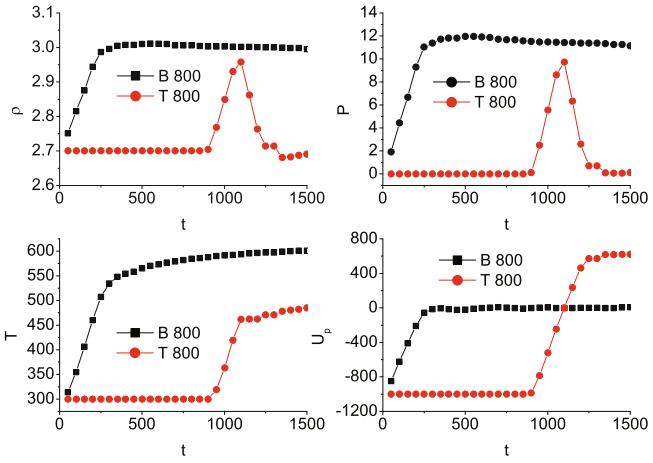

Figure 26 (Color online) Variations of mean density, pressure, temperature and particle velocity with time. Here $\delta = 1.4$, $\Delta = 0.286$, $v_{\rm init} = 1000$ m/s. The meanings of "B", "T" and units are the same as in Figure 19. (The grey-scale version is published in ref. [50].)

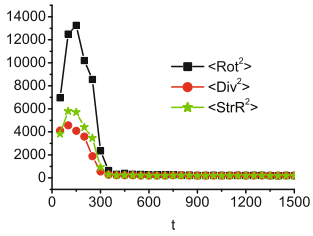

Figure 27 (Color online) Variations of the mean values squared of local rotation, divergence and strain rate with time. The unit of time is ns. (The grey-scale version is published in ref. [50].)

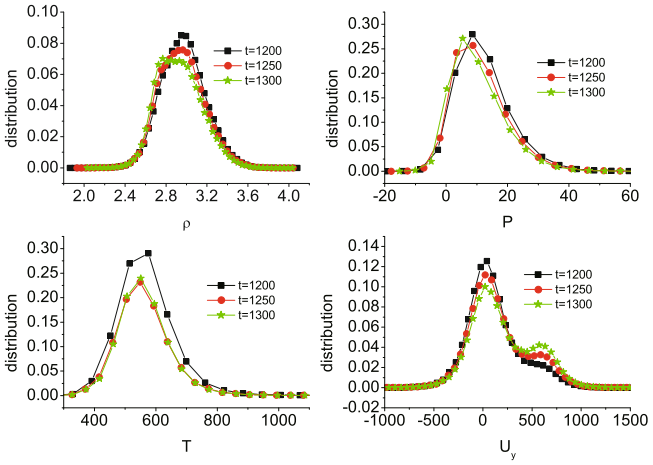

Figure 28 (Color online) Distribution of local density, pressure, temperature, particle velocity at various times. The units are the same as in Figure 19. (The grey-scale version is published in ref. [50].)

$t = 1200$, 1250 and 1300 ns. Their distributions generally deviate from the Gaussian distribution and vary with time. The effects of initial impact velocity on the mean density, pressure and temperature are shown in Figure 29. It is clear that the decreasing rate of the mean density and the increasing rate of mean temperature becomes larger as increasing the strength of the initial shock.

When study the porosity effects, we fix the shock strength. Figure 30 shows the mean density, and temperature versus time for various porosities. Here initial velocity $v_{\rm init} = 1000$ m/s. When the porosity is very small, the mean density decreases more quickly with increasing the porosity. But when the porosity is high, the mean density show more complex behaviors.

4.1.2 *Morphological analysis*

Morphological analysis describes the geometrical and topological properties of the fields of temperature, pressure, density, etc. Shock wave results in complicated series of compressions and rarefactions in the porous material. In the case of temperature field, A describes the fraction of high temperature particles. Its increasing rate roughly gives the velocity D of a compressive-wave series. The velocity D decreases with increasing the threshold value $T_{\rm th}$ of temperature. The fraction A increases, nearly parabolically, with time t during the initial period. The $A(t)$ curve shows more linearity in the following three cases: (i) when the porosity Δ approaches 0, (ii) when the initial shock becomes much stronger, and (iii) when the threshold value approaches the minimum value of the temperature. The fraction A of high temperature particles may continue to increase even after the early compressive waves have arrived at the downstream free surface

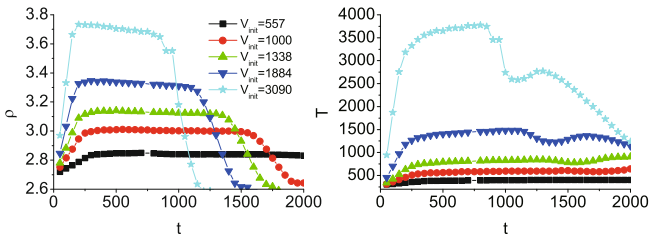

Figure 29 (Color online) Mean density and temperature versus time for various shock strengths. The initial velocity $v_{\rm init}$ are shown in the legend. The units are the same as in Figure 19. (The grey-scale version is published in ref. [50].)

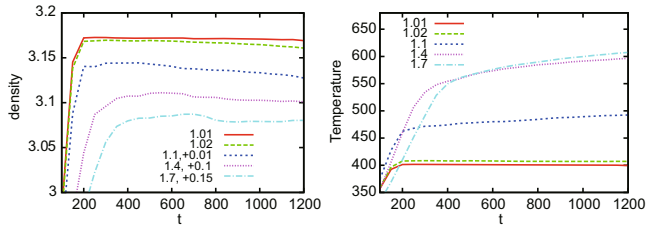

Figure 30 (Color online) Mean density and temperature versus time for various porosities. The values of δ, 1.01, 1.02, 1.1, 1.4, 1.7 are shown in the legends. In the left figure, the lines for cases with $\delta = 1.1$, 1.4 and 1.7 are moved upwards by 0.01, 0.1, and 0.15, respectively. The units are the same as in Figure 19. (The grey-scale version is published in ref. [50].)

and some rarefactive waves have come back into the material. In the case of energetic material needing a higher temperature for ignition, a higher porosity is preferred and the material may be ignited after the precursory compressive waves have scanned the entire material. In morphology analysis, the result dependence on experimental conditions is reflected simply by a few coefficients. Here we show some observations for the temperature field [48].

Basic observations A set of snapshots for a shock process are shown in Figure 31, where the contours are for the temperature. From blue to red, the temperature increases. The first two show the loading process. The last two are for the unloading process of the compressive waves. As mentioned in previous part, rarefactive waves are reflected back into the material when compressive waves reach the upper free surface. Under the tensional action of rarefactive wave, the height of the porous material increases with time. In fact, a large number of local unloading phenomena have occurred within the material before the compressive waves arrive at the upper free surface. The details of wave series are very complex, we use the Minkowski functionals to characterize the physical fields inside the material.

In this review, the morphological analysis is mainly for the temperature field. To use the Minkowski functionals, we first choose a threshold temperature $T_{\rm th}$ and condense the temperature field $T(\boldsymbol{x})$ into high temperature regions (with $T(\boldsymbol{x}) \geqslant T_{\rm th}$) and low temperature regions (with $T(\boldsymbol{x}) < T_{\rm th}$). Figure 32 shows the several sets of Morphological analysis for the shocking process shown in Figure 31. "DT" in the legend means $T_{\rm th} - 300$. The unit of temperature is K. The time unit is ns. One can find that, when DT is very small, the wave front is nearly a plane, which is similar to the case of uniform solid material. When $DT = 10$ K, the total fractional high temperature area A increases up to be nearly 1 at about the time $t = 1600$ ns and keeps this saturation value until the time $t = 2600$ ns, then shows a slight decreasing. This indicates that (i) the early compressive wave reaches the upper free surface at about the time $t = 1600$ ns, (in fact before that), (ii) nearly all material particles obtain a temperature higher than 310 K during the following 1000 ns period. In the unloading process a very small fraction of material particles decrease their temperature to below 310 K due to the action of rarefactive waves. The high temperature area A decreases with increasing the temperature threshold. In the case where $DT = 100$ K, at the time $t = 1900$ ns, the high temperature area gets a (nearly) steady value 0.96, which indicates that 4% of the material particles could not have a temperature higher than 400 K in the whole process during shown period. When the compressive wave arrives at a cavity, it is decomposed of many components. The components in the solid portion propagate forwards more quickly, while the portion facing cavity may result in jet phenomenon. When jetted material particles hit the downstream wall of the cavity, new compressive waves occur. At the meanwhile, the cavity reflects rarefactive wave back to the compressed regime. A large number of similar processes occur inside the shocked porous material. Thus, the shock loading process is manifested as successive actions of many compressive and rarefactive waves. The effects of compressive waves dominate during the shock-loading process.

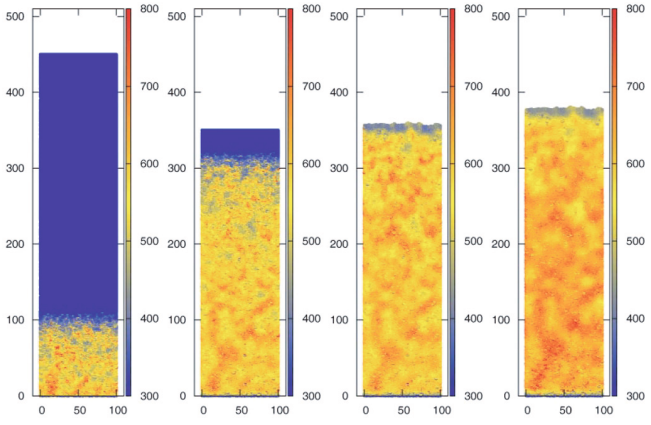

Figure 31 (Color online) Configurations with temperature contours. $\Delta = 0.5$ and $v_{\rm init} = 1000$ m/s. From left to right, t=500, 1500, 2000, and 2500 ns, respectively. The length unit here is 10 μm. (Adopted with permission from ref. [48].)

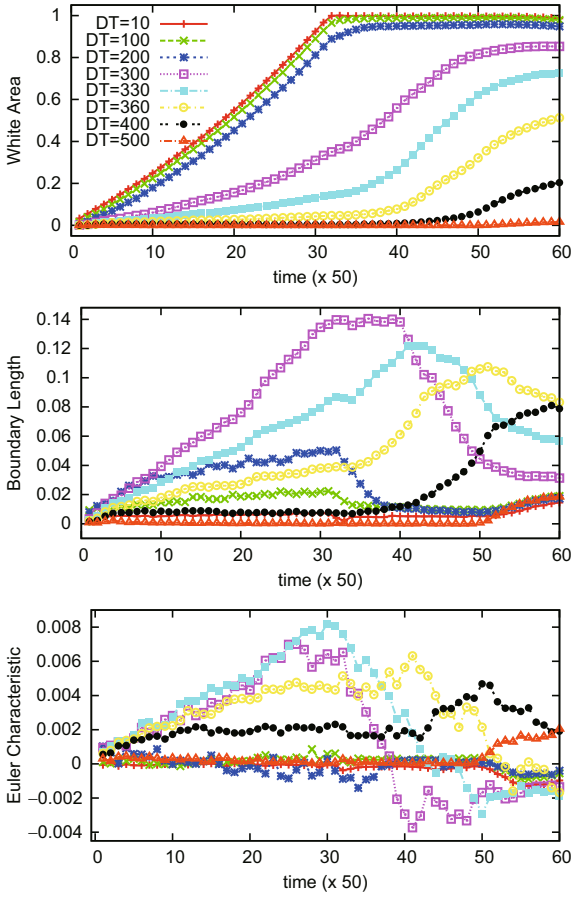

Figure 32 (Color online) Minkowski measures for the procedure shown in Figure 31. The contour levels of the temperature increment are shown in the legend. (Adopted with permission from ref. [48].)

All the plastic deformations contribute to the temperature increase. Similarly, one can interpret the curve for $DT = 200$ K. When DT increases from 200 K to 300 K, the curve of high temperature area shows a significant variation. For the case of $DT = 400$ K, the high temperature area reach 0.2 at about $t = 3000$ ns, which indicates 80% of material particles could not obtain a temperature higher than 700 K up to this time. When $DT = 500$ K, the high temperature area keeps nearly zero during the whole period shown here, which indicates all the local temperature is lower than 800 K up to $t = 3000$ ns. For cases with $DT = 300$, 330, 360 and 400 K, after the initial slow increasing period, the high temperature area shows a quick increasing period. The latter means that a large number of high temperature regimes in the previously compressed region coalesce during this period. After that the increasing rate of A shows a slowing-down phenomenon. The slope of the $A(t)$ curve roughly indicates a mean propagation speed of some components of the compressive waves. When a velocity D of the profile front of high temperature domains is mentioned, the corresponding temperature should also be claimed. It is clear that $D(T_{\rm th})$ decreases when $T_{\rm th}$ becomes higher. The total fractional high temperature area $A(t)$ shows roughly a parabolic behavior during the initial period. When DT approaches 0, the curve for high temperature area $A(t)$ goes back to be quasi-linear.

Now we analyze the second Minkowski measure, the boundary length L. For the case of $DT = 10$ K, after the initial increase period, L keeps a small constant up to about the time $t = 2600$ ns. The phenomenon that boundary length L keeps constant while the high temperature area A increase indicates also that the compressive wave is propagating towards the upper free surface and the interface is nearly a plane. The increasing of L after $t = 2600$ ns is companied by a decreasing of high temperature area A, which indicates some small low temperature spots occur inside the background of high temperature area. The curves for $DT = 100$ K and $DT = 200$ K present similar information. They first increase with time due to the creation of more spots with high temperature, then decreases due to the coalesce of high temperature areas, and finally increase, accompanied by a slight decrease of the total fractional high temperature area. For the case with $DT = 300$ K, during the period with 1500 ns $< t <$ 2500 ns, the high temperature area A increases, while the total fractional boundary length L is nearly a constant. This phenomenon indicates that, during this period, the compressive waves propagate forwards, more scattered high temperature spots appear in the newly compressed regime; at the same time, some previous scattered spots with high temperatures coalesce. From the time 2500 ns to 3000 ns, the fractional high temperature area A increases very slowly, but the boundary length L decreases quickly. This phenomenon indicates that the increasing of A is mainly due to coalesce of previous scattered spots with high temperature. The curves for $DT = 330$ K and $DT = 360$ K can be interpreted in a similar means. For this shock strength, only very few material particles can obtain a temperature higher than 700 K before the time $t = 2000$ ns. Therefore, the boundary length L for $DT = 400$ K has a meaningful increase only after the time $t = 2000$ ns.

When the threshold value DT is small, the condition $T > T_{\rm th}$ is satisfied in (nearly) all of the compressed region and $T < T_{\rm th}$ is satisfied in the uncompressed part of the material. The condensed temperature field appears as a highly connected structure with (nearly) equal and very small amount of high temperature and low temperature domains. So, the Euler characteristic χ keeps nearly zero in the whole shock-loading process and the mean curvature κ is also nearly zero. The value of χ decreases to be evidently less than zero in the unloading process, which means that the number of low temperature domains increases. (See the $\chi(t)$ curves for cases of $DT = 10$, $DT = 100$ and $DT = 200$ in Figure 32.) With increasing the threshold value $T_{\rm th}$, more domains changes from high temperature to low temperature ones. The pattern evolution in the shock-loading process shows the following scenario: scattered high temperature domains appear gradually with time in the background of low temperature domains. Consequently, the Euler characteristic χ is positive and increasing with time. (See the $\chi(t)$ curves for cases of $DT = 300$, $DT = 330$ and $DT = 360$ in Figure 32.) When the threshold value $T_{\rm th}$ is further increased up to 700 K, a considerable fraction of material particles could not obtain a temperature higher than $T_{\rm th}$. The saturation phenomenon in the χ curve during the period, 550 ns $< t <$ 2100 ns, indicates that the numbers of connected domains with high and low temperatures vary with time in a similar way. The increase of χ in the period, 2100 ns $< t <$ 2500 ns, is due to that the rarefactive waves make mean-temperature decrease, some connected high temperature domains are disconnected again. For the case with $DT = 500$ K, the so-called low temperature domain occupies nearly all the shocked material. Consequently, χ is nearly zero.

Effects of porosity To study the effects of porosity, a set of snapshots for the case with a lower porosity are shown in Figure 33. Here $\Delta = 0.286$ and the other conditions are the same as those in Figure 31. From left to right, the corresponding times are $t = 500$, 1100, 1400 and 1700 ns, respectively. It is easy to find that the propagation velocity of compressive wave increases with decreasing the porosity. In this case, at time $t = 500$ ns, the compressive wave arrives at the position with $y = 1750$ μm; while in the case of $\Delta = 0.5$, the compressive wave arrives only at the position with $y = 1000$ μm. In this case, the compressive wave has arrived the top free surface and the rarefactive wave has been reflected back to the porous material before $t = 1400$ ns; while in the case of $\Delta = 0.5$, the shock-loading procedure has not been finished up to the time $t = 1500$ ns.

The porosity effects can be more quantitatively investigated via the morphological analysis. In Figure 34 we show a set of morphological analysis for the cases with various porosities, $\Delta = 0.592, 0.5, 0.412, 0.286, 0.180,\ 0.130,\ 0.091$

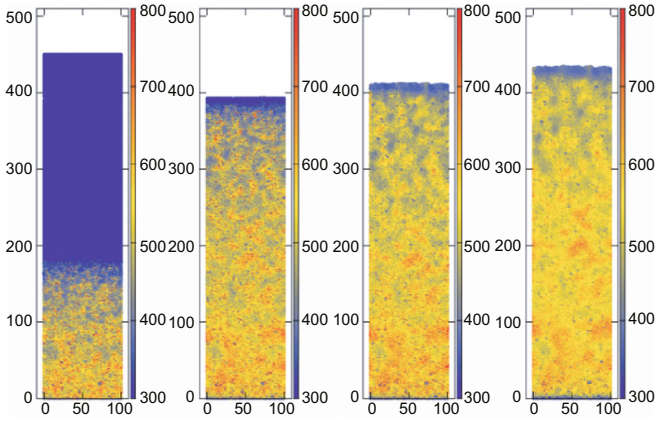

Figure 33 (Color online) Configurations with temperature contours. $\Delta = 0.286$ and $v_{\rm init} = 1000$ m/s. From left to right, t=500, 1100, 1400, and 1700 ns, respectively. The length unit here is 10 μm. (Adopted with permission from ref. [48].)

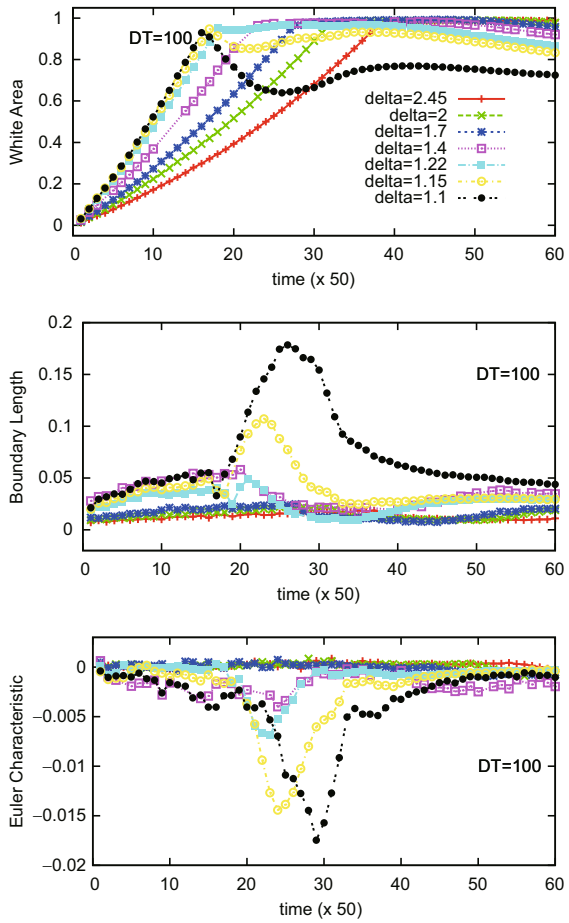

Figure 34 (Color online) Minkowski measures for cases with various porosities. $T_{\rm th} = 400$ K. The values of δ are shown in the legend. (Adopted with permission from ref. [48].)

(i.e. $\delta = 2.45$, 2, 1.7, 1.4, 1.22, 1.15, 1.1), where $T_{\rm th} = 400$ K. Via comparing the slopes of the $A(t)$ curves for the shock loading processes, it is clear that the velocity D of the profile front of high temperature domains decreases with increasing porosity. The largest value of boundary length $L_{\rm max}$ increases as Δ decreases. In the case of $\Delta = 0.091$, the L obtains its maximum value at about the time $t = 1250$ ns. This phenomenon indicates that the highest temperature in shocked porous material decreases when the porosity decreases. The value of χ becomes more negative when Δ decreases from 0.592 to 0.091, which means the disconnected low temperature domains where $T < 400$ K dominate more the condensed temperature field.

Via comparing results in Figures 35 and 36, we can have some observation on the result dependence on the temperature threshold $T_{\rm th}$. Figures 35 and 36 show, respectively, two sets of the Minkowski measures for the same porosities but two higher temperature thresholds, $T_{\rm th} = 500$ K and $T_{\rm th} = 600$ K. They present some supplementary information to that shown in Figure 34. For cases with $\Delta = 0.286$, 0.180, 0.130 and 0.091, only 88%, 55%, 36% and 15% of the material particles obtain a temperature higher than 500 K. For cases with $\Delta = 0.286$ and 0.180, and only 16% and 6% obtain a temperature higher than 600 K in the shock-loading process. When the temperature threshold $T_{\rm th} = 500$ K, the

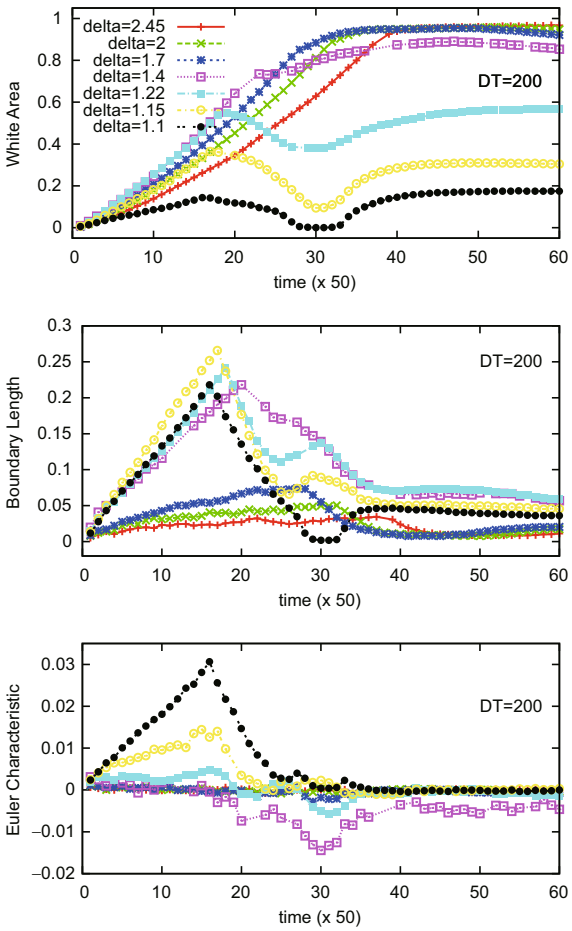

Figure 35 (Color online) Minkowski measures for cases with various porosities. $T_{\rm th} = 500$ K. The values of δ are shown in the legend. (Adopted with permission from ref. [48].)

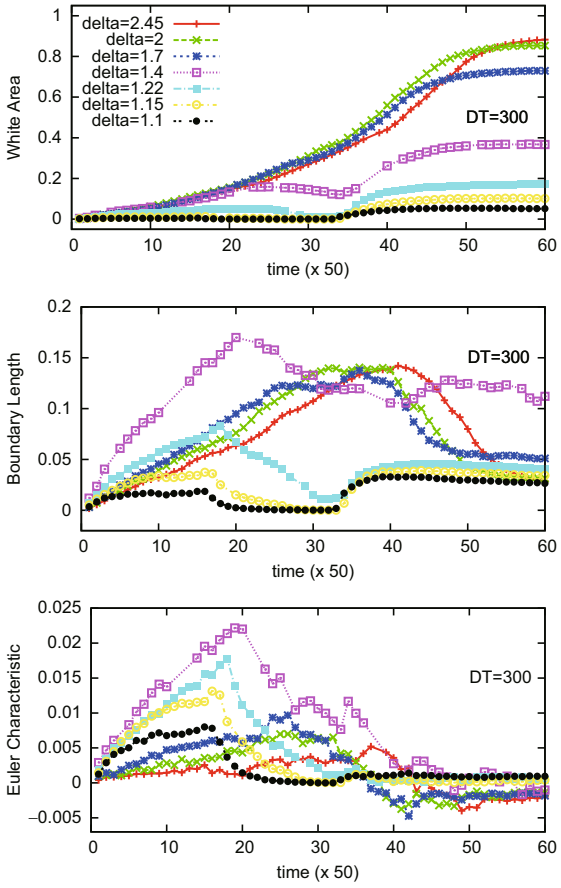

Figure 36 (Color online) Minkowski measures for cases with various porosities. $T_{\rm th}$ = 600 K. The values of δ are shown in the legend. (Adopted with permission from ref. [48].)

case of Δ = 0.130 shows the maximum boundary length and the case of Δ = 0.091 shows the maximum Euler characteristic. When the temperature threshold $T_{\rm th}$ = 600 K, the case of Δ = 0.286 shows the maximum boundary length and maximum Euler characteristic, which means the high temperature spots with T > 600 K are scatteredly distributed in the background of low temperature regime with T < 600 K.

Effects of shock strength When study the effects of shock strength, we fix the value of porosity. A set of snapshots for the case with Δ = 0.286 and $v_{\rm init}$ = 500 m/s are shown in Figure 37. From left to right, the corresponding times are t = 500, 1500, 2000 and 2500 ns, respectively. The first two are for the shock loading process and the latter two are for the shock unloading process. Compared with the case shown in Figure 33, the velocity D of profile front of high temperature domains and the highest temperature $T_{\rm max}$ decreased. The Minkowski meansures for the temperature field in this process is shown in Figure 38. Such a shocking process could not result in high temperature domains with T = 500 K. High-temperature area continue to increase even after some precursory compressive waves have scanned all the material and some rarefactive waves have come back from the upper free surface. Up to the time t = 3000 ns, the fractional high temperature area of with T > 400 K reaches 40%, the fractional area for T > 380 K reaches 74%, that for T > 360 K reaches 91%. The temperature threshold value with T = 380 K shows the largest boundary length at about the time t = 1500 ns when the high temperature spots

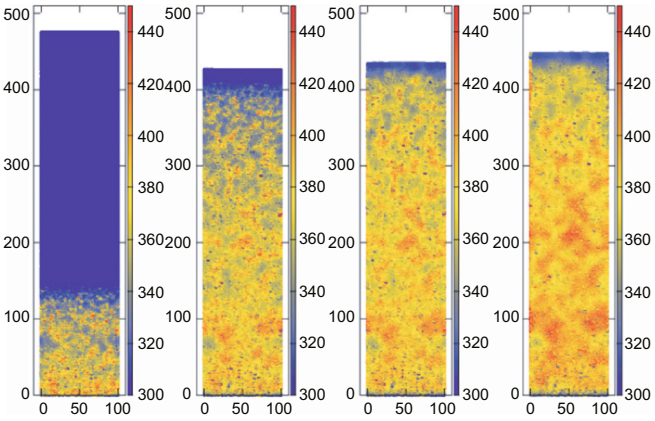

Figure 37 (Color online) Configurations with temperature contours. Δ = 0.286 and $v_{\rm init}$ = 500 m/s. From left to right, t = 500, 1500, 2000, and 2500 ns, respectively. The length unit here is 10 μm. (Adopted with permission from ref. [48].)

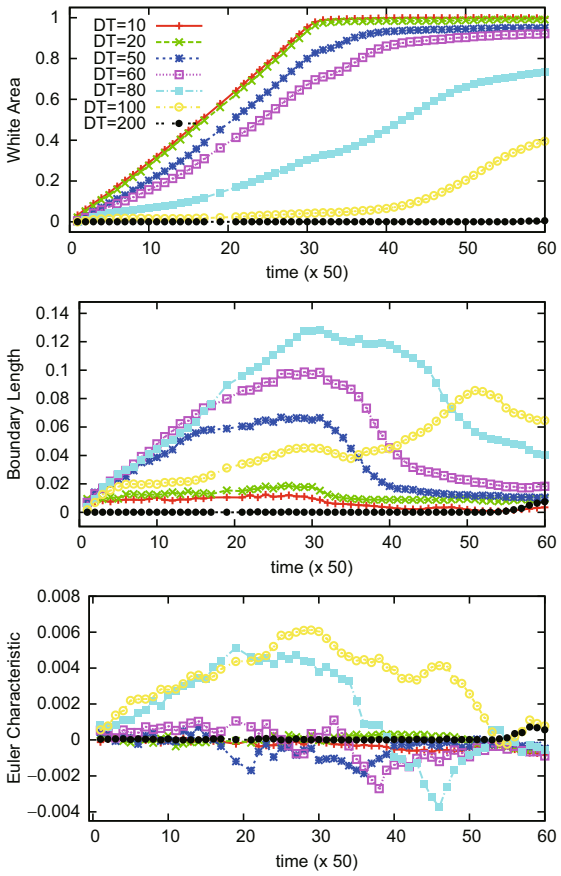

Figure 38 (Color online) Minkowski measures for the case of Δ = 0.286 and $v_{\rm init}$ = 500 m/s. The values of contour level are shown in the legend. (Adopted with permission from ref. [48].)

mainly distribute scatteredly in the low temperature background. Figures 39 and 40 show the morphological analysis for cases with the same porosity but lower initial shocking strengths. Figure 39 is for the case with $v_{\rm init}$ = 400 m/s. Figure 40 is for the case with $v_{\rm init}$ = 300 m/s. With the decrease of initial shock strength, the highest temperature $T_{\rm max}$ in the system becomes lower; the total fractional high temperature area A for low threshold value, for example DT = 10 K, increases with time in a more linear way.

The comparison of Minkowski measures for cases with different initial shocking strengths is shown in Figure 41, where Δ = 0.286, DT = 50 K, $v_{\rm init}$ = 1000, 500, 400, 300, and 200 m/s. The higher the initial shock strength, the larger the slope of $A(t)$ curve. The case with $v_{\rm init}$ = 400 m/s shows the largest boundary length. For this case, scattered high temperature spots dominate the condensed temperature field in the shock-loading process, while scattered low temperature spots dominate in the unloading process.

Dynamic similarities We present some results on dynamic similarities occurred in shocked porous material [66]. Figure 42 shows a set of morphological analysis for the case with Δ = 0.09 and $v_{\rm init}$ = 800 m/s in the three-dimensional

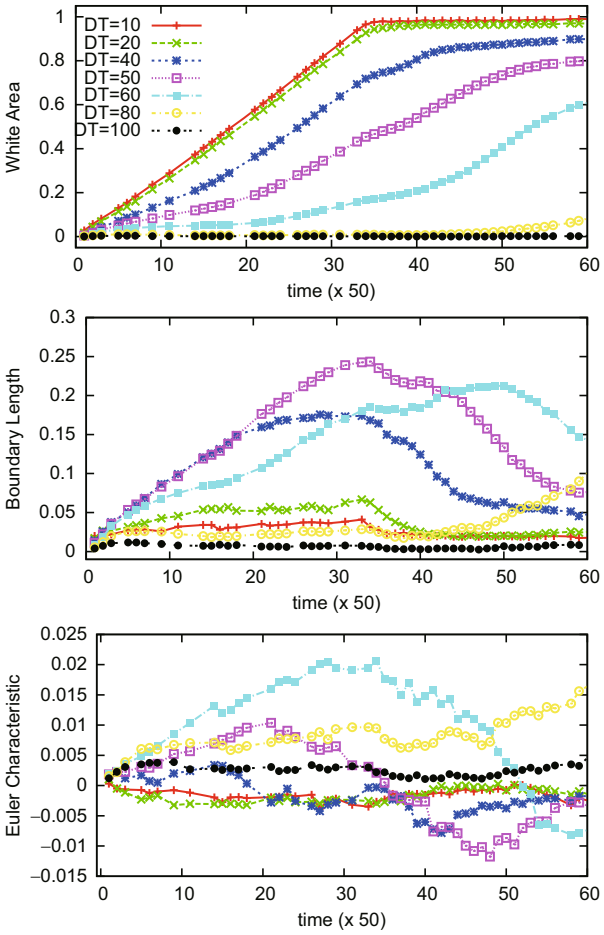

Figure 39 (Color online) Minkowski measures for the case of Δ = 0.286 and $v_{\rm init}$ = 400 m/s. The values of contour level are shown in the legend. (Adopted with permission from ref. [48].)

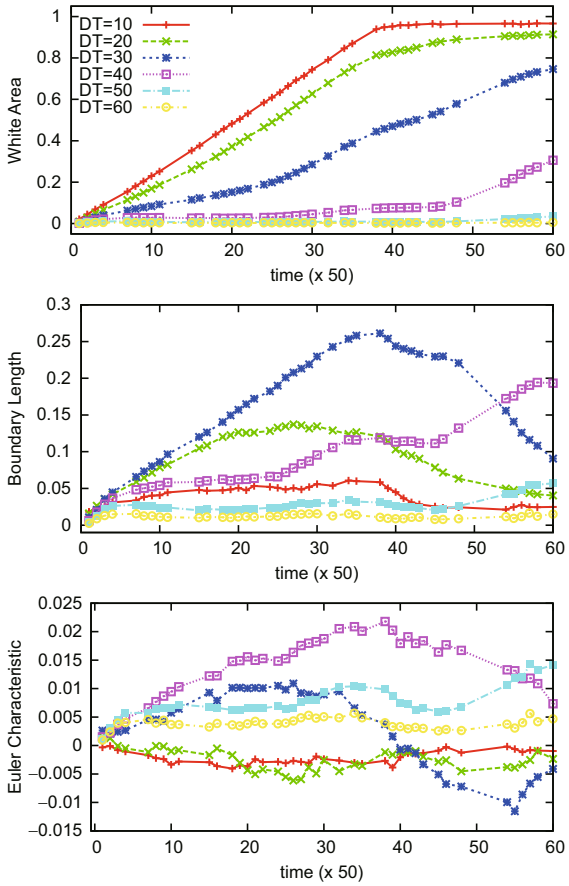

Figure 40 (Color online) Minkowski measures for the case of Δ = 0.286 and $v_{\rm init}$ = 300 m/s. The values of contour level are shown in the legend. (Adopted with permission from ref. [48].)

space opened by the three Minkowski functions. That the curves for DT = 5, 30 and 60 K are closer indicates that the shape and connectivity of high temperature domains for these cases show high similarities. We can check in which cases the condensed temperature fields show similarities. Such information is generally helpful for classifying the shocking dynamic processes, material selection and structured material design. For fixed material components and structures, an evolution process for a condensed temperature field is determined by the initial shock strength. We can label an evolution process of a condensed temperature field by a pair of quantities, ($v_{\rm init}$, $T_{\rm th}$). We further add a subscripts, "1" or "2", to index the evolution process. For cases with fixed porosity, Δ = 0.09, we first choose an evolution process with $v_{\rm init1}$ = 800 m/s and $T_{\rm th1}$ =408 K, as the reference, check its process distance d_P to the evolution process with $v_{\rm init2}$ = 900 m/s and $T_{\rm th2}$. It is easy to find that the distance d_P takes its minimum value when $T_{\rm th2}$ = 442 K. In the same means, we can know that the following evolution processes, "300 m/s, 315 K", "400 m/s, 326 K", "500 m/s, 340 K", "600 m/s, 358 K", "700 m/s, 381 K", "1000 m/s, 489 K", show also high similarities to the reference process. If use the eight pairs of $v_{\rm init}$ and $T_{\rm th}$ to plot a curve, then we obtain the one labeled by

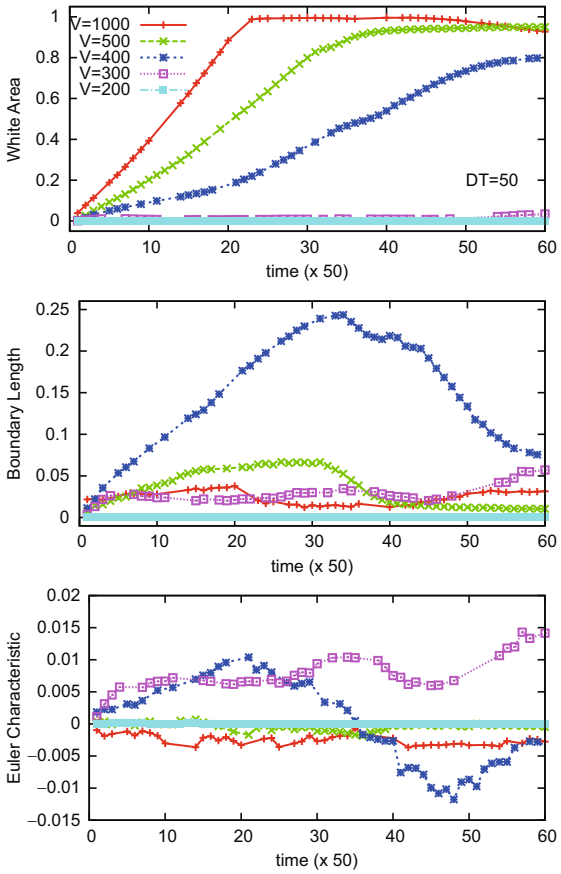

Figure 41 (Color online) Minkowski measures for cases with various shock strengths. $\Delta = 0.286$. The values of initial impacting speed $v_{\rm init}$ are shown in the legend. (Adopted with permission from ref. [48].)

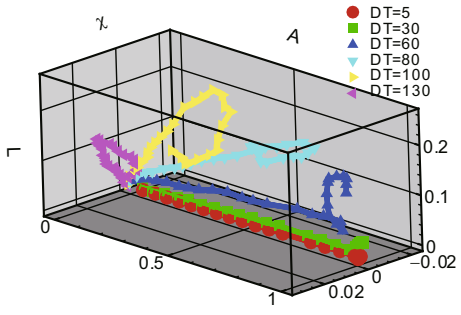

Figure 42 (Color online) Minkowski description in the three-dimensional space opened by A, L and χ.

"300:15" in Figure 43(c). The label "300:15" means processes shown in this curve show high similarities to the case where $v_{\rm init1} = 300$ m/s and $DT = 15$ K. If increases the temperature threshold of the reference process, we can obtain, in the same means, other curves shown in the figure. Figures 43(a), (b) and (d) are for the cases with $\Delta = 0.03$, $\Delta = 0.18$, $\Delta = 0.286$, respectively. From Figure 43 one can also find that, when the porosity is high, the value of $\sqrt{T_{\rm th} - 300}$ shows nearly linear dependence on the impact velocity $v_{\rm init}$. However, when the porosity is very small, the

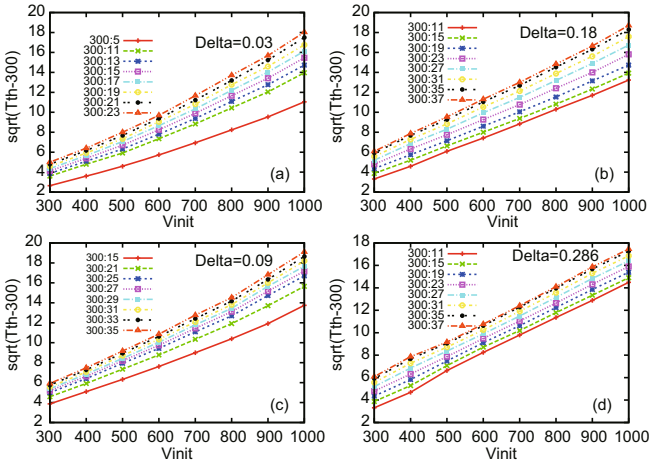

Figure 43 (Color online) $\sqrt{T_{\rm th} - 300}$ versus $v_{\rm init}$ for similar processes. From (a) to (d), the porosity is 0.03, 0.18, 0.09, 0.286, respectively.

increasing rate of $\sqrt{T_{\rm th} - 300}$ with respect to $v_{\rm init}$ is larger. The physical reasons are as below. The temperature increasing is mainly due to the plastic work when the porosity is high, while it is mainly from the shock compression when the porosity is very small [66].

The shock strength, described by $v_{\rm init}$, is fixed when we study the dynamical similarity S_P versus porosity Δ. In such cases, an evolution process can be labeled by the pair of values, $(\Delta, T_{\rm th})$. We first consider the cases with $\Delta_1 = 0.09$ and $\Delta_2 = 0.01$. The initial impact velocity is fixed at $v_{\rm init} = 800$ m/s. Processes with $T_{\rm th1} = 315, 320, 360, 390, \cdots, 630$ K, show high similarities to the processes with $T_{\rm th2} = 346, 347, 350, 353, \cdots, 481$ K, respectively. If use the values of $(T_{\rm th1} - 300)$ for $\Delta_1 = 0.09$ as the x-coordinates and $(T_{\rm th2} - 300)$ for $\Delta_2 = 0.01$ as the y-coordinates, we obtain the curve labeled by "0.01" in Figure 44. Figure 44 shows also the cases with $\Delta_2 = 0.02, 0.029, 0.048, 0.09, 0.13, 0.329$. An interesting results is that all curves meet at a point which corresponds to the temperature increment of uniform material under the same shock strength.

We can get more observation along this line. Under the same shock strength, the processes with ($\Delta_2 = 0.01$, $T_{\rm th2} - 300 = 144$ K), ($\Delta_2 = 0.02$, $T_{\rm th2} - 300 = 173$ K), ($\Delta_2 = 0.029$, $T_{\rm th2} - 300 = 195$ K), $\cdots$, ($\Delta_2 = 0.329$, $T_{\rm th2} - 300 = 336$ K) show high similarities to the process with ($\Delta_1 = 0.09$, $T_{\rm th1} - 300 = 270$ K). If the relations between $(T_{\rm th} - 300)$ and Δ are shown in the log-log scale, we obtain the one labeled by "270" in Figure 45. It is interesting to find that the relation between $(T_{\rm th} - 300)$ and Δ follows a power-law relationship for a wide range. There is a critical value for the porosity beyond which the power-law relation breaks. Figure 45 shows also the cases with $DT = 240, 210, 180, 150$ and 120 K.

In brief, the condensed temperature fields in shocked porous materials may show high similarities when the shock strength, porosity and temperature threshold are appropriately chosen.

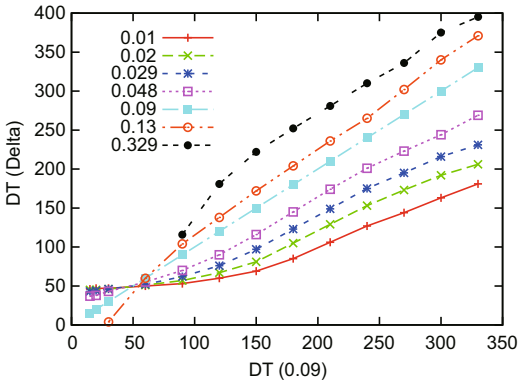

Figure 44 (Color online) $DT(\Delta_1)$ versus $DT(\Delta)$ for similar dynamical processes. The horizontal axis shows the temperature threshold in the reference material, $DT(\Delta_1 = 0.09)$. The vertical axis shows the corresponding DT values in the second material. The porosities of the second material, 0.01, 0.02, 0.029, 0.048, 0.09, 0.13, and 0.329, are shown in the legend.

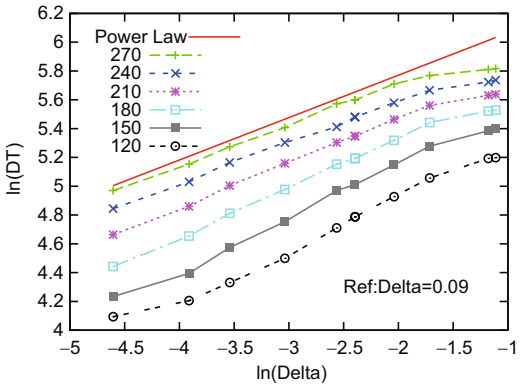

Figure 45 (Color online) Temperature threshold versus the porosity for similar dynamical processes. The porosity of the reference material is 0.09, the values of $T_{\rm th}$ − 300, 270, 240, 210, 180, 150 and 120, are shown in the legend. The plot is in log-log scale. A straight line is shown to guide the eyes.

4.2 MPM investigations: Local behaviors

In our MPM simulations, local behaviors are referred to the dynamical behaviors occurred around a single cavity in the material under shock loading or unloading process.

4.2.1 Shock loading

We set a single cavity in the simulated material. Due to the periodic boundary conditions applied in the horizontal conditions, what we considered corresponds to a very wide system with a row of cavities in it. We study various cases where the shock strength varies from strong to weak. In the cases with strong shock, the jet creation and the distribution of the "hot spots" are the main concern. When the cavity is close to the free surface, the critical condition for observing jetted material particles from the upper free surface is studied. In the cases with weak shock, we investigate the effects of cavity size, distance from the cavity center to the impacting interface, the initial yield stress of the material, etc, on the collapsing process [24].

The main studies here include two parts: (i) the dependence of collapsing symmetry on the shock strength and other interfaces, (ii) hydrodynamic and thermodynamic behaviors ignored by the pure fluid models. In the case with weak shock, an interesting observation is that the cavity may not be collapsed completely and the cavity may collapse in a nearly isotropic means. In the case with strong shock, the jetting process is carefully studied. The specific collapsing process significantly affects the distribution of "hot spots" in the shocked material.

A snapshot for a case with high shock strength is shown in Figure 46. The initial pressure loaded by the shock is about 30 GPa which is less than the critical value, 270 GPa. The global scenario is follows: (i) When the shock wave arrives at the upper-stream wall of the cavity, plastic deformation begins to occur. The shock waves at the two sides of the cavity propagate forwards to the free surface. The propagation speed of compressive waves at the two sides is larger than the deforming speed of the upper-stream wall of the cavity. (ii) The cavity continues to collapse, a configuration with a turned "C" occurs. A jet phenomenon occurs. "Hot spots" occurs at the tip regime of the jet (See Figure 46(a)). (iii) The propagation speed of jetted material increases with time. Along the initial shocking direction, the tip of the jet catches up, then exceeds the compressive waves at its two sides. (iv) The jetted material particles hit the down-stream wall of the cavity, leads to a pair of vortices rolling in opposite directions. The "hot spots" appear at the vortex centers (See Figure 46 (b)).

When the cavity is close to the upper free surface, if the shocking is strong enough, the material particles jetted into the cavity will break the down-stream wall of the cavity, and consequently, some material particles will be jetted out of the upper free surface. Such a behavior has been observed in experiments and has long been concerned. A dynamical process is shown in Figure 47, where the initial cavity is under the free surface by a distance $d = 4.5$ μm and the initial radius is $r = 1.5$ μm, $v_{\rm init} = 1120$ m/s. The corresponding times for

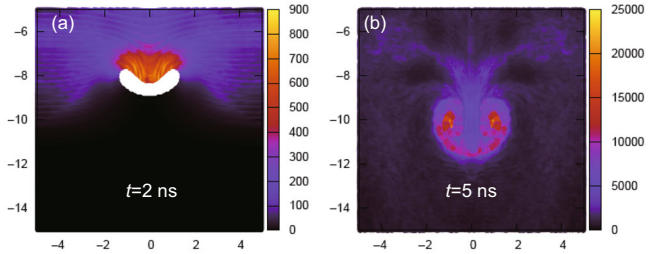

Figure 46 (Color online) Snapshots of collapse of a single cavity under strong shocks, where $v_{\rm init} = 1500$ m/s. From black to yellow the grey-level in the figure shows the increase of local temperature denoted by the plastic work during the deformation procedure. The spatial unit is μm. The unit of work is mJ. (a) t=2 ns; (b) t=5 ns. (The gray-level version is published in ref. [24].)

Figures 47(a)-(f) are 1.2, 1.6, 1.8, 2.0, 2.2, and 12.0 ns, respectively. Figure 47(a) shows a snapshot where the shock wave has passed most part of the cavity. At this time the cavity has been substantially deformed and some material particles have been projected into the cavity. When t = 1.6 ns, the cavity has been nearly filled with the jetted material (See Figure 47(b)). The compressive wave first arrives at the upper free surface and rarefactive waves are reflected back from the two sides. The rarefactive waves reflected back into the shocked material decrease the pressure and new cavitation may occur around the region of the original cavity (See Figures 47(c) and (d).) Compared with those at the two sides, material in the middle has a much higher pressure and has much more kinetic energy. The newly created cavities coalescence and become a larger one with time (See Figure 47(e)). If the upper wall of the newly created cavity possesses enough kinetic energy, it will break (See Figure 47(f)). The corresponding configurations with temperature is shown in Figure 48. In Figure 48(a) the "hot spot" appears at the tip of the material tongue. In Figures 48(b) and (c) the "hot spot" occurs at regime hit by the material tongue. When new cavities are created, "hot spots" occur at the inner wall of the cavity, especially the upper and bottom walls (See Figures 48(d)-(f)). Whether or not there are material particles jetted

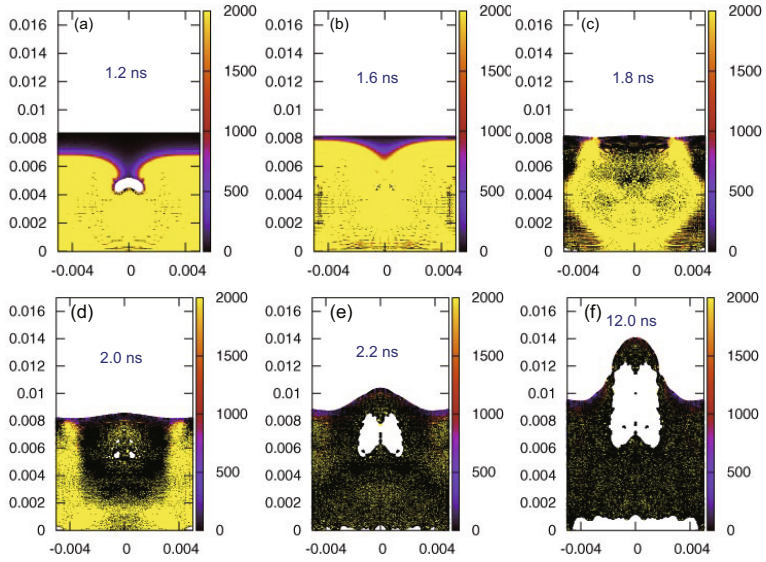

Figure 47 (Color online) Snapshots of collapse of a single cavity under a strong shock. For the pressure contour, from black to yellow the value increases. The corresponding times at (a)-(f) are 1.2, 1.6, 1.8, 2.0, 2.2, 12 ns, respectively. The spatial unit is mm. The unit of pressure is MPa. (The gray-level version is published in ref. [24].)

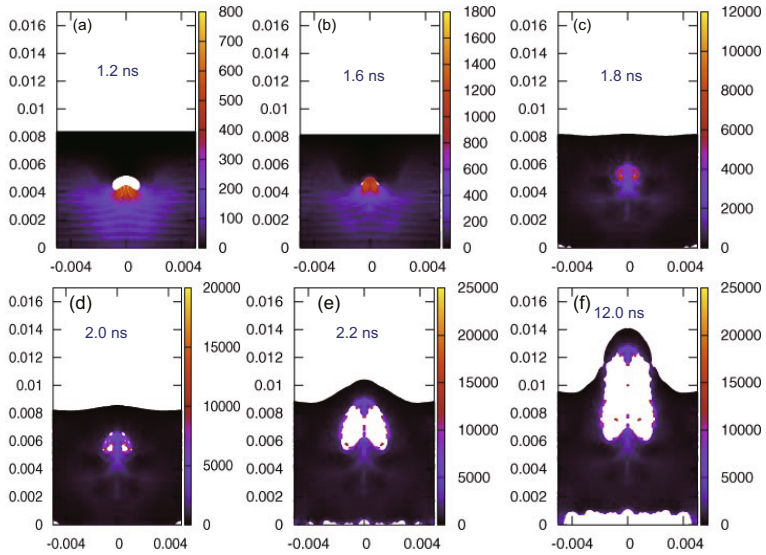

Figure 48 (Color online) Configurations with local temperature denoted by the plastic work during the deformation. The unit of work is mJ. (a)-(f) here correspond to (a)-(f) in Figure 2, respectively. (The gray-level version is published in ref. [24].)

from the upper free surface depends on the initial shocking strength and the width d. The critical initial velocity u increases parabolically with d (See Figure 49).

With decreasing the shock strength, the collapsing process becomes slower. When the initial impact velocity decreases to about 200 m/s, the dynamical scenario has been significantly different. It is interesting to find that the cavity can not be fully collapsed, and the final configuration around the cavity varies from (nearly) symmetric to asymmetric, or vice verse, with changing the distance from the cavity center to the impacting surface. Figure 50 shows an asymmetric dynamical scenario where the cavity collapsed less in shocking direction. The behavior can be understood via "recovering" or "magnifying" the system in such a way: The rigid walls at the two sides and at the bottom of the system can be regarded as "mirrors". The extended system is symmetric about the "mirrors". The distance between two neighboring cavities in the horizontal direction is d_H; and the distance between the two cavities in the computed and the fictitious material bodies, respectively, is d_V. The cavities reflect rarefactive waves when compressive waves come, which makes lower the pressure in between two cavities. If the distance d_V in vertical direction is much less than d_H in horizontal direction, the rarefaction effects in between the two cavities in vertical direction are more pronounced. Therefore, the pressure in this region is lower than those in the surrounding regions. At the same time, when the compressive waves arrive at the upper free surface, rarefactive waves will be reflected back and propagate towards the cavity. This is a second reason why the cavity collapses less in the vertical direction. Compared with the rarefactive waves reflected from the fictitious cavity below the bottom, the ones from the upper free surface make effects in a much wider range, which is responsible for the phenomenon that the collapsing of the lower part of the cavity is more pronounced. Figure 51 shows such an case. The highest temperature appears in the region below the cavity. Figures 50(a) and 51(a) show that, although the rarefactive waves lower the pressure in the influenced region, but may increase the temperature. Because the rarefactive waves may make plastic work.

The temperature in the "hot spot" continues to increase in the process of collapsing. The lower part of the cavity will collapse more pronouncedly if the distance between the cavity and the lower impacting face is further decreased. Figure 52(a) shows the final steady state for such a case, where the lower boundary of the cavity just locates at the impacting face. In contrast, if the distance between the cavity and the lower impacting face is increased, the collapsed cavity will be more symmetric. Figure 52(b) shows such a case, where the collapsing is nearly isotropic.

When study the effects of cavity size on the collapsing behaviors, the other conditions are kept unchanged. For the checked cases, the collapsibility increases with decreasing the initial cavity. The evolution of area of the cavity is shown in Figure 53(a), where four different sizes are used. If define the collapsibility as $\Phi = (A_0 - A)/A_0$, then Φ decreases with increasing the cavity radius, where A_0 and A are the areas of the cavity in the initial and final states (See Figure 53(b)). The effects of material strength is also investigated via changing the initial yield stress of the material and keeping unchanged all other parameters. The corresponding collapsing processes

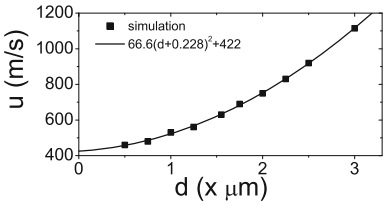

Figure 49 Critical impact velocity versus the thickness of the downstream wall of the cavity. The symbols are simulation results and the solid line is the fitting result. (Adopted with permission from ref. [24].)

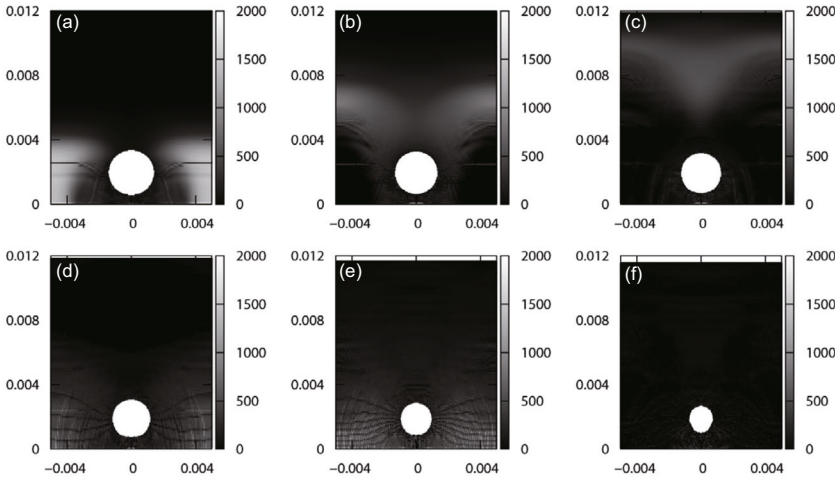

Figure 50 Snapshots of collapse of a single cavity under a weak shock. From black to white the local pressure increases. The spatial unit is millimetre. The unit of pressure is megapascal. (a) t=1.0 ns; (b) t=1.6 ns; (c) t=2.2 ns; (d) t=3.0 ns; (e) t=5.4 ns; (f) t=16.0 ns. (Adopted with permission from ref. [24].)

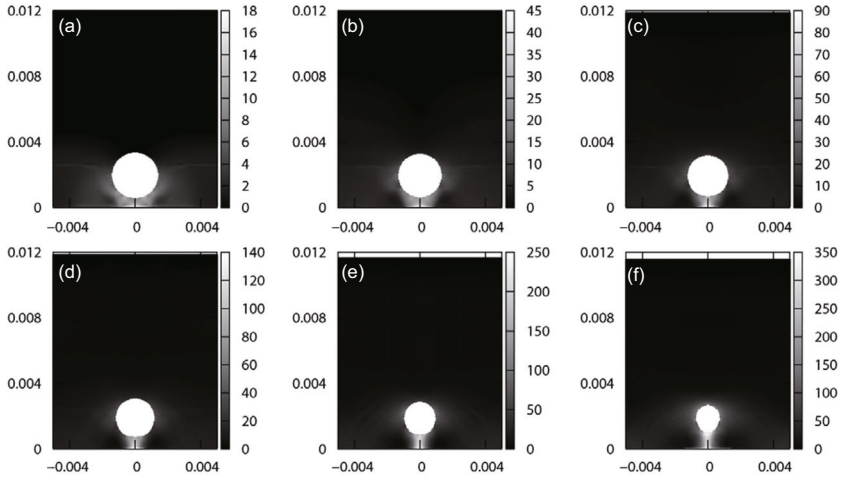

Figure 51 Configurations with local temperature denoted by the plastic work during the deformation. From black to white the grey level in the figure shows the increase of local temperature. The spatial unit is millimetre. The unit of work is millijoule. (a) t = 1.0 ns; (b) t = 1.6 ns; (c) t = 2.2 ns; (d) t = 3.0 ns; (e) t = 5.4 ns; (f) t = 16.0 ns. (Adopted with permission from ref. [24].)

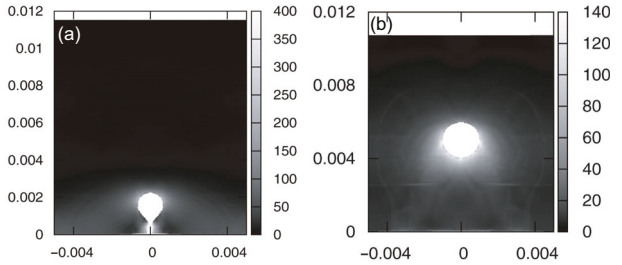

Figure 52 Transition of symmetry of collapsing. (a) Asymmetric in vertical direction near the impacting face; (b) nearly symmetric collapse. The gray level in the figure corresponds to the plastic work. The spatial unit in the figure is millimetre. The unit of energy is millijoule. (Adopted with permission from ref. [24].)

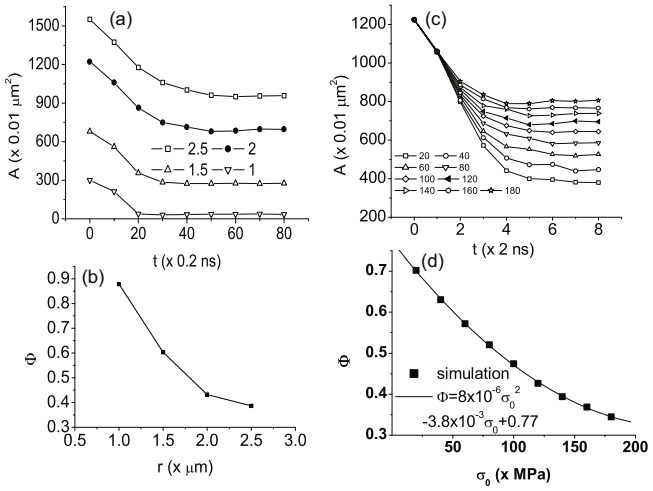

Figure 53 Effects of cavity size ((a) and (b)) and initial yield ((c) and (d)) to the collapsing procedure. (a) Area of cavity versus time for different initial radius. What shown in the legend are the initial radii, the unit is μm; (b) collapsibility versus initial radius of cavity; (c) area of cavity versus time for different initial yield stresses. What shown in the legend are the initial yield stresses, the unit is megapascal; (d) collapsibility versus initial yield stress. (Adopted with permission from ref. [24].)

are shown in Figure 53(c). The collapsibility decreases nearly parabolically with increasing the initial yield (See Figure 53(d)).

4.2.2 Shock unloading

Response and failure of ductile materials under dynamic loading are important and fundamental issues in the fields of science and engineering. The process of material failure is very complicated because various physical and mechanical mechanisms, in a wide spatial-temporal scales, are involved and coupled. The spallation and fragmentation of metal materials consist mainly of the following typical stages: nucleation, growth and coalescence of microscopic voids and/or larger scale cavities. The quasi-static growths of voids and cavities have been extensively studied. However, the dynamical growth is much more complex and far from being well understood.

Early in 1972 Carroll and Holt [69] showed that the compression effect on the cavity growth is not pronounced if the material is not sensitive to the loading rate. The study was extended to the case of visco-plastic materials by Johnson [70] in 1981. In 1987 Becker [71] numerically analyzed the influences of a nonuniform distribution of porosity on the flow localization and failure in a porous material. In this study, the void distribution and properties were obtained from measurements on partially consolidated and sintered iron powder. An elastic visco-plastic constitutive relation for porous plastic solids was used. The model considers local material failure via considering the dependence of flow potential on void volume fraction. The region modeled is a small portion of a larger body under various stress conditions. Under imposed periodic boundary conditions, both the plane strain and axisymmetric deformations were investigated. It was found that interactions between regimes with higher fractions of void promote the plastic flow localization into a band. Local fail-

ure occurs through void growth and coalescence within the band. This study suggested a failure criterion based on a critical void volume fraction. The latter is only weakly dependent on the stress history. The critical void fraction is dependent on the initial void distribution and material hardening characteristics. In 1992 Ortiz and Molinari [72] investigated the influences of strain hardening and rate sensitivity on the dynamic growth of a void in a plastic material. They pointed out that the effects of inertia, hardening and loading rate can significantly influence the void growth. The results of Benson [73] in 1993 and those of Ramesh and Wright [74] in 2003 indicate that the inertia effect is responsible for the stable growth of cavity. In 1998, within the scope of the local approach methodology, Pardoen et al. [75] investigated the ductile fracture of round copper bars. They analyzed two damage models and comparatively studied four coalescence criteria. The two damage models are the Rice-Tracey model and the Gurson-Leblond-Perrin model. The four coalescence criteria are as follows: (i) a critical value of the damage parameter, (ii) the Brown and Embury criterion, (iii) the Thomason criterion and (iv) a criterion based on the reaching of the maximum von Mises equivalent stress in a Gurson type simulation. Both the ellipsoidal void growth and void interaction were accounted for. In this study, as far as possible, all the parameters of the models were identified from experiments and physical observations. Via using specimens which present a wide range of notch radii, the effect of stress triaxiality was studied. Via comparing the behavior of the material in the cold drawn state and in the annealed state, the effect of strain-hardening was analyzed. In 2000 an extended model for void growth and coalescence was proposed by Pardoen et al. [76]. This model integrated two existing contributions. The first is the Gologanu-Leblond-Devaux model extending the Gurson model to void shape effects. The second is the Thomason scheme for the onset of void coalescence. Each of these was extended heuristically to describe the strain hardening. To supplement the criterion for the onset of coalescence, a simple micro-mechanically based constitutive model for the void coalescence stage was proposed. The fully enhanced Gurson model depends on both the flow properties of the material and the dimensional ratios of the void-cell representative volume element. The effect of void shape, relative void spacing, strain hardening, and porosity are incorporated into it. In 2001 an inelastic rate-dependent crystalline constitutive formulation and specialized computational schemes were developed by Orsini et al. [77]. They aim to obtain a detailed understanding of the interrelated physical mechanisms which can result in ductile material failure in rate-dependent porous crystalline materials subjected to finite inelastic deformations. It was shown that ductile failure can occur either due to void growth parallel to the stress axis or void interaction along bands. The former results in void coalescence normal to the stress axis. The latter are characterized by intense shear-strain localization and intersect the free surface at regions of extensive specimen necking. In 2002, two mechanisms of ductile fracture, void by void growth and multiple void interaction, were discussed by Tvergaard and Hutchinson [78]; the plastic flow in porous material was discussed by Zohdi et al. [79].

In most of current studies on cavity/void growth, the main concern is focused on its relevance on macroscopic behaviors [69-79]. The quantitative relations are determined via fitting experimental results. So, those studies were not capable of revealing or indicating the underlying idiographic physical and mechanical mechanisms of cavity/void growth. The cavity coalescence is the final stage of spallation developed from mesoscopic scale to macroscale [80]. But this stage is also the least-known stage [81-88]. Continuous damage mechanic theory adopts fluid or solid model supplemented by some damage modeling. The damage is generally accounted for by an internal variable. The internal variable is generally defined by the variation of some mechanical behavior. It is not dynamically relevant to the particular structures.

Global scenario In our numerical experiments, the simulated aluminum material body is initially located within the volume, $[-20, 20] \times [-20, 20] \times [0, 50]$. The length unit is μm. A spherical cavity with radius $r = 5$ μm is located at the position $(0, 0, z)$ within the material body. A rigid wall with $z = 0$ is connected with the aluminum material body. The mesh size is 1 μm. The diameter of the material particle is 0.5 μm. Periodic boundary conditions are used in the horizontal directions. Free boundary condition is used in the upper surface. The rigid wall is assumed to be the same kind of material with the material body [89]. The material body starts to move upwards at the velocity v_{z0} at the time $t = 0$. Thus, the tensional wave or rarefactive wave occurs at the interface with $z = 0$. The rarefaction wave propagates upwards within the material body.

A set of snapshots of configurations with v_z field are shown in Figure 54, where $z = 10$ μm, $v_{z0} = 100$ m/s. The contours for $v_z = 0$ are shown. The velocities at the nodes within the cavity are equal zero because no material particles are located within the cavity. Before the arrival of the global tensional wave, the upper contour with $v_z = 0$ within the body presents the initial morphology of the cavity. The moving upwards of the lower contour with $v_z = 0$ shows the propagation of tensional wave. The lower contour for $v_z = 0$ is approaching the lower boundary of the cavity at about $t = 0.8$ ns. Before that time the velocities of particles below the cavity had begun to decrease. It can also be found that, below the lower $v_z = 0$ contour, some material particles show negative velocities. With propagating of the tensional wave, the lower contour for $v_z = 0$ begins to get connection with that corresponding to the cavity. When the tensional wave arrives at the cavity, compression wave is reflected back. Under the compression wave, more material particles obtain negative velocities, and their amplitudes continue to increase (See Figures (b) and (c)). Compared with the propagation of tensional wave surrounding the cavity, the cavity deformation is a slower behavior. The surrounding tensional waves begin

to converge after passing the cavity. Thus, higher negative pressure occurs on the top of the cavity. Consequently, material particles on the top of the cavity are accelerated by the upward stresses. At about $t = 3$ ns some material particles obtain velocities larger than 100 m/s (See Figure (d)).

Figure 55(a) shows the configuration with pressure and velocity fields within the $x = 0$ plane, where $t = 2$ ns. Figure 55(c) shows that for $t = 3$ ns. From blue to red, the color cor-

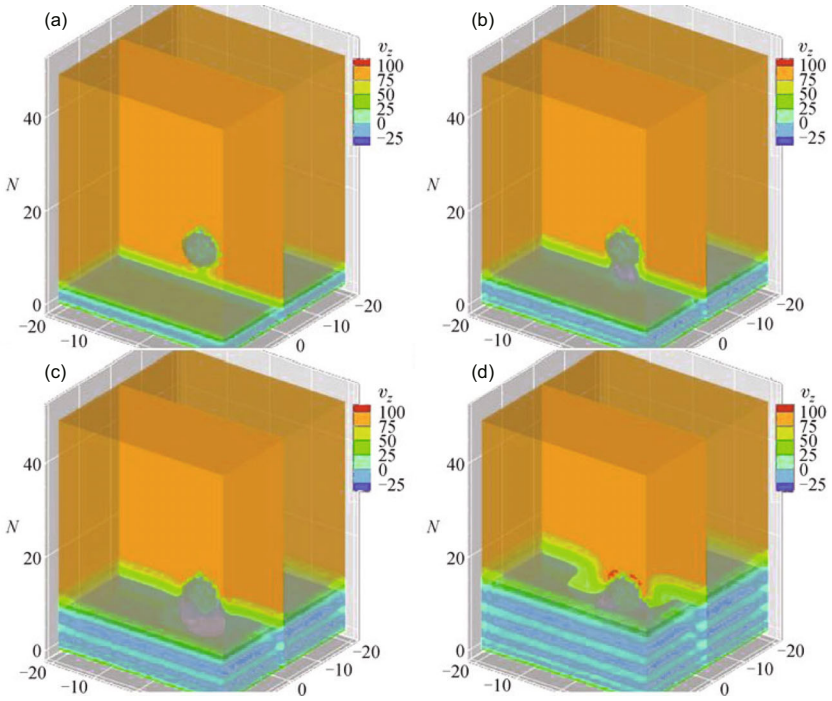

Figure 54 (Color online) Configurations with v_z field at four different times for the case with $z = 10$ μm and initial $v_{z0} = 100$ m/s. The contours for $v_z = 0$ are shown in the plots. (a) $t = 0.8$ ns, (b) $t = 1.2$ ns, (c) $t = 2.0$ ns and (d) $t = 3.0$ ns. (Adopted with permission from ref. [89].)

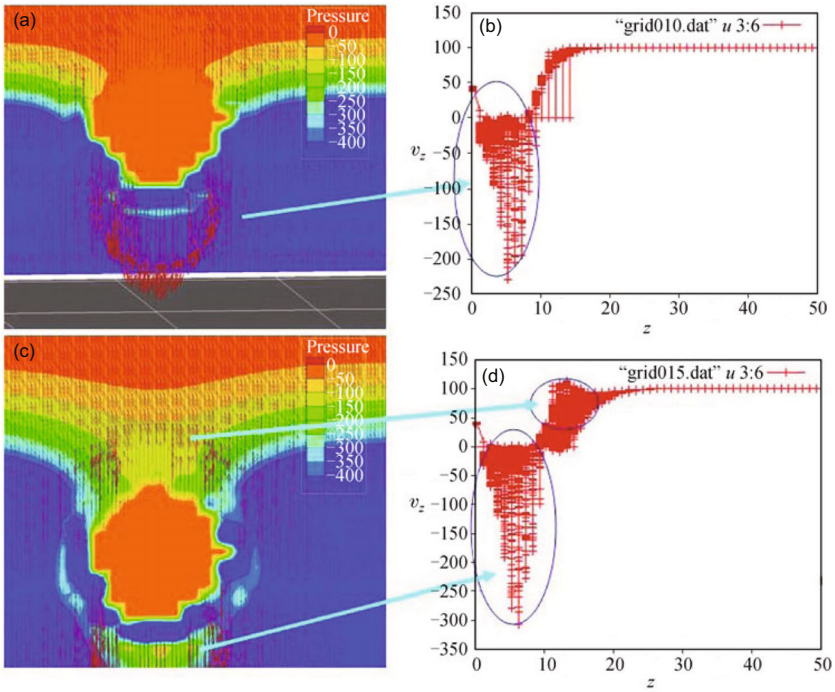

Figure 55 (Color online) Configurations with pressure and velocity fields in the plane with $x = 0$ (see (a) and (c)) and v_z distribution in the tensile direction (see (b) and (d)). $t = 2$ ns in (a) and (c). $t = 3$ ns in (b) and (d). (Adopted with permission from ref. [89].)

responds to the increase of pressure. One can observe the deformation of the cavity under tensile loading. To study the behaviors in amplitudes of particle velocities, the distributions of v_z along the z-direction are shown in Figures 55(b) and (d), respectively. When $t = 2$ ns, the maximum downward particle velocity is about 230 m/s. When $t = 3$ ns, it is about 300 m/s. Figure 55(d) shows also that some material particles have upward velocities larger than 100 m/s. The morphology irregularities of the cavities shown in the figures result from the following three reasons. (i) Due to the discreteness of the material particles in the MPM, the initial cavity is not strictly spherical. (ii) The mesh size is not negligible compared with the dimension of the cavity. (iii) The compressive waves reflected back from the cavity result in the Richtmyer-Meshkov (RM) instability, which is the main physical reason for the initial irregularities of the deformed cavity. For the first two points, it should be pointed out that, in practical simulations, we have to make compromise between the size of simulated material body, cavity size and the mesh unit. It should also be commented that the cavities in practical materials are generally not strictly spherical, which is partly simulated by the finite size effects of mesh and particles.

With the increasing of upward stress acting on particles on the top region of the cavity, the accelerations and velocities of particles increase. The global tensional wave arrives at the upper free surface at bout $t = 7.2$ ns. The maximum value of particle velocities on the top region of the cavity is about 430 m/s. There exists a region below the cavity within which the particles have large downward velocities at this moment. The largest value of downward velocity is about 325 m/s. There exists a valley between the peak and the tensional wave front in the curve of v_z versus z. The smallest value of particle velocities is about 6 m/s. When the tensional wave arrives at the upper free surface, compression wave is reflected back into the material. The material particles, in the region scanned by the reflected compression wave, obtain downward accelerations. Several characteristics are typical for the compression wave. (i) The velocities of material particles, representing the upper free surface, decrease. (ii) The valley continues to move toward the upper free surface. (iii) The maximum velocity between the valley and the cavity continues to increase. At the same time, the region with maximum downward particle velocity moves toward the bottom. The simulation results for the case with single cavity are also indicative for interaction of neighboring cavities because periodic boundary conditions are used in the horizontal directions. From the pressure field, the negative pressures within regions among the neighboring cavities are weaker. The contours for negative pressure with small amplitudes are connected. The compression wave reflected back from the cavity becomes stronger with the increasing of the strength of tensional wave. Consequently, regions with local positive pressures occur among the neighboring cavities. The occurrence of positive pressures within the background regime, where material particles are scanned by the global tensional wave, is a typical cavity effect.

The deformation of the cavity is still controlled by the tensile loading before the reflected compression wave arrives. As an example, we analyze the pressure distributions at two times, 9 and 11 ns. The configurations with pressure field at the time 9 ns is shown in Figure 56, where the contour pressures are −300, −350, −400, −450, −500 and −550 MPa, respectively. Around the cavities, the contours for pressure lower than −300 MPa are connected. The neighboring cavities interact via the connection of pressure contours. There is still no positive pressure occur among the neighboring cavities when $t = 9$ ns. Figure 57 shows various pressure contours, where $t = 11$ ns, and the contour pressures are 0, −50, −100, −150, −200 and −250 MPa, respectively. Observations on pressure distribution around the cavity are as below. (i) The pressure surrounding the cavity is zero. (ii) The corresponding contour moves away from the cavity and its surface area becomes larger with the increasing of pressure. (iii) Among cases shown in the figure, the contour for −150 MPa has the maximum area. The contour area becomes smaller if further increase the pressure value. Observations on pressure distribution between the cavity and rigid wall are as below. There are four regimes, around the cavity, where the pressures are positive. The pressure contours for −100 MPa, between the nearest cavities, are connected. The contours for −150 MPa have a higher connectivity. All contours for −200, −250 MPa, etc. are connected. The pressure distribution on the top of the cavity shows the following behaviors. The highest pressure regime does not locate above the cavity but above the middle of neighboring cavities. Because the tensional wave propagates more quickly within the solid region, the wave firstly arrives at the upper free surface. The weaker the negative pressure, the closer to the upper free surface and the planar the corresponding pressure contour.

Morphology versus tensile strength The configurations with temperature field are shown in Figure 58, where $t = 6$ ns and the contour temperatures are 310, 320, 330 and 340 K, respectively. The thermal process is much slower compared with the dynamical process. It is the plastic work that determines the temperature and distribution of hot-spots.

All tensional waves arrive at the upper free surface at the same time because they propagates in the same speed, sound speed. The growth rate of the cavity gets larger with the increase of tensile strength. The evolution of the cavity morphology is shown in Figure 59. Figure 59(a) is for the cavity volume versus time. The points show simulation results and the lines are plotted to guide the eyes. The initial tensile velocities, 100, 200, 400 and 1000, are shown in the legend, where the unit is m/s. The inset shows an enlarged portion of the curve for $v_{z0} = 100$ m/s. The growth of cavity can be described by the following stages. (i) initial slow growth stage, (ii) linear growth stage, which ends when the global rarefaction wave arrives at the upper free surface, (iii) slower growth stage, which ends when the reflected compression wave arrives at the cavity, (iv) quicker growth stage, and (v) linear

growth stage. The evolutions of the cavity dimensions in Horizontal (H) and Vertical (V) directions are shown in Figure 59(b). The points show simulation results and the lines are plotted to guide the eyes. An interesting phenomenon is that the growth rate in horizontal direction is larger than that in vertical direction. Such a phenomenon corresponds to the "necking effect" in macroscopic scale. The growths of cavity dimensions show also a linear stage. With the increase of the strength of tensile loading, the growth rate becomes larger. The initial linear growth rate of cavity volume versus initial strength of tensile loading v_{z0} is shown in Figure 59(c). The points show the slopes of fitting lines in Figure 59(a) for the first linear growth stage, and the line are linear fitting results for the points. Within the checked range, with increasing the initial tensile velocity v_{z0}, the volume growth rate increases linearly. Figure 60(a) shows the density fields of the material at the time 7.2 ns. Figure 60(b) is for the time, t = 12 ns. The corresponding pressure fields are shown in Figures 60(c) and 60(d).

Energy transformation versus tensile strength During the process of tensile loading, kinetic energy of the material transforms gradually to elastic potential energy and plastic work. For the case with uniform material, those energies distribute uniformly in planes parallel to the rigid wall. The dynamical and thermodynamical process is in fact one-dimensional, even though the material is three-dimensional.

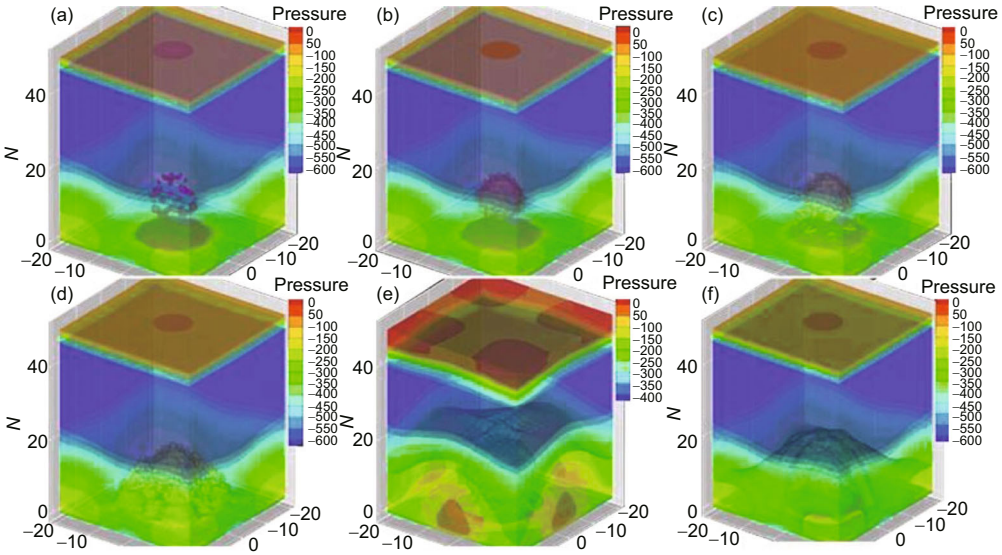

Figure 56 (Color online) Configurations with pressure field at the time 9 ns. The pressure contours in (a)-(f) correspond to −300, −350, −400, −450, −500, and −550 MPa, respectively. (Adopted with permission from ref. [89].)

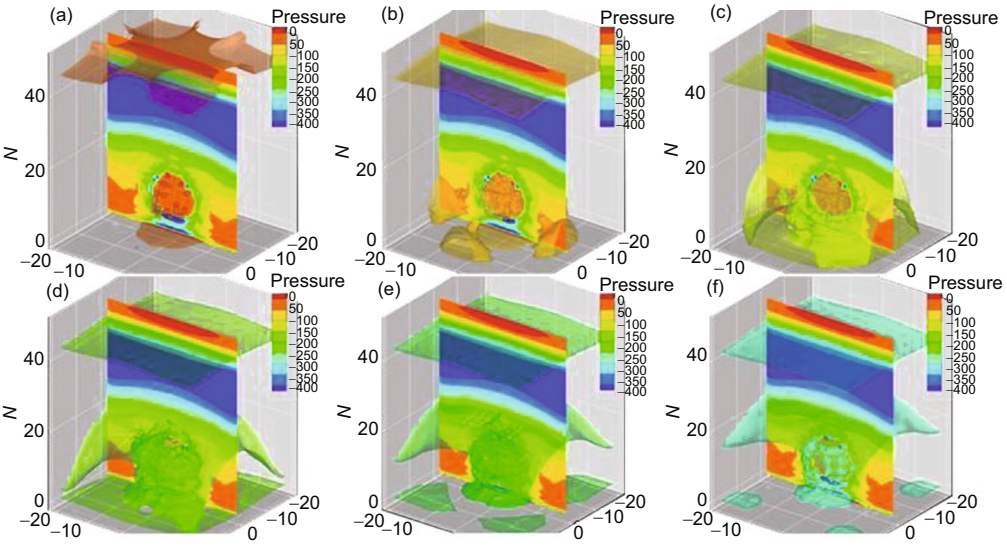

Figure 57 (Color online) Configurations with pressure field at the time 11 ns. The pressure contours in (a)-(f) correspond to 0, −50, −100, −150, −200, and −250 MPa, respectively. (Adopted with permission from ref. [89].)

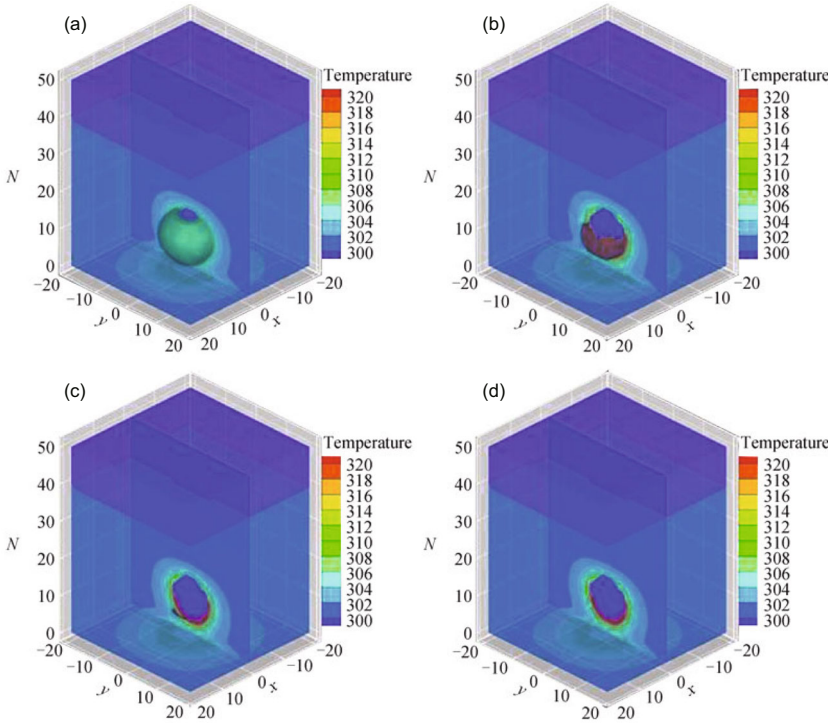

Figure 58 (Color online) Configurations with temperature field at the time 6 ns. The contours in (a)-(d) correspond to 310, 320, 330 and 340 K, respectively. (Adopted with permission from ref. [89].)

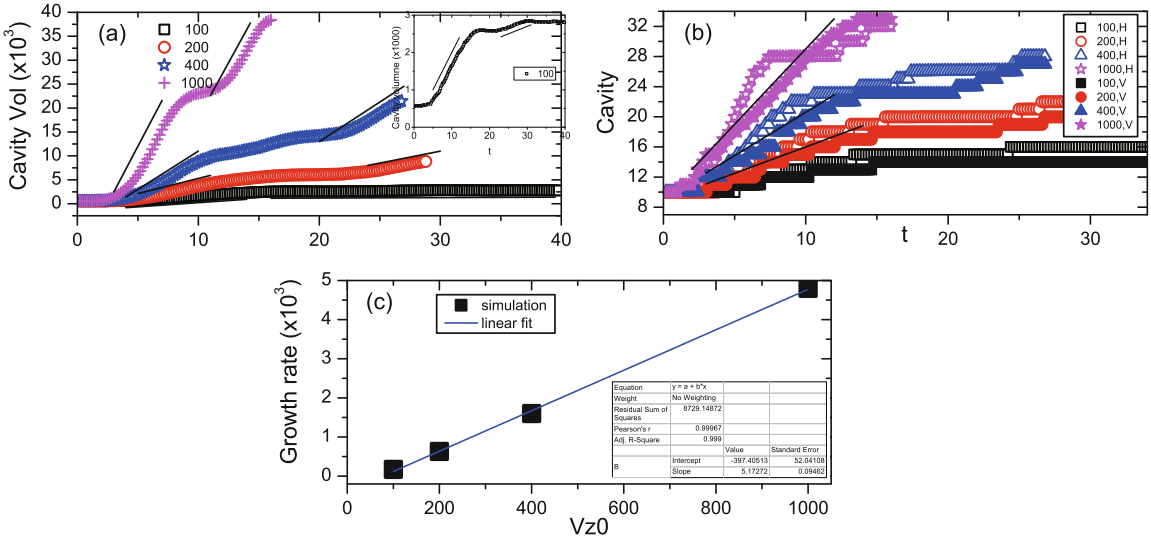

Figure 59 (Color online) Evolution of the cavity morphology. (a) Cavity volume versus time. (b) Cavity dimensions in the Horizontal (H) and Vertical (V) directions versus time. (c) The linear growth rate versus initial tensile velocity. The sizes of the initial tensile velocity v_{z0}, 100, 200, 400 and 1000, are shown in the legend of Figure (a). The unit is m/s. In Figures (a) and (b) the points are simulation results and the lines are plotted to guide the eyes. An enlarge portion of the curve for v_{z0} = 100 is shown in the inset of Figure (a). In Figure (c) the points are for the slopes of fitting lines in Figure (a) for the first linear growth stage, and the line are linear fitting result for the points. (Adopted with permission from ref. [89].)

The situation becomes much more complex when cavities exist. The configurations with temperature field are shown in Figures 61(a) and 61(b). The times are the same as in Figure 60. Besides the cavity morphology, one can understand better the energy transformation from kinetic to thermal. A high temperature layer, surrounding the deformed cavity, exists. Because the plastic work by the stresses is pronounced in that region. The configurations with v_z field at the same two times are shown in Figures 61(c) and (d), respectively. With the reflecting back of compression wave from the upper free surface, the range with high particle velocity decreases.

Figure 62 shows both the dependence of maximum upward particle velocity, $v_{z\max}$, above the cavity on the initial tensile velocity v_{z0} and the dependence of maximum downward par-

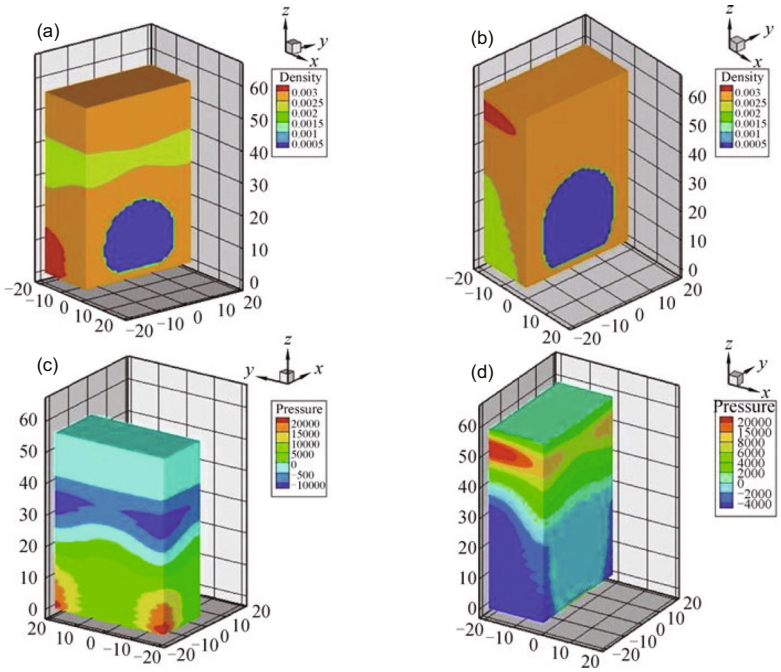

Figure 60 (Color online) Configurations with density field ((a) and (b)) and configurations with pressure field ((c) and (d)) at two times, 7.2 and 12 ns. Only the portion with $-20 \leqslant x \leqslant 0$ is shown in each plot. (Adopted with permission from ref. [89].)

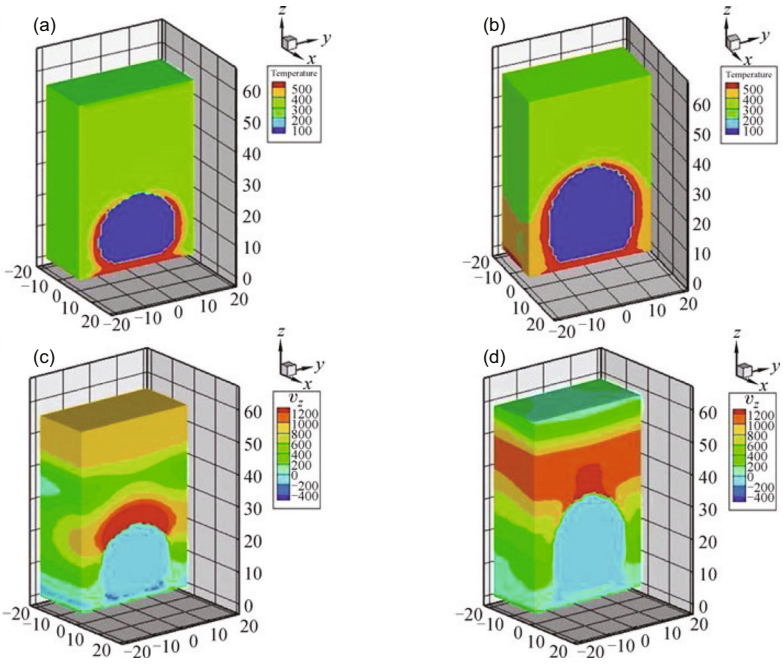

Figure 61 (Color online) Configurations with temperature field ((a) and (b)) and configurations with v_z field ((c) and (d)) at two times, 7.2 and 12 ns. Only the portion with $-20 \leqslant x \leqslant 0$ is shown in each plot. (Adopted with permission from ref. [89].)

ticle velocity, $v_{z\min}$, below the cavity versus v_{z0}. The points show simulation results and the lines show fitting results. Both $v_{z\max}$ and $|v_{z\min}|$ increase logarithmically with v_{z0}.

4.3 DBM investigations

As mentioned above, many behaviors in heterogenous materials under strong shock can be described and investigated by fluid models. At the same time, the non-equilibrium phase transition kinetics studied by the liquid-vapor model can help to understand the solid-solid phase transition in the metal under shock from two sides, the morphological and non-equilibrium behaviors. When such a flow system is in a unstable state, the free energy of the system is too high compared with that in its ground or metastable state. The inter-particle

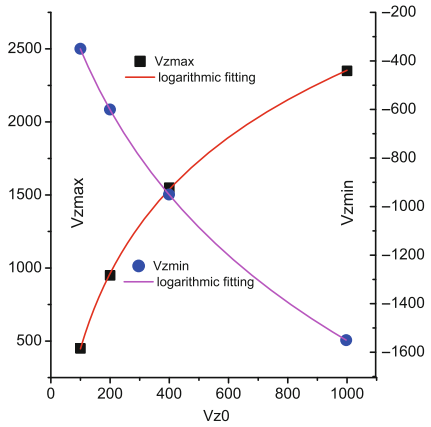

Figure 62 (Color online) Maximum upward particle velocity and maximum downward particle velocity versus initial tensile velocity v_{z0}. The points are simulation results and the lines are logarithmic fitting results. (Adopted with permission from ref. [89].)

force will drive changes, and the gradient force induced by gradients of macroscopic quantities will opposes them. From the view of phase transition kinetics, for a system instantaneously quenched from a disordered state into a two-phase coexistence one, the flows are generally known to undergo two TNE stages, the early spinodal decomposition stage and the later domain growth stage, before approaching the finial totally separated equilibrium state. Previous studies were focused mainly on the domain growth law in the second stage, which is partly due to the uncertainty in quantitative determining of transition time from the former to the latter stages. This uncertainty is due to the existence of large variety of complex spatial patterns, especially during the spinodal decomposition stage. In a recent work [90], with the help of morphological analysis, our group presented a geometrical criterion for separating the two stages and some new insights into the first stage have been obtained. But roughly speaking, the spinodal decomposition stage has, far from, being well-understood. At the same time, as a typical case of non-equilibrium phase transition, the TNE behaviors during the whole process are barely investigated.

The DBM is a kinetic method making it possible to investigate effectively the complex interplay between various non-equilibrium behaviors. Based on the measured TNE quantities, one can further define new quantities, like the TNE strength, to roughly estimate the deviation from the corresponding thermodynamic equilibrium. In a recent study [8], it is found that the TNE strength attains its maximum at the end of the spinodal decomposition stage. Consequently, the TNE intensity presents a convenient physical criterion to separate the two stages of phase separation. The effects of latent heat and surface tension on phase separation were also studied via the DBM simulation. Some specific results are as below.

Figure 63 shows three sets of snapshots for the density field in the phase separation process. The difference for the three columns is the value of K. K is a coefficient describing the strength of interfacial energy. The interfacial tension strongly influences the pattern morphology, the evolution speed and the depth of phase separation. At the time $t = 0.045$, numerous mini domains with large density ratio occur for the case with small $K = 10^{-5}$, which indicates that the evolution has already entered the spinodal decomposition stage. While for cases of larger K, at the time, the density variance is small, and it decreases with the increasing of coefficient K. Nevertheless at the time $t = 0.153$, the mean domain size and the phase separation depth are nearly the same for the three cases; all of them proceed to the domain growth stage. In the later times, it is observed that the larger the coefficient K, the faster the phase separation, the bigger the mean size, the fewer the domain number and the wider the interface.

These observations can be quantitatively studied via the time evolution of the characteristic domain size $R(t)$. See Figure 64(a). As a rough estimation of the phase separation process, the $R(t)$ curves behave similarly and distinguish approximately the phase separation process into two stages. During the first stage, the characteristic domain size $R(t)$ increases and arrives at a platform which is marked by the green arrow. It should be pointed out that, the marked point corresponds to the end of the spinodal decomposition stage. The plateau is dependent on the initial state described by the intensity of random noise, the depth of temperature quench, and also the interfacial tension. The larger the interfacial tension, the longer the duration t_{SD} of the spinodal decomposition stage, and the larger the domain size R_{SD} for the spinodal decomposition stage.

During the phase separation process, the potential energy transforms into the thermal energy and the interfacial energy. The physical scenario is as below. Under the action of interparticle force, a liquid (vapor) embryo continuously gains (loses) molecules due to the condensation (evaporation), then the interface emerges and part of the potential energy transforms into the interfacial energy. Since the interfacial energy is proportional to K, an increasing K means an increasing interfacial energy. Since the interfacial tension always resists the appearance of new interface to minimize the interfacial energy, an increasing K means an increasing t_{SD} required for completing such an energy conversion process. The larger the interfacial tension, the longer it takes for sharp interfaces to form.

In the second stage, under the action of interfacial tension, small domains merge to minimize the interfacial energy. The domain size $R(t)$ continuously grows with time. The slope of the $R(t)$ curve presents a phase separation speed u_{DG} for the domain growth stage. It can be found that u_{DG} increases with increasing K. Thus, during the second stage, the phase separation process is significantly accelerated by the interfacial tension. Specifically here, the curve of $R(t)$ for $K = 6 \times 10^{-5}$ crosses with the other two at the time $t = 0.153$, then rises quickly and exceeds the former two. When the coefficient K varies from 10^{-5} to 3×10^{-4}, the dependence of separation

speed u_{SD} on K can be fitted by

$$u_{DG} = e + fK - (gK)^2 + (hK)^3, \tag{34}$$

with $e = 0.00764$, $f = 1.51 \times 10^2$, $g = 8.06 \times 10^2$, $h = 1.02 \times 10^3$, as shown in the legend of Figure 64(a).

To numerically determine the duration t_{SD}, we check the evolution of the second Minkowski measure: boundary length $L(t)$ for the density field. The density threshold is cho-

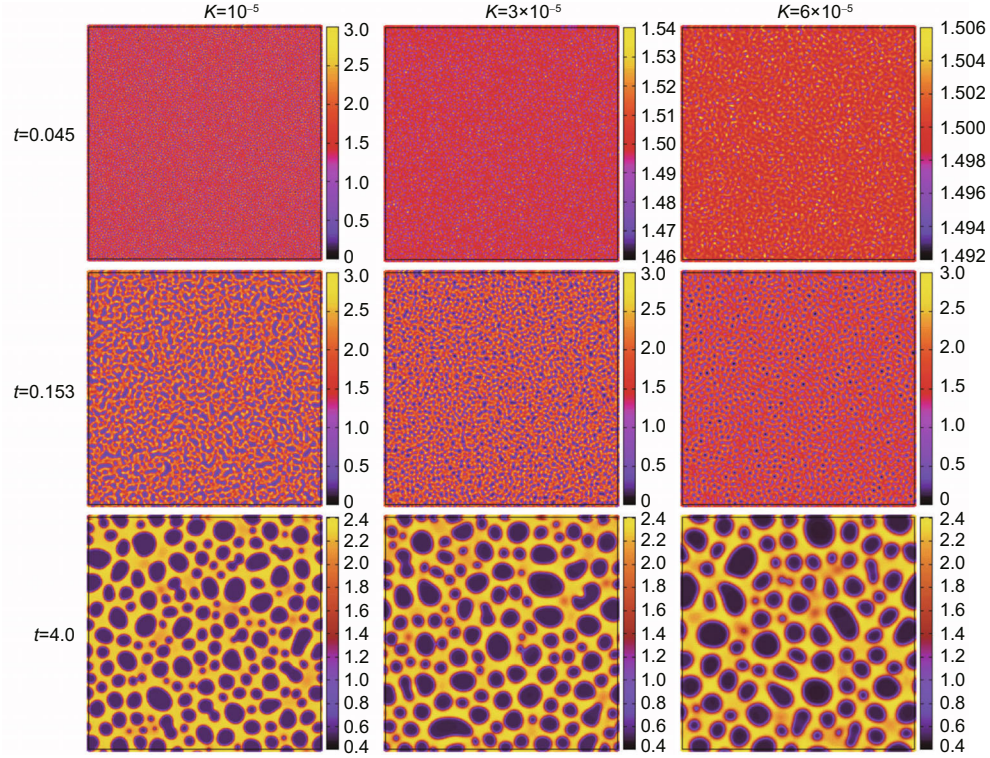

Figure 63 (Color online) Density patterns at three representative times during thermal phase separation processes, $t = 0.045$ (the first row), $t = 0.153$ (the second row) and $t = 4.0$ (the third row). From left to right, the three columns correspond to cases with $K = 10^{-5}$, 3×10^{-5} and 6×10^{-5}, respectively. (Adopted with permission from ref. [8].)

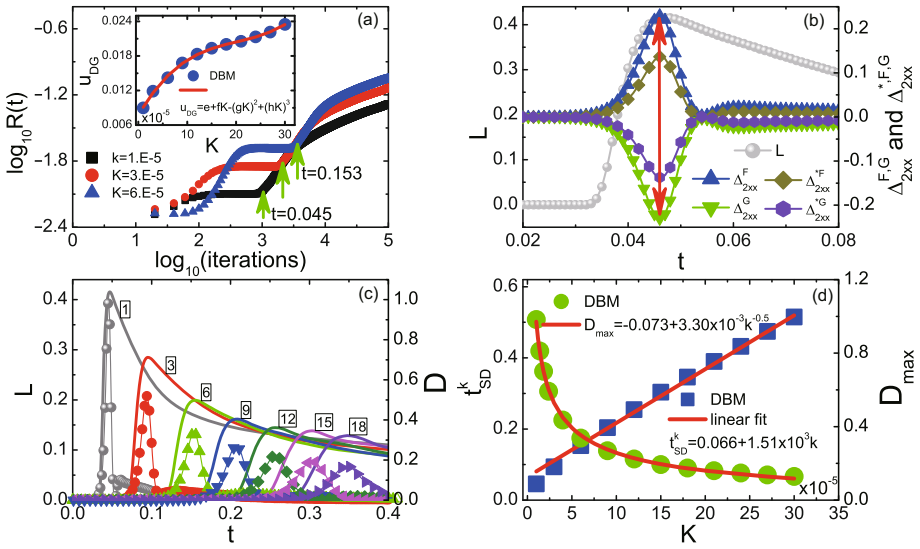

Figure 64 (Color online) (a) Evolutions of the characteristic domain sizes R for the procedures shown in Figure 63. (b) Evolutions of the boundary length L and the xx component of some TNE manifestations for the phase separation process with $K = 10^{-5}$. (c) Evolutions of the boundary lengths L (solid curves) and the corresponding TNE intensities D (curves with solid symbols) for phase separation processes with various K. Here 1, 3, 6, ..., 18 labeled on the L-curves indicate cases with $K = 10^{-5}$, 3×10^{-5}, 6×10^{-5}, ..., 1.8×10^{-4}, respectively. (d) Duration of the spinodal decomposition stage t_{SD} and the maximum TNE intensity $D_{\max}$ as functions of K. (Adopted with permission from ref. [8].)

sen as $\rho_{\rm th} = 1.70$ in Figure 64(b). Because the density pattern has the largest boundary length for this case. Some TNE manifestations are exhibited in the same panel. One can find that the peak of the $L(t)$ curve exactly coincides with the peaks or troughs of the TNE curves.

Since each component of $\mathbf{\Delta}$ or $\mathbf{\Delta}^*$ describes the TNE from its own aspect, a "TNE strength" can be defined as:

$$D = \sqrt{\mathbf{\Delta}_2^{*2} + \mathbf{\Delta}_3^{*2} + \mathbf{\Delta}_{3,1}^{*2} + \mathbf{\Delta}_{4,2}^{*2}} \tag{35}$$

to roughly and averagely estimate the deviation amplitude from the thermodynamic equilibrium. One can also use $\sqrt{\mathbf{\Delta}_2^2 + \mathbf{\Delta}_3^2 + \mathbf{\Delta}_{3,1}^2 + \mathbf{\Delta}_{4,2}^2}$ (or its F, or G component). Before using the concept, one needs first nondimensionalize the discrete Boltzmann equation. Here, the discrete Boltzmann equation is dimensionless, so do $\mathbf{\Delta}$ and D. Thus, $D = 0$ indicates that the system is in thermodynamic equilibrium, and $D > 0$ indicates that the system is out of the thermodynamic equilibrium. Figure 64(c) shows the evolutions of $L(t)$ (solid curves) and $D(t)$ (curves with solid symbols), where $D(t)$ is calculated from $\mathbf{\Delta}^{*F}$) for various K. The numbers, 1, 3, 6, ..., 18, labeled on the $L(t)$-curves indicate cases with $K = 10^{-5}$, 3×10^{-5}, 6×10^{-5},...,1.8×10^{-4}, respectively. One can find a perfect coincidence between the peaks of $L(t)$ and $D(t)$ in pairs. Thus, the behavior of $D(t)$ curve provides a convenient and efficient physical means to discriminate the stages of spinodal decomposition and domain growth. The left side of the peak corresponds to the spinodal decomposition stage, and the right side corresponds to the domain growth stage. Compared to the morphological method, the extension of the current approach to three dimensions is straightforward. Because the calculation of the interface area in three dimensional case is much more complex in coding.

From Figure 64(c) one can observe that, when K varies in the range $[10^{-5},\ 3 \times 10^{-4}]$, the dependence of t_{SD} on K can be fitted by the following equation,

$$t_{SD} = a + bK, \tag{36}$$

with $a = 0.066$ and $b = 1.51 \times 10^3$. The specific result is shown in Figure 64(d). Go to a further step, because of the length of interface, the depth of phase separation, as well as the gradient force and inter-particle force obtain their peak values at the end of the stage of spinodal decomposition, the TNE effect is the strongest at this moment. The interfacial tension effects are found to decrease the maximum of the TNE strength $D_{\rm max}$. The relation follows roughly

$$D_{\rm max} = c + dK^{-0.5}, \tag{37}$$

with $c = -0.073$ and $d = 3.30 \times 10^{-3}$. See Figure 64(d). From the physical side, the Knudsen number is usually used to measure the TNE level. It is defined as the ratio between the molecular mean-free-path λ and a macroscopic character length L. For a phase separation process, L can be roughly taken the domain size R_{SD} at the end of the spinodal decomposition stage. Thus, the mean Knudsen number ${\rm Kn} = \lambda/2R_{SD}$. Since R_{SD} increases with K, Kn and the TNE strength decrease with K. This can also be understood as follows. A larger coefficient K broadens the interfacial width, reduce the gradient force and refrain the TNE intensity. The details of the DBM and more results are referred to ref. [8].

As for system under detonation by DBM, we just briefly mention a few results. As an initial application, various non-equilibrium behaviors around the detonation wave in one-dimensional detonation process were preliminarily probed. It is found that, at the von Neumann pressure peak, the system is in a state being close the its local thermodynamic equilibrium; in front of and behind the von Neumann pressure peak, the system deviates from the thermodynamic equilibrium state in opposite directions. The following TNE behaviors, exchanges of internal kinetic energy between different displacement degrees of freedom and between displacement and internal degrees of freedom of molecules, have been observed. It was found that the system viscosity (or heat conductivity) decreases the local TNE, but increases the global TNE around the detonation wave. Even locally, the system viscosity (or heat conductivity) results in two competing trends, i.e. to increase and to decrease the TNE effects. The physical reason is that the viscosity (or heat conductivity) takes part in both the thermodynamic and hydrodynamic responses to the corresponding driving forces. The ideas to formulate DBM with the smallest number of discrete velocities and DBM with flexible discrete velocity model are presented [5,6,30]. A double-distribution-function DBM for combustion is referred to ref. [41].

4.4 MD investigations

MPM simulation is based on continuum assumption. The material properties are described by constitutive equation. Consequently, the minimum element of the material used in the simulation should be larger than 1 μm. When some critical phenomena, such as initiating of phase transition, localization of plasticity, creation of damage and fracture, have to be considered, the original continuum modeling and constitutive equation do not work any more and need to be improved based on more fundamental mechanisms in smaller scales. The MD simulation can study the dynamic behaviors of microscopic structures in the scales of nanometer and sub-nanoseconds. The bridge connecting the microscopic MD simulation and the mesoscopic MPM simulation is still a grand challenge in nowadays. We hope to incorporate the microscopic evolution mechanisms of these critical phenomena into the larger-scale model via some coarse-grainning techniques.

Our MD simulations can be classified into two groups. The first group aims to study the creation mechanisms of micro-structures like dislocation, void, cavity, and new phase grain in metal materials [42, 91-93]. The second group aims to study the evolution behaviors of these micro-structures [43, 44, 94, 95].

4.4.1 Creation mechanisms of micro-structures

Due to the fundamental importance for plastic deformation, phase transition and dynamic fracture modelings, the dislocation and void nucleation processes have attracted extensive theoretical and experimental studies. But due to the complexities, the physical picture on the self-organized atomic collective motions during dislocation creation, and the mechanisms for the void nucleation, obscured by the extreme diversity, in structural configurations surrounding the void nucleation core, are still open problems and far from being well clarified. Via MD simulations we investigated the origin of dislocation creation and void nucleation in face-centered-cubic (FCC) ductile metals under uniaxial high strain rate tensile loading. The dislocation creation process can be described by three distinguished stages (See Figure 65): In the first stage, thermal fluctuations randomly activate Flattened octahedral structures (FOSs) in the material. In the second stage, double-layer defect clusters occur via self-organized stacking of FOSs on the close-packed plane. In the third stage, stacking faults appear and the Shockley partial dislocations are created from the double-layer defect clusters by slip between the layers. The dislocation nucleation and slip dot not release bulk stress (negative pressure), even though they can release part of the shear stress. Plenty of energies accumulate in the system with the increase of the tensile strain. At the weak points in material, some voids or cracks occur to release the accumulated energy.

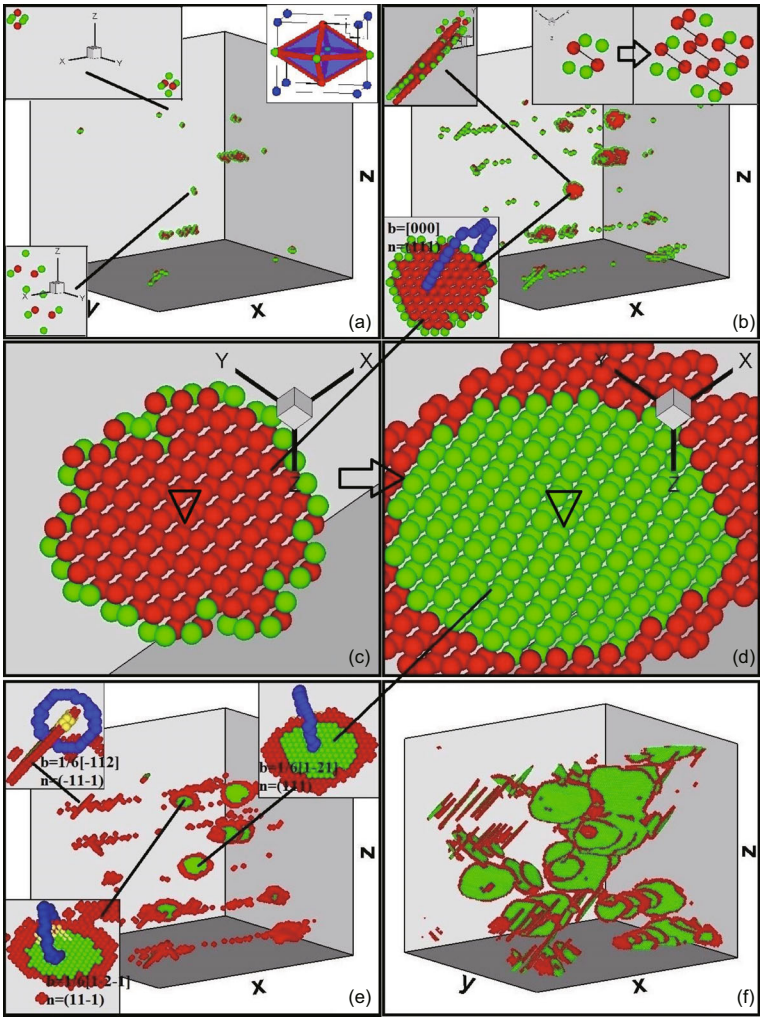

Figure 65 (Color online) Molecular-dynamics simulation snapshots that provide a general three-stage physical picture for the generation of dislocations and the corresponding non-zero Burgers vectors in FCC ductile metals under high-strain-rate uniaxial stretch. Panel (a) shows that FOSs (for a detailed view, see the top right inset) are firstly activated in the metals by thermal fluctuations. Panel (b) shows that FOSs begin to stack on the close-packed plane to form double-layer defect clusters (see the top left inset for closer view). This stacking process is shown in the top right inset. The Burgers vector for the double-layer defect cluster structure is calculated to be zero, as shown in the bottom left inset. Panel (c) and panel (d) shows the transformation of the double-layer defect clusters into stacking faults. Panel (e) gives a few non-zero Burgers vectors of the nucleated dislocations that surround the stacking faults. Panel (f) shows the growth of stacking faults and dislocations. In panels (a)-(c)the coordination numbers of red and green atoms are 13 and 12, respectively, while in panels (d)-(f) the CNA values of red and green atoms are 5 (dislocation atoms) and 2 (HCP atoms), respectively. (Adopted with permission from ref. [42].)

The cavity creation process can be described by the following two stages. In the first stage, stacking faults, with different normal directions, evolve to intersect with each other. They generate pillar-like vacancy strings located at the intercrossing lines (See Figure 66 and the inset inside). In the second stage, these vacancy strings grow into voids via emitting dislocations. The growth of the nucleated voids releases stress, which suppresses the growth of neighboring vacancy strings.

The above process of vacancy string creation could be regarded as two successive plastic deformations. The first deformation brings a stacking fault into the system (see the inset in Figure 66(c)), and the atoms have a displacement of the corresponding Burgers vector along the plane. During the second deformation process, the atoms further have a corresponding displacement along the other plane, which results in a volume variation (see the inset in Figure 66(d)). The plastic deformation resulting from stacking faults can be described by a distortion tensor $\boldsymbol{\beta} = \boldsymbol{\delta}(\Sigma)\boldsymbol{b} = \int \int_{\sum} \mathrm{d}s' \delta(\boldsymbol{r}' - \boldsymbol{r})\boldsymbol{b}$, where $\boldsymbol{\delta}(\Sigma)$ is the surface Dirac function, Σ is stacking fault plane, and $\boldsymbol{b}$ is the Burgers vector. The relative volume variation is $\delta V/V = \mathrm{Tr}\,(\boldsymbol{\beta})$. For the case of single stacking fault, $\mathrm{Tr}\,(\boldsymbol{\beta}) = \boldsymbol{\delta}(\Sigma) \cdot \boldsymbol{b} = 0$, herefore, there is no density variation in the system. For the case of two stacking faults intersecting with each other, the distortion tensor is $\boldsymbol{\beta} = \boldsymbol{\beta}_1 + \boldsymbol{\beta}_2 \cdot (\boldsymbol{I} + \boldsymbol{\beta}_1)$, where $\boldsymbol{\beta}_1$ and $\boldsymbol{\beta}_2$ are the distortion tensors of the two stacking faults, respectively. Therefore, the volume variation is $\delta V = \int \mathrm{d}V \mathrm{Tr}\,(\boldsymbol{\beta}_1 \cdot \boldsymbol{\beta}_2) = (\boldsymbol{b}_2 \cdot \boldsymbol{n}_1)(\boldsymbol{b}_1 \cdot \boldsymbol{n}_2)L/|\boldsymbol{n}_1 \times \boldsymbol{n}_2|$, where $\boldsymbol{n}_1$ and $\boldsymbol{n}_2$ are normal directions of the stacking faults and L is the length of the vacancy string. Here, we arrive at that the cross-section area of vacancy string resulting from the intersection of two different stacking faults is $(\boldsymbol{b}_2 \cdot \boldsymbol{n}_1)(\boldsymbol{b}_1 \cdot \boldsymbol{n}_2)/|\boldsymbol{n}_1 \times \boldsymbol{n}_2|$, and the direction of vacancy string is $\boldsymbol{n}_1 \times \boldsymbol{n}_2$.

The dislocations generated from the double-layer defect

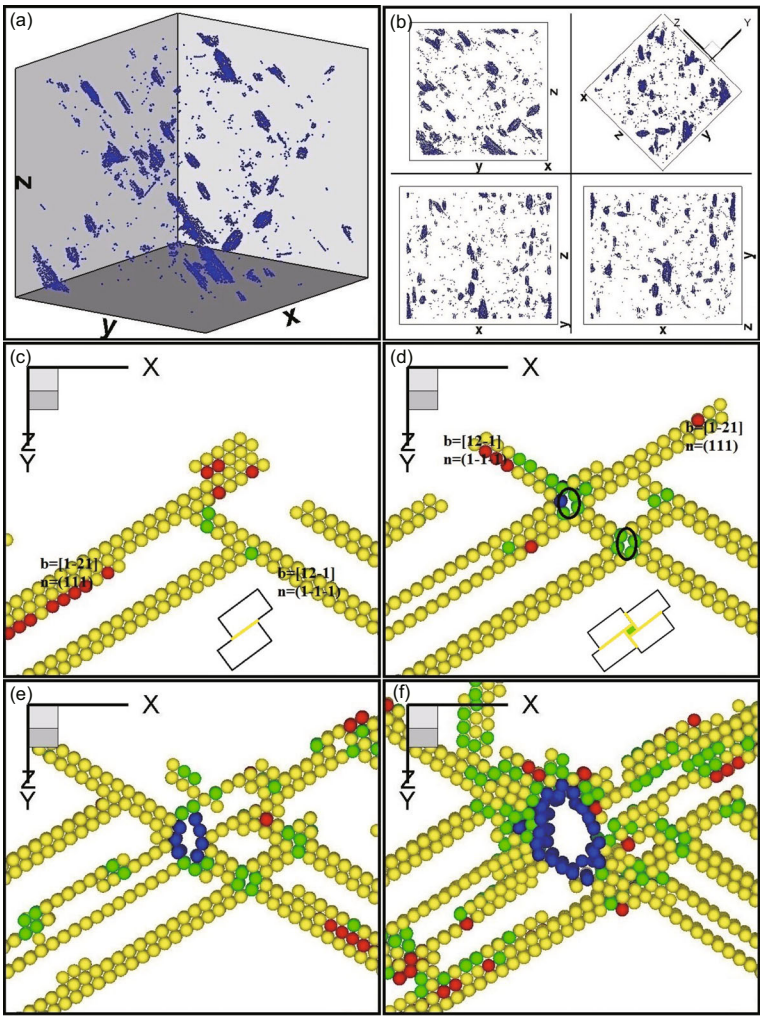

Figure 66 (Color online) Incipient void nucleation phenomenon and its two-stage mechanism. Panels (a) and (b) shows the void nucleation phenomenon. Panels (c)-(f) show the evolutionary process of these atoms in a picked slice, and therein the insets are the schematic diagrams of stacking faults creation and vacancy string formation. Panel (c) shows that four stacking faults appearing as lines nucleate from double-layer defect clusters. Panel (d) shows that two pillar-like vacancy strings are generated from the the intersections of stacking faults, see the upper and lower black circles. Panel (e) shows that the upper vacancy string transforms into a void via emitting dislocations, while the lower one retains its size. Panel (f) shows that nucleated voids grow gradually and neighboring vacancy strings disappear. (Adopted with permission from ref. [42].))

clusters are all Shockley partial dislocations. Since the corresponding Burgers vectors have been obtained, the initial vacancy strings have a typical cross-section area, $\sqrt{2}a^2/36$, according to the above expression, where a is the lattice constant. They have six possible types of distribution directions. But only two types of voids are observed in Figure 66(a). The corresponding directions are [011] and [01$\bar{1}$] which are perpendicular to the loading direction. The physical reasons are as follows: The energy released via growth of a vacancy string is $\int\int \mathrm{d}\boldsymbol{s}\cdot\boldsymbol{\sigma}\cdot\delta\boldsymbol{r}$, where $\delta\boldsymbol{r}$ is the growth displacement, $\boldsymbol{s}$ the surface area of the vacancy string, and $\boldsymbol{\sigma}$ the applied stress. In the numerical simulation, the applied stress is σ_{xx}. Only when the vacancy string is perpendicular to [100], does its growth release more energy and evolve into voids. The numerical results shown in Figure 66(a) confirm this analysis.

With the development of the high-pressure technology, structure phase transition in metal has attracted wide notice and been one of the focuses in material physics. As for the structure transition from bcc to hcp occurred in iron under a pressure higher than 13 GPa, before our works, even though the transition process has been roughly understood, how the phase transition initiate and how the new phase grain nucleate are still far from clear. The MD simulation shows that, similarly to case of dislocation nucleation, the nucleation process of new phase grain can also be described by three stages. In the first stage, as shown in Figure 67, with the aid of thermal fluctuations, some atoms deviate from their equilibrium positions to form FOSs with two different deformation directions in the local region. In the second stage, as shown in Figures 68(a) and (b), the FOSs with different deformation directions aggregate to form a thin stratified structure like twin-crystal configuration. In the third stage, as shown in Figures 68(b) and (c), the thin stratified structure undergoes a relative slip to form the new hcp phase.

4.4.2 *Evolution mechanisms of micro-structures*

When model the damage and micro-fracture, the growth and coalescence of voids have to be considered. We investigated the dynamics of a pair of voids located along loading direction in crystal copper under uniaxial tension. Voids with different sizes grow and coalesce through dislocation nucleating on void surfaces. In early elastic stage, voids grow along the loading direction, then the vertical direction and finally form octahedral-like structures in plastic stage. Critical yield stress increases with decreasing of void size (See Figure 69). If radius is large, dislocations nucleate and migrate symmetrically. Voids elongate in loading direction, and evolution process is similar. If radius is small,dislocations nucleate asymmetrically and voids elongate along vertical direction. The process of void growth may be characterized by elastic deformation, independent growth, coalescence and steady growth (See Figure 70).

The growth mechanism of new phase domain has not obtain quantitative characterization. The main reason is due to lacking technology to precisely determine the new phase domain. To calculate and analyze the morphology and growth speed of the hcp phase domains, a central-moment method and a rolling-ball algorithm were designed. To clarify our derived growth law of the phase domains, a phase transition model was proposed. Studies show that the new-phase evolution process undergoes three distinguished stages with different time scales of the hcp phase fraction in the system.

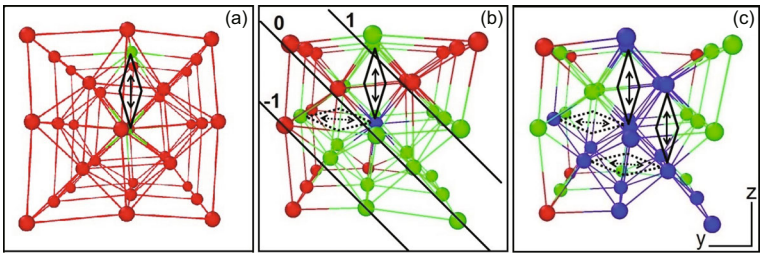

Figure 67 (Color online) The nucleation and growth mechanisms of hcp domain by means of the formation of FOSs. Panel (a) shows the structure of formed FOS. Panel (b) shows the nucleation of hcp domain. Panel (c) shows the growth of hcp domain. (Adopted with permission from ref. [43].)

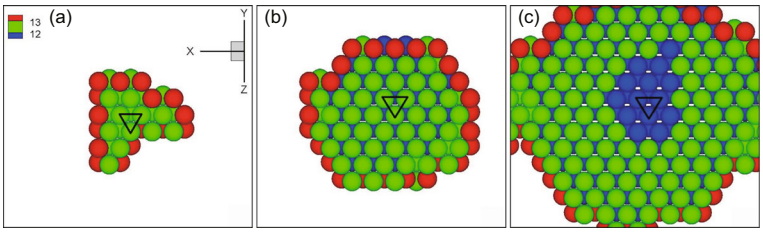

Figure 68 (Color online) The relatively slip process between the atomic layers observed from the normal direction of phase plane. Panel (a) shows that some FOSs simply aggregate into a thin stratified structure. Panel (b) shows that the atoms in the central region of the middle layer are transformed into hcp structure. Panel (c) shows that the atoms in the central region of three layers are transformed into hcp structure. (Adopted with permission from ref. [43].)

In the initial independent growth stage, the morphology of domain is ellipsoid-like where the three principal axes are approximately along [100], [011], and [011] directions. The growth in the three directions shows different velocities. See Figures 71(a) and (b). The growth velocity depends also on the morphology of phase domain. The growth speed of a single phase domain is supersonic. It is in a range 4×10^4 to 5×10^3 m/s. See Figures 71(c) and (d). The time evolutions of the size, surface area, and volume of the single hcp domain follow roughly $L \sim t^{0.5}$, $A \sim t^{1.0}$, $V \sim t^{1.5}$, respectively. See Figure 72. The FOS is the primary structural unit of the embryo nucleus and phase interface of hcp domains. The interfacial energy is reduced via formation of FOSs. The hcp phase domain grows up via forming new FOSs along the phase boundary. The growth rate of single phase domain depends on the loading means *and its occurrence time.*

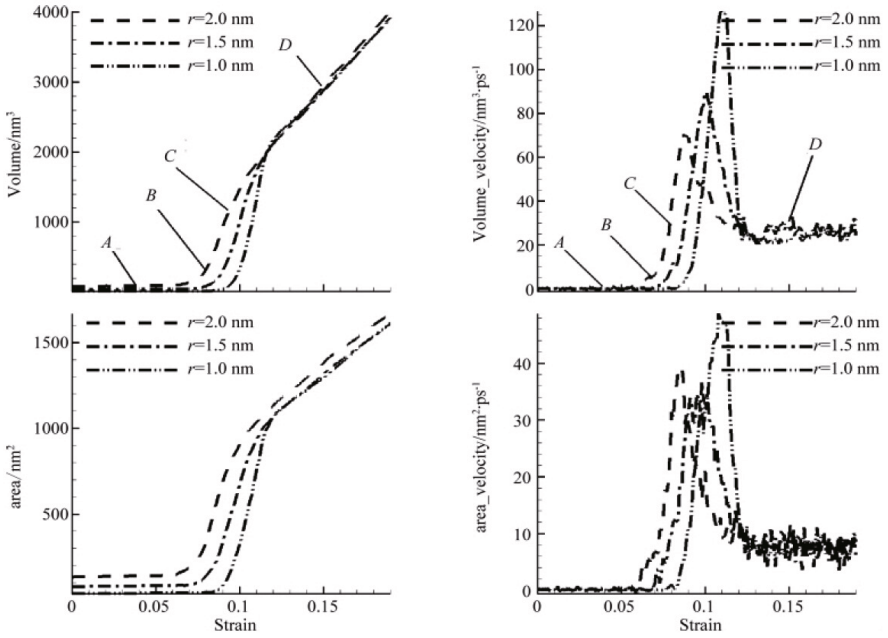

Figure 69 Volumes and areas of voids with different size. (Adopted with permission from ref. [92].)

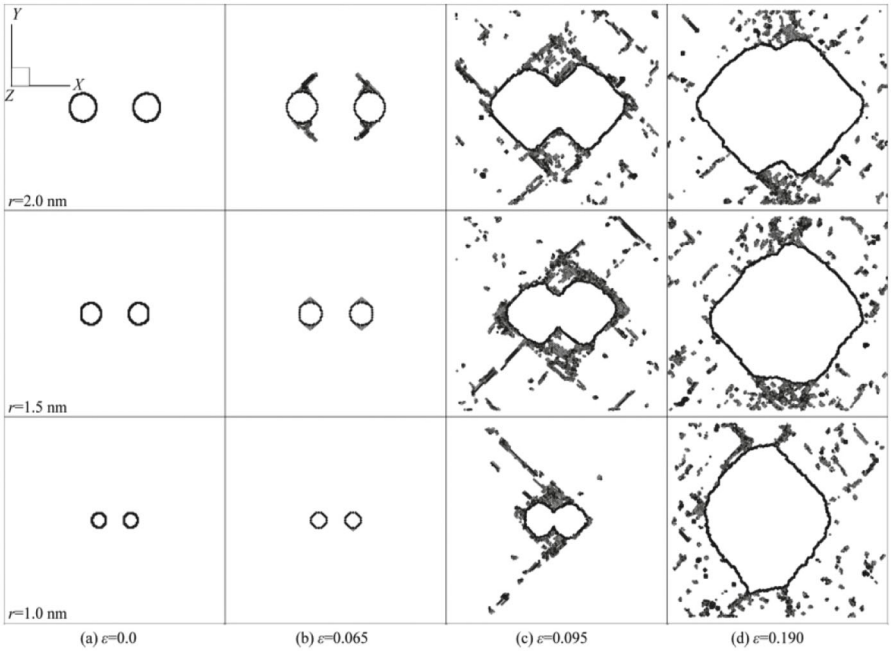

Figure 70 Growth and coalescence of voids with different size. (Adopted with permission from ref. [92].)

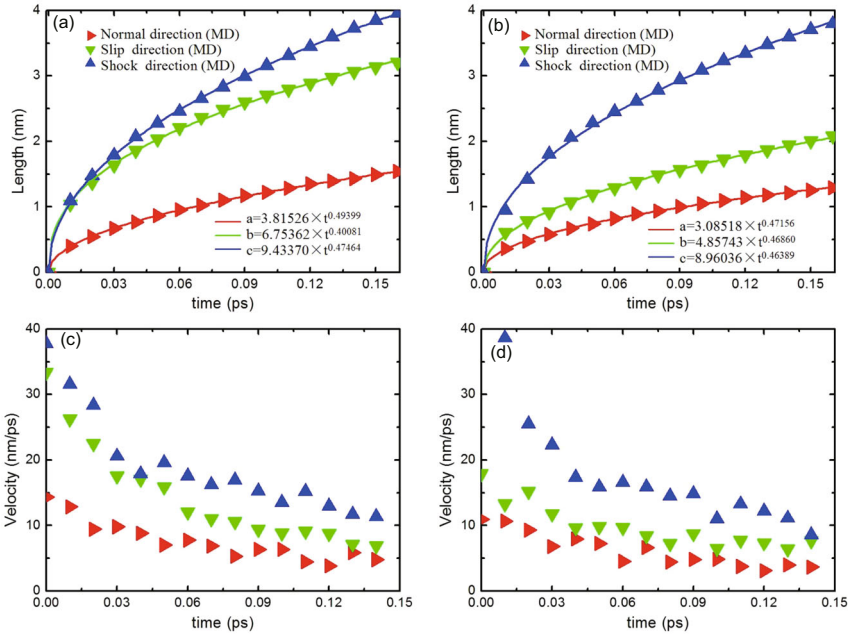

Figure 71 (Color online) Principal-axis lengths and growth speeds of two HCP phase domains which form at different times under the same shock velocity. Panels (a) and (b) are the principal-axis lengths, while panels (c) and (d) are the growth speeds. The symbols are the MD simulated results and the lines are the fitting results. (Adopted with permission from ref. [44].)

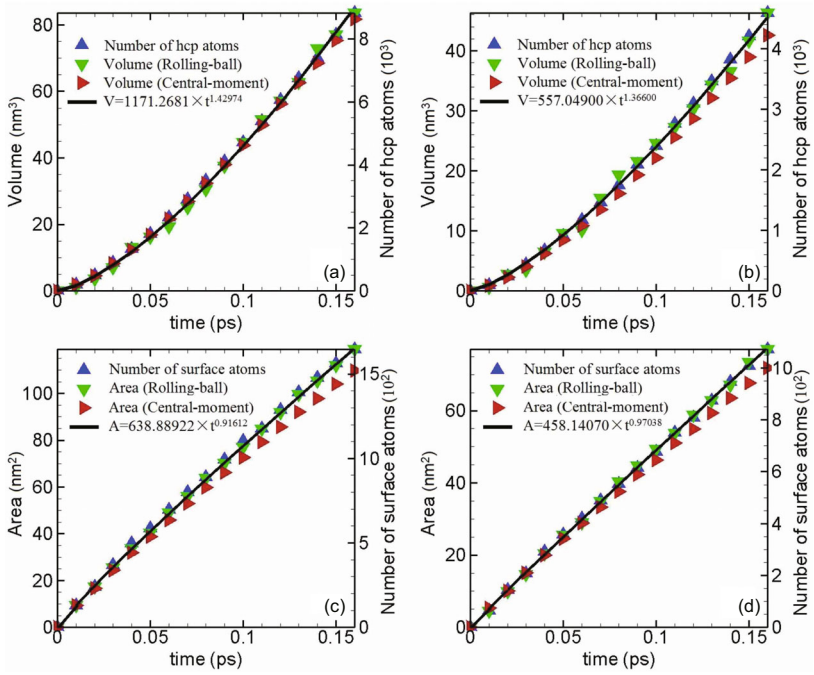

Figure 72 (Color online) Time evolutions of surface areas, volumes, and the corresponding atom numbers of the same two phase domains as those used in Figure 71. The symbols are the MD simulated results and the lines are the fitting results. (Adopted with permission from ref. [44].)

4.4.3 From micro to meso scales: coarse-grained modeling

As an specific example of coarse-grain modeling from the micro to mesoscales, based on the order parameter theory of Ginzburg-Landau, we propose a phase transition model to describe the shocking kinetic process in iron. To this aim, we choose the slippage ξ of the lattice as the order parameter. It varies from $\xi = 0$ in bcc structure to $\xi = 1$ in hcp structure, as schematically shown in Figure 73(a), where the horizontal axis represents the distance away from the phase interface. For the uniform bulk phase transition in metal iron, to undergo transformation from bcc to hcp structure via the lattice slippage, the system needs to overcome a potential barrier [96], as schematically shown in Figure 73(b). However, surely, what observed in experiments and simulations are not uniform bulk structure transition, but complex

processes with creation and growth of new phase domains. Therefore, a solely uniform description is insufficient. The phase domain effects must be reasonably included in a phase transition model. In the stage of new phase domain nucleation, within the local region with stress concentration, the atoms overcome the potential barrier with the aid of collective thermal fluctuations. Simulation results have shown that, in the growth stage of a phase domain, the growth speed is supersonic, and the stress wave has no enough time to propagate in the domain of hcp phase. It is mainly the interfacial energy that drives the growth of a new phase domain. The potential energy field of a slice in the simulated system is shown in Figure 73(e), where the regions with red, blue, and other colors represent the bcc, hcp, and interface structures, respectively. The potential energy in the interfacial region is in between those for hcp and bcc phases, from which we obtain the schematic shown in Figure 73(c). The interface energy is negative, from which we obtain the schematic shown in Figure 73(d). It is the interfacial energy that reduces prominently the potential barrier between two phases. Consequently, the transition process becomes easier.

Based on this physical scenario, the relation between system energy and order parameter can be roughly described by

$$F = \int \left[f(\xi) - \frac{D}{2}(\nabla\xi)^2 \right] \mathrm{d}^3\boldsymbol{r}, \tag{38}$$

where the first and second terms in the integrand are the bulk free energy and interface energy of the system, respectively. Specifically,

$$f(\xi) = \frac{a}{2}\xi^2 - \frac{a+1}{3}\xi^3 + \frac{1}{4}\xi^4$$

is a bi-stable function with two stable points, $\xi = 0$ and $\xi = 1$. Here, the dependence of bulk free energy on temperature and pressure is described by the parameter a. Under low pressure, $a > 1/2$, the bcc phase is stable, while under high pressure, $a < 1/2$, the hcp phase is stable. The possible anisotropy in the interface energy has been ignored for simplicity. The evolution equation of the order parameter reads

$$\partial_t \xi = \frac{\delta F}{\delta \xi} = f'(\xi) - D\nabla^2\xi. \tag{39}$$

For the steady growth of one-dimensional phase domain,

$$\xi = \xi(\eta) \equiv \xi(x - c_0 t).$$

It satisfies the following eigenvalue equation

$$\begin{cases} f'(\xi) - D\partial_\eta^2\xi + c_0\partial_\eta\xi = 0, \\ \xi\,|_{\eta\to-\infty} = 0, \\ \xi\,|_{\eta\to+\infty} = 1, \end{cases} \tag{40}$$

where c_0 is the growth speed of the hcp phase domain. For the convenience of describing the growth of a three-dimensional phase domain, we adopt the local coordinate system, instead of the Cartesian coordinates,

$$\boldsymbol{r} = \boldsymbol{r}_0 + \lambda\boldsymbol{n} + \mu\boldsymbol{t}_1 + \nu\boldsymbol{t}_2,$$

where $\boldsymbol{r}_0$ represents a point at the interface, and $\boldsymbol{n}, \boldsymbol{t}_1, \boldsymbol{t}_2$ represent the normal and two principal tangential unit vectors of the interface at position $\boldsymbol{r}_0$, respectively. The evolution equation of order parameter reads

$$\partial_t\xi = f'(\xi) - D(\partial_\lambda^2 + \partial_\mu^2 + \partial_\nu^2 + (k_1+k_2)\partial_\lambda - k_1\partial_\mu - k_2\partial_\nu)\xi, \tag{41}$$

where k_1 and k_2 are the curvatures along the two principal tangential directions, respectively. According to the relation

$$\xi = \xi(\eta) \equiv \xi(\lambda - vt),$$

the above expression can be reduced to

$$f'(\xi) - D\partial_\eta^2\xi + (-Dk + v)\partial_\eta\xi = 0 \tag{42}$$

with the boundary conditions

$$\xi\,|_{\eta\to-\infty} = 0,\ \xi\,|_{\eta\to+\infty} = 1,$$

and $k = k_1 + k_2$. Comparing eqs. (40) and (42) giving the growth speed of new phase domain evaluated by

$$v = c_0 + Dk. \tag{43}$$

For structure phase transition induced by shock wave, the interface energy is related to the pressure surrounding the phase domain. So, the parameter D is a function of pressure. Simulated results and theoretical analysis show that the growth speed is supersonic and the value of D is almost a constant in the phase domain growth process. Therefore, eq. (43) indicates that the growth speed of the phase domain is a function of the local curvature. In the initial stage, the volume of phase domain is small, the local curvature is large, and consequently the energy triggering phase transition is relatively more concentrated, which is responsible for the relatively quick growth. With the growth of the phase domain, the interfacial area becomes larger, and the local curvature decreases, which is responsible for the relatively slow growth.

For an ellipsoidal phase domain, the local curvature is nonuniform on the surface of the phase domain. The portion with a larger curvature grow more quickly. As a result, the phase domain becomes more and more flat with time. Actually, simulation results in Figure 74 confirm that various phase domains evolve to be disc-like, spherical, columnar, elongated, etc., in the later stage. Now, we can go a further step to give a very simple but illustrative estimation on the dynamics of domain growth. For this purpose, we assume the phase domain is spherical with radius R, the growth speed in eq. (43) gives

$$\dot{R} = c_0 + 2D/R.$$

Further assuming $c_0 \to 0$ gives

$$R(t) = \sqrt{4Dt}.$$

Our MD simulation results show that the linear length of an ellipsoidal phase domain roughly follows $L \sim t^{0.465}$, which is close to what this analytical expression indicates. The difference bettwen the curvatures of the sphere and the ellipsoid is responsible for deviation of exponent 0.465 from 0.5.

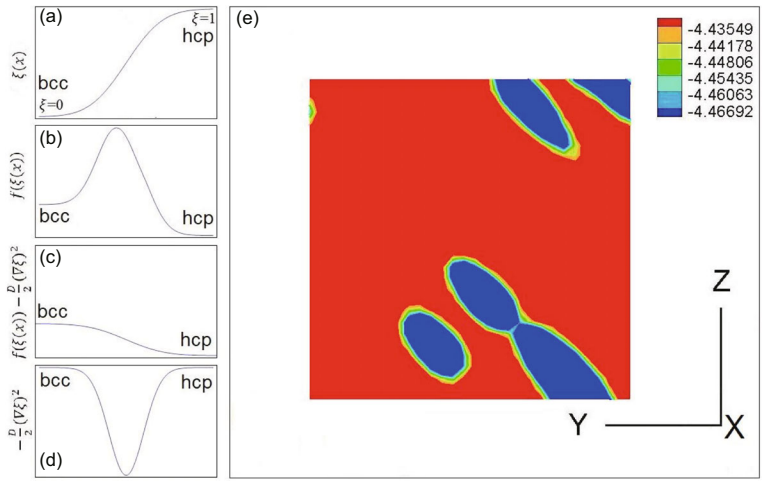

Figure 73 (Color online) The potential energy distribution and schematic diagram of phase transition. Panels (a)-(d) are the schematic diagram of phase transition, where the horizontal axis represents the distance away from the phase interface. Panel (e) shows the potential energy distribution of a slice in shocked iron. (Adopted with permission from ref. [44].)

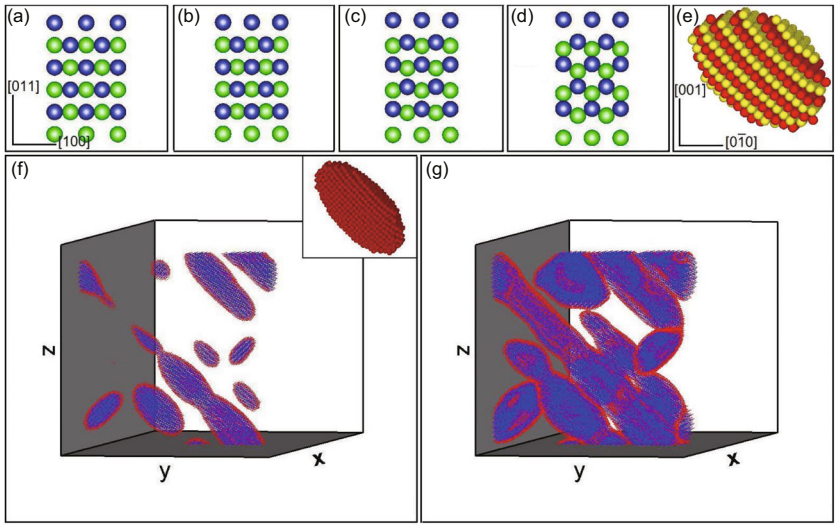

Figure 74 (Color online) Microstructure evolution in iron from BCC to HCP structure during the shock process. Panels (a)-(e) show the phase transition mechanism, while panels (f) and (g) show the formed new phase domains in the shocked region. (Adopted with permission from ref. [44].)

A second example of mesoscopic modeling is used to study the impulse propagation in granular chain. Solitary signal has been observed and well understood in a horizontal granular chain without considering dissipation. But in vertical chain under gravity, more complex and interesting phenomena occur. Via MD-like simulations, signal is found to change its speed and form with propagating depth. The grain velocity and the propagation speed, amplitude and width of the signal follow power laws in depth. Physically, this is due to the power-law type changing of elastic properties in a medium under gravity. The impulse propagation can be classified into two types in terms of the behavior of the power-law exponents. The latter are further dependent on the strength of the nonlinearity. The power-law exponents are invariant with the strength of the impulse in the weakly nonlinear regime, while they vary with the strength of the impulse in the strongly nonlinear regime [97, 98]. For the case with impurities inside the vertical granular chain under gravity, different characteristics in the backscattered signal are found. These characteristics are dependent on the presence of light and heavy impurities inside the chain. Physically, that the soliton can be confined in the region with light impurity but can not in the region with heavy impurity is responsible for this difference. This difference can be used, in nondestructive inspection of impurities in granular medium, to discriminate between light and heavy impurities. It may also be used in design of grain layer protector from shocks [99, 100].

5 Conclusion and discussions

The macroscopic mechanical properties of a heterogeneous material under shock rely not only on the loading/unloading

process, but also on the stable or slowly-varying structures within the material, such as dislocations in plastic deformation, new phase domains in phase transition, cavities and shearing bands in the damaging or fracture process, non-equilibrium vortices and jets behind the shock front, etc. Those structures generally cover a wide range of spatiotemporal scales. To understand and model the macroscopic behaviors of a heterogeneous material, those mesoscopic structures and their evolution mechanisms, their energies and means of dissipation, must be taken into account.

To access the complex structures and physical fields, various models and simulation schemes are needed. For such typical multi-scale problems, there are mainly two complementary categories of studies. In the first category, the bridging of schemes in neighboring scales, for example, the connection of molecular dynamics and finite element methods, is the main concern. In the second category, the complicated problem is first decomposed into different scales. One constructs/chooses a model according to the scale and main mechanisms working at that scale. Perform numerical simulations using the relatively mature schemes. The physical information is transferred between neighboring scales in such a way: The statistical information of results in smaller scale contributes to establish the constitutive equation in larger one. Except for the microscopic molecular dynamics model, both the mesoscopic and macroscopic models can be further classified into two categories, solidic and fluidic models, respectively. A cellular automata model for elastic solid material was attempted in 2013 [101]. No matter which model and simulation tool are used, what obtained are large quantity of data. How to analyze the data and pick out reliable structural information is the first issue to resolve. The solution to this issue is the footstone of further studies.

The dynamical responses of heterogeneous materials are studied from the sides of strength, inertia and dissipation. To access the strength behaviors, the molecular dynamics is used to simulate the evolutions of microscopic structures, such as dislocations, phase domains, microscopic voids under uniform deformation and shock loading; the material point method is used to simulate the mesoscopic behaviors of cavities under shock loading and unloading. To access the inertia and dissipation behaviors, the discrete Boltzmann method is used to simulate the non-equilibrium phase transition kinetic processes, and the material point method is used to simulate porous media under shock.

It is found that, the creation and evolution of microscopic structures in crystal are mainly determined by the properties of local active regimes. For example, dislocations tend to occur in regimes with dense FOS structures; Microscopic voids tend to occur in regimes where fault stacks cross; The FOS structures near a phase domain make easier the phase transition. The morphology of mesoscopic cavities in the collapsing process is determined by the complex interactions between various wave series. For example, when the compression is weak, the cavity may keep its spherical structure; when the compression is strong, the regime around the cavity, where the waves focus, may show a tip even jet. During the phase transition process, the growth of the new phase domain is determined by the competition of transition energy, surface energy, and thermal energy. For example, during the spinnodal decomposition, more surfaces occur and consequently the non-equilibrium effects resulted from the mass flux and energy flux become more pronounced with time. This observation can be used as a new physical criterion to discriminate the two stages, spinnodal decomposition and domain growth, in the phase transition process. In porous materials under shock, the vortices and jets resulted from all cavities behind the shock front show some kinds of similarities for various cavity sizes, shock strengths, etc. Therefore, the global scenarios of porous materials under shock show some structural and dynamical similarities. For example, the temperature fields occurred in two separate shocking processes with two sets of shocking strengths and porosities may show similarities. The DBM results for phase separation are helpful for understanding the structural phase transition occurred in metal under shock.

After all, physics is an experimental science. The simulation results are to be checked, directly or indirectly, with experiments, and are used to anticipate possible new results. Due to the complexity of the problem, some phenomenological or semi-phenomenological models have to be taken into account when necessary.

Up to now, all the above observations are based on intuitive understanding on relevant structures. How to quantitatively bridge the structures and macroscopic dynamical properties of the material is still a challenging and open problem. This involves two important and complimentary issues, coarse-grained modeling of mesoscopic structures and homogenization of complex heterogeneous systems. The former is relevant to parametrization of mesoscopic structures, energy relations and dissipation mechanisms. The latter is relevant to the averaging and transition between neighboring scales. The two issues are currently demanding much more corporations and efforts of scientists in related fields. The field of heterogeneous materials under shock will see significant development in the following years.

The authors thank Prof. Hua Li for fruitful discussions. This work was supported by the Science Foundation of LCP, National Natural Science Foundation of China (Grant Nos. 11475028 and 11325209), the Opening Project of State Key Laboratory of Explosion Science and Technology (Beijing Institute of Technology, Grant No. KFJJ14-1M) and the Open Project Program of State Key Laboratory of Theoretical Physics, Institute of Theoretical Physics, Chinese Academy of Sciences, China (Grant No. Y4KF151CJ1).

1 S. Nemat-Nasser, and M. Hori, *Micromechanics: Overall Properties of Heterogeneous Materials* (Elsevier, Oxford, 1999).
2 V. F. Nesterenko, *Dynamics of Heterogeneous Materials* (Springer-Verlag, New York, 2001).

3 J. S. Zhu, X. M. Hu, P. Wang, J. Chen, and A. G. Xu, Adv. Mech. **40**, 400 (2010).
4 A. G. Xu, G. C. Zhang, Y. B. Gan, F. Chen, and Y. J. Li, Front. Phys. **7**, 582 (2012).
5 A. G. Xu, G. C. Zhang, Y. J. Li, and H. Li, Prog. Phys. **34**, 136 (2014).
6 A. G. Xu, G. C. Zhang, and Y. J. Ying, Acta Phys. Sin. **64**, 184701 (2015).
7 M. L. Rocca, A. Montessori, P. Prestininzi, and S. Succi, J. Comput. Phys. **284**, 117 (2015).
8 Y. B. Gan, A. G. Xu, G. C. Zhang, and S. Succi, Soft Matter **11**, 5336 (2015).
9 B. J. Alder, and T. E. Wainwright, J. Chem. Phys. **31**, 459 (1959).
10 A. Rahman, Phys. Rev. **136**, A405 (1964).
11 M. S. Daw, and M. T. Baskes, Phys. Rev. B **29**, 6443 (1984).
12 R. Harrison, A. F. Voter, and S. P. Chen, in *Atomistic Simulation of Materials*, edited by V. Vitek, and D. J. Srolovitz (Plenum Press, New York, 1989).
13 F. Auricchio, and L. B. da Veiga, Int. J. Numer. Meth. Eng. **56**, 1375 (2003).
14 X. Zhang, K. Y. Sze, and S. Ma, Int. J. Numer. Meth. Eng. **56**, 689 (2006).
15 S. Ma, X. Zhang, Y. Lian, and X. Zhou, Comput. Model. Eng. Sci. **39**, 101 (2009).
16 S. Ma, X. Zhang, and X. M. Qiu, Int. J. Impact. Eng. **36**, 272 (2009).
17 S. Ma, *Material Point Meshfree Methods for Impact and Explosion Problems (in Chinese)*, Dissertation for the Doctorial Degree (Tsinghua University, Beijing, 2006).
18 F. H. Harlow, in *Methods for Computational Physics*, edited by B. Adler, S. Fernbach, and M. Rotenberg (Academic Press, New York, 1964), **3**, 319-343
19 D. Burgess, D. Sulsky, and J. U. Brackbill, J. Comput. Phys. **103**, 1 (1992).
20 S. Bardenhagen, J. Brackbill, and D. Sulsky, Comput. Methods Appl. Mech. Eng. **87**, 529 (2000).
21 Y. J. Guo, and J. A. Nairn, Comput. Model Eng. Sci. **1**, 11 (2006).
22 N. P. Daphalapurkar, H. Lu, D. Coker, and R. Komanduri, Int. J. Fract. **143**, 79 (2007).
23 S. Ma, X. Zhang, X. M. Qiu, Int. J. Impact. Eng. **36**, 272 (2009).
24 A. G. Xu, X. F. Pan, G. C. Zhang, and J. S. Zhu, J. Phys.-Condens. Matter **19**, 326212 (2007).
25 X. F. Pan, A. G. Xu, G. C. Zhang, P. Zhang, J. S. Zhu, S. Ma, and X. Zhang, Commun. Theor. Phys. **49**, 1129 (2008).
26 X. F. Pan, A. G. Xu, G. C. Zhang, and J. S. Zhu, J. Phys. D-Appl. Phys. **41**, 015401 (2008).
27 B. P. Zhang, Q. M. Zhang, and F. L. Huang, *Explosion Physics* (Ordance Industry Press of China, Beijing, 1997).
28 S. Succi, *The Lattice Boltzmann Equation for Fluid Dynamics and Beyond* (Oxford University Press, New York, 2001).
29 C. D. Lin, A. G. Xu, G. C. Zhang, Y. J. Li, and S. Sauro, Phys. Rev. E **89**, 013307 (2014).
30 A. G. Xu, C. D. Lin, G. C. Zhang G, and Y. J. Li, Phys. Rev. E **91**, 043306 (2015).
31 H. L. Lai, A. G. Xu, G. C. Zhang, Y. B. Gan, and Y. J. Ying, [arXiv: 1507.01107].
32 Y. D. Zhang, A. G. Xu, G. C. Zhang, C. M. Zhu, and C. D. Lin, [arXiv: 1603.05442].
33 G. Gonnella, A. Lamura, and V. Sofonea, Phys. Rev. E **76**, 036703 (2007).
34 Y. B. Gan, A. G. Xu, G. C. Zhang, Y. J. Li, and H. Li, Phys. Rev. E **84**, 046715 (2011).
35 Y. Gan, A. G. Xu, G. C. Zhang, P. Zhang, and Y. J. Li, Europhys. Lett. **97**, 44002, (2012).
36 A. G. Xu, G. C. Zhang, and Y. B. Gan, [arXiv:1403.3744].
37 A. Onuki, Phys. Rev. Lett. **94**, 054501 (2005).
38 N. F. Carnahan, and K. E. Starling, J. Chem. Phys. **51**, 635 (1969).
39 B. Yan, A. G. Xu, G. C. Zhang, Y. J. Ying, and H. Li, Front. Phys. **8**, 94 (2013).
40 C. D. Lin, A. G. Xu, G. C. Zhang, and Y. J. Li, Commun. Theor. Phys. **62**, 737 (2014).
41 C. D. Lin, A. G. Xu, G. C. Zhang, and Y. J. Li, Combust. Flame **164**, 137 (2016).
42 W. W. Pang, P. Zhang, G. C. Zhang, A. G. Xu, and X. G. Zhao, Sci. Rep. **4**, 6981 (2014).
43 W. W. Pang, P. Zhang, G. C. Zhang, A. G. Xu, and X. G. Zhao, Sci. Rep. **4**, 5273, (2014).
44 W. W. Pang, P. Zhang, G. C. Zhang, A. G. Xu, and X. G. Zhao, Sci. Rep. **4**, 3628, (2014).
45 A. G. Xu, G. Gonnella, and A. Lamura, Phys. Rev. E **67**, 056105 (2003).
46 A. G. Xu, G. Gonnella, A. Lamura, G. Amati, and F. Massaioli, Europhys. Lett. **71**, 651 (2005).
47 A. G. Xu, G. Gonnella, and A. Lamura, Phys. Rev. E **74**, 011505 (2006).
48 A. G. Xu, G. C. Zhang, X. F. Pan, P. Zhang, and J. S. Zhu, J. Phys. D-Appl. Phys. **42**, 075409 (2009).
49 A. G. Xu, G. C. Zhang, P. Zhang, X. F. Pan, and J. S. Zhu, Commun. Theor. Phys. **52**, 901 (2009).
50 A. G. Xu, G. C. Zhang, X. F. Pan, and J. S. Zhu, Commun. Theor. Phys. **51**, 691 (2009).
51 G. C. Zhang, A. G. Xu, and G. Lu, General index and its application in MD simulations, in *Molecular Interactions*, edited by A. Meghea (InTech, Rijeka, 2012).
52 G. C. Zhang, A. G. Xu, G. Lu, and Z. Y. Mo, Sci. China-Phys. Mech. Astron. **53**, 1610 (2010).
53 J. Serra, *Image Analysis and Mathematical Morphology* (Academic, New York, 1982), Vols. 1 and 2.
54 K. R. Mecke, Phys. Rev. E **53**, 4794 (1996).
55 A. Aksimentiev, K. Moorthi, and R. Holyst, J. Chem. Phys. **112**, 1 (2000).
56 K. R. Mecke, and V. Sofonea, Phys. Rev. E **56**, R3761 (1997).
57 W. T. Góźdź, and R. Holyst, Phys. Rev. Lett. **76**, 2726 (1996).
58 C. L. Kelchner, S. J. Plimpton, and J. C. Hamilton, Phys. Rev. B **58**, 11085 (1998).
59 D. Faken, and H. Jonsson, Comput. Mater. Sci. **2**, 279 (1994).
60 R. Mencl, and H. Müller, Interpolation and approximation of surfaces from three-dimensional scattered data points, in *Scientific Visualization Conference*, Dagstuhl, Germany, June 1997, edited by H. Hagen, G. M. Nielson, and F. H. Post (IEEE, Dagstuhl, 1997), pp. 223-223.
61 J. D. Boissonant, ACM Trans. Graph. **3**, 266 (1984).
62 H. Hoppe, T. DeRose, T. Duchanp, J. Mcdonald, and W. Stuetzle, ACM Comput. Graph. **26**, 71 (1992).
63 H. K. Zhao, S. Osher, B. Merriman, and M. Kang, Comput. Vision Image Proc. **80**, 295 (2002).
64 F. Bernardini, J. Mittlelman, H. Rushmeir, C. Silva, and G. Taubin, IEEE Trans. Visual. Comput. Graph. **5**, 349 (1999).
65 S. Wang, G. Lu, and G. Zhang, Comput. Mater. Sci. **68**, 396 (2013).
66 A. G. Xu, G. C. Zhang, H. Li, Y. J. Ying, X. J. Yu, and J. S. Zhu, Sci. China-Phys. Mech. Astron. **53**, 1466 (2010).
67 A. G. Xu, G. C. Zhang, Li H, Y. J. Ying, and J. S. Zhu, Comput. Math. Appl. **61**, 3618 (2011).
68 A. G. Xu, G. C. Zhang, Y. J. Ying, P. Zhang, and J. S. Zhu, Phys. Scr. **81**, 055805 (2010).
69 M. M. Carroll, and A. C. Holt, J. Appl. Phys. **27**, 1626 (1972).

70 J. N. Johnson, J. Appl. Phys. **52**, 2812 (1981).
71 R. Becker, J. Mech. Phys. Solids **35**, 577 (1987).
72 M. Ortiz, and A. Molinari, J. Appl. Mech. **59**, 48 (1992).
73 D. J. Benson, The numerical simulation of the dynamic compaction of powders, in *High-Pressure Shock Compression of Solids IV*, edited by L. Davison, Y. Horie, and M. Shahinpoor (Springer, New York, 1997), pp. 233-255.
74 X. Y. Wu, K. T. Ramesh, and T. W. Wright, J. Mech. Phys. Solids **51**, 1 (2003).
75 T. Pardoen, I. Doghri, and F. Delannay, Acta Mater. **46**, 541 (1998).
76 T. Pardoen, and J. W. Hutchinson, J. Mech. Phys. Solids **48**, 2467 (2000).
77 V. C. Orsini, and M. A. Zikry, Int. J. Plast. **17**, 1393 (2001).
78 V. Tvergaard, and J. W. Hutchinson, Int. J. Solids Struct. **39**, 3581 (2002).
79 T. I. Zohdi, M. Kachanov, and I. Sevostianov, Int. J. Plast. **18**, 1649 (2002).
80 D. R. Curran, L. Seaman, and D. A. Shockey, Phys. Rep. **147**, 253 (1987).
81 E. T. Seppala, and J. Belak, Phys. Rev. Lett. **93**, 245503 (2004).
82 A. K. Zurek, W. R. Thissell, J. N. Johnson, D. L. Tonks, and R Hixson, J. Mater. Proc. Tech. **60**, 261 (1996).
83 A. K. Zurek, J. D. Embury, A. Kelly, W. R. Thissell, R. L. Gustavsen, J. E. Vorthman, and R. S. Hixson, AIP Conf. Proc. **429**, 423 (1998).
84 D. L. Tonks, A. K. Zurek, and W. R. Thissell, AIP Conf. Proc. **620**, 611 (2002).
85 J. P. Bandstra, D. M. Goto, and D. A. Koss, Mater. Sci. Eng. A **249**, 46 (1998).
86 J. P. Bandstra, and D. A. Koss, Mater. Sci. Eng. A **319**, 490 (2001).
87 D. A. Koss, A. Geltmacher, P. Matic, and R. K. Everett, Mater. Sci. Eng. A **366**, 269 (2004).
88 M. F. Horstemeyer, M. M. Matalanis, A. M. Sieber, and M. L. Botos, Int. J. Plast. **16**, 979 (2000).
89 A. G. Xu, G. C. Zhang, Y. J. Ying, and X. J. Yu, Front. Phys. **8**, 394 (2013).
90 Y. B. Gan, A. G. Xu, G. C. Zhang, and Y. J. Li, Europhys. Lett. **97**, 44002 (2012).
91 G. Lu, S. C. Wang, G. C. Zhang, and A. G. Xu, Acta Phys. Sin. **61**, 073102 (2012).
92 W. Pang, G. C. Zhang, A. G. Xu, and G. Lu, Chin. J. Comp. Phys. **28**, 540 (2011).
93 W. W. Pang, P. Zhang, G. C. Zhang, and X. G. Zhao, Sci. Sin.-Phys. Mech. Astron. **42**, 464 (2012).
94 Q. L. Yang, G. C. Zhang, A. G. Xu, Y. H. Zhao, and Y. J. Li, Acta Phys. Sin. **57**, 940 (2008).
95 W. W. Pang, G. C. Zhang, A. G. Xu, and P. Zhang, Adv. Mater. Res. **790**, 65 (2013).
96 J. B. Liu, and D. D. Johnson, Phys. Rev. B **79**, 134113 (2009).
97 J. Hong, and A. G. Xu, Phys. Rev. E **63**, 061310 (2001).
98 A. G. Xu, and J. Hong, Commun. Theor. Phys. **36**, 1990 (2001).
99 J. Hong, and A. G. Xu, Appl. Phys. Lett. **81**, 4868 (2002).
100 A. G. Xu, and J. Hong, Commun. Theor. Phys. **36**, 699 (2001).
101 Y. F. Dong, G. C. Zhang, A. G. Xu, and Y. B. Gan, Commun. Theor. Phys. **1**, 59 (2013).